UCLA
UCLA Electronic Theses and Dissertations

Title

Tuning Ion Transport by Functional Coordination Material for High-Performance Lithium-Ion Batteries

Permalink

Author

Li, Xinru

Publication Date

2020

Peer reviewed|Thesis/dissertation

UNIVERSITY OF CALIFORNIA

Los Angeles

Tuning Ion Transport by Functional Coordination Material for High-Performance

Lithium-Ion Batteries

A dissertation submitted in partial satisfaction of the

requirements for the degree Doctor of Philosophy

in Chemical Engineering

by

Xinru Li

2020

ABSTRACT OF DISSERTATION

Tuning Ion Transport by Functional Coordination Materials for High-Performance

Lithium-Ion Batteries

by

Xinru Li

Department of Chemical and Biomolecular Engineering

University of California, Los Angeles, 2020

Professor Yunfeng Lu, Chair

As electricity is the dominant form of energy we are using, electrochemical energy storage (EES), which reversibly stores and converts between chemical energy and electrical energy, holds great promises towards better human being civilization. Among the EES devices, rechargeable lithium-ion batteries hold considerable promises for numerous applications with profound societal impacts. Since the first commercial lithium-ion battery developed by a Sony and Asahi Kasei team led by Yoshio Nishi in 1991, extensive efforts have been made to develop better lithium-ion batteries for a

broad range of applications.

To date, the increasing demand for electric vehicles, particularly, calls for better lithium-ion batteries that are suitable for fast charging, dynamic acceleration, and regenerative braking. Such high-rate dynamic operations unavoidably cause severe polarization of the batteries that compromises their performance and lifespan. Mitigating the polarization is critical towards broader adoption of electric vehicles. Meanwhile, increasing energy density of the batteries is critical to extend mileage of electric vehicles. Replacing current anode material, graphite, with high-energy-density ones, such as lithium metal may lead to dramatic improvement of energy density. Adoption of lithium metal anodes, however, has been hampered by the high chemical reactivity and infinite relative volume change of metallic lithium.

In light of the abovementioned challenges, this dissertation research focuses on the development of functional coordination materials as ion transport modulators, which assists to mitigate polarization and stable electrolyte interface leading to better lithium-ion batteries for electric vehicles and other applications.

In chapter one, the mechanisms and limitations of state-of-the-art lithium-ion battery chemistries are introduced. An overview of novel battery chemistries based on metallic lithium anode is also provided.

In chapter two, the mitigation of concentration polarization in lithium-ion batteries by utilizing metal-organic frameworks (MOF) as electrolyte modulators was reported.

The use of such modulators leads to significantly improved power and energy output, energy efficiency and lifespan, which has demonstrated in commercial pouch cells. This work provides a simple yet effective strategy towards better lithium-ion batteries for electric vehicles and other applications.

In chapter three, artificial solid electrolyte interphase (ASEI) films on lithium metal were developed via *in-situ* polymerization of 2,3,7,8-tetrakis((trimethylsilyl)ethynyl)pyrazino[2,3-g]quinoxaline-5,10-dione, which assists to regulate uniform lithium-ion flux and passivate lithium-metal surface for dendrite-free lithium plating/stripping with improved Coulombic efficiency. Symmetric cells and full cells with such coatings exhibit excellent electrochemical performance with reduced voltage hysteresis and prolonged cycling life.

In chapter four, an electrolyte interphase built from two-dimensional anionic covalent organic frameworks (ACOF) coated was on Li for dendrite suppression. The ACOF with Li^+-affinity facilitates rapid and exclusive passage of lithium ions, yielding a near-unity Li^+ transference number (0.82) and ionic conductivity beyond 2.3 mS cm^{-1} at the interphase. Such high transport efficiency of lithium-ions could circumvent Li^+ deficiency that results in dendrite formation.

In the conclusion section, the abovementioned work was summarized and perspectives and outlooks for future research were also provided. Overall, this dissertation research applies low-cost coordination solids in lithium-ion batteries, which effectively tunes the ion transport leading to better batteries for various applications.

The dissertation of Xinru Li is approved.

Vasilios Manousiouthakis

Dante A. Simonetti

Lihua Jin

Yunfeng Lu, Committee Chair

University of California, Los Angeles

2020

ACKNOWLEGEMENT

My PhD journey at UCLA is among the most memorable journeys in my life. It is a proud privilege and a matter to offering my overwhelming gratitude to my advisor, Prof. Yunfeng Lu, who is an amazing boss in every aspect. I am especially thankful for his persistent demand for achieving excellence.

I thank UCLA for the opportunity to pursue research in a wonderful environment. I would also like to acknowledge helpful suggestions from my committee members: Dr. Vasilios Manousiouthakis, Dr. Dante Simonetti and Dr. Lihua Jin.

I wish to record my deep gratitude to my friends as well as my former colleagues. Thank you, Dr. Xiaoyan Liu, for being my best sister through my whole PhD life. Thank you, Dr. Xianyang Li and Dr. Zhuang Liu, for being my best brothers here. Thank you, Dr. Li Shen, for always being the hero showing up in someone's darkest moment. Thank you, Dr. Haobin Wu, for letting me know Queen Holly. Thank you, Dr. Gurong Shen, for being my awesome roommate. Thank you, Pengcheng Xu, for helping me get through so many obstacles. Thank you, Tianren Fu, for being my best friend in New York. Thank you, Dr. Huihui Zhou, for always being the warmest and kindest elder sister in the lab. Thank you, Dr. Seung Ho Choi, for all the bad food and wonderful trips we had. Thank you Yue Tian, for always being so supportive for my tough experiments. Thank you Dr. Zhen Han, for always being my Doraemon and sponsor for my experiments. Thank you, Jinhui Xu, for being my last Subway lunch partner. I would also like to thank the following people who have helped me undertake this journey: Dr. Zaiyuan Le, Dr. Qiangfeng Xiao, Dr. Shengxiong Xiao, Dr. Wenyue Shi,

Table of Contents

LIST OF FIGURES

LIST OF TABLES

VITA

Education:

09/16-06/17   MA.   Chemistry   Columbia University, New York

09/14-06/16   MS.   Chemical Engineering   UCLA, Los Angeles

09/10-06/14   BSc.   Applied Chemistry   East China Normal University, Shanghai

Publications:

1) **_X. Li_**, J. Wang, Y. Men, Z. Bian*."TiO2 mesocrystal with exposed (001) facets and CdS quantum dots as an active visible photocatalyst for selective oxidation reactions." _Applied Catalysis B: Environmental_ 187 (2016): 115-121.

2) **_X. Li_**, Z. Le, X. Chen, Z. Li, W. Wang, X. Liu, A. Wu, P. Xu, D, Zhang*. "Graphene oxide enhanced amine-functionalized titanium metal organic framework for visible-light-driven photocatalytic oxidation of gaseous pollutants." Applied Catalysis B: Environmental 236 (2018): 501-508.

3) **_X. Li_**, Y. Lu* _et al_. "Uniform Surface Potential Distribution Induced by in-situ Cross-linked Artificial Solid Electrolyte Interface for Stable Lithium Metal Batteries. " (ready for submission)

4) **_X. Li_**, Y. Lu* _et al_. "Electrolyte Interphase Built from Anionic Covalent Organic Frameworks for Lithium Dendrite Suppression. " (ready for submission)

5) **_X. Li_**, Y. Lu* _et al_. "Built-In Anion Complex for Mitigating Polarization in High-Rate Lithium-Ion Batteries. " (ready for submission)

6) F. Liu, F Liu, G Sun, HB Wu, G Chen, D Xu, R Mo, L. Shen, X. Li, S. Ma, R. Tao, **_X. Li_**. X.Tan, B.Xu, G.Wang, B.Dunn, P. Sautet, Y. Lu*. "Dual redox mediators accelerate the electrochemical kinetics of lithium-sulfur batteries." Nature communications 11.1 (2020): 1-10.

7) X. Lu, H. Wu, D. Kong, **_X. Li_**, L. Shen, Y. Lu*. "Facilitating Lithium-Ion Conduction in Gel Polymer Electrolyte by Metal-Organic Frameworks." ACS Materials Letters 2.11 (2020): 1435-1441.

8) SH. Choi, J. Baucom, X. Li **_X. Li_**, L Shen, YH. Seong, Y. Lu*. "Porous Carbon Microspheres with Highly Graphitized Structure for Potassium-Ion Storage." Journal of Colloid and Interface

Science (2020).

9) L. Shen, **_X. Li_**, X. Lu, D. Kong, A. Fortini, C. Zhang, Y. Lu*. "Semiliquid electrolytes with anion-adsorbing metal–organic frameworks for high-rate lithium batteries." Chemical Communications (2020).

10) Y. Tian, X. Liu, X. Cao, D. Zhang, S. Xiao, **_X. Li_**, Z. Le, X. Li, H. Li*. "Microwave-assisted synthesis of 1T MoS2/Cu nanowires with enhanced capacity and stability as anode for LIBs." Chemical Engineering Journal 374 (2019): 429-436.

11) X. Li, G. Chen, Z. Le, **_X. Li_**, P. Nie, X. Liu, P. Xu, HB. Wu, Z. Liu, Y. Lu*. "Well-dispersed phosphorus nanocrystals within carbon via high-energy mechanical milling for high performance lithium storage." Nano Energy 59 (2019): 464-471.

12) X. Liu, **_X. Li_**, H. Li, HB. Wu*. "Recent Progress of Hybrid Solid-State Electrolytes for Lithium Batteries." Chemistry–A European Journal 24.69 (2018): 18293-18306.

13) X. Liu, Y. Tian, X. Cao, **_X. Li_**, Z. Le, D. Zhang, X. Li, P. Nie, H. Li*. "Aerosol-assisted synthesis of spherical Sb/C composites as advanced anodes for lithium ion and sodium ion batteries." ACS Applied Energy Materials 1.11 (2018): 6381-6387.

14) P. Nie, Z. Le, G. Chen, D. Liu, X. Liu, HB. Wu, P. Xu, **_X. Li_**, F. Liu, Chang, X. Zhang*, Y. Lu*. "Graphene caging silicon particles for high-performance lithium-ion batteries." Small 14.25 (2018): 1800635.

15) X. Liu, P. Xu, **_X. Li_**, Y. Peng*, Z. Le*. "Assembly of mesoporous SnO2 spheres and carbon nanotubes network as a high-performance anode for lithium-ion batteries." Journal of Materials Science 53.22 (2018): 15621-15630.

16) Z. Le, F. Liu, P. Nie, **_X. Li_**, X. Liu, Z. Bian, G. Chen, HB. Wu, Y. Lu*. "Pseudocapacitive sodium storage in mesoporous single-crystal-like TiO2–graphene nanocomposite enables high-performance sodium-ion capacitors." ACS nano 11.3 (2017): 2952-2960.

17) J. Wang, X. Li, X. Li, J. Zhu, H. Li*. "Mesoporous yolk–shell SnS 2–TiO 2 visible photocatalysts with enhanced activity and durability in Cr (vi) reduction." Nanoscale 5.5 (2013): 1876-188

Chapter 1. Introduction and Background

1.1 Energy storage and battery technologies

Pioneer work with the lithium battery began in 1912 under G.N. Lewis but it was not until 1991 that Li-ion batteries by SONY company became commercially available. Over the past decades, we have witnessed tremendous implementations in various fields, including portable electronic devices, grid-scale storage and the recent emergence of electric vehicles (EVs) which revolutionize our daily transportation.[1, 2] The inherent limitations of Li-ion chemistry make it unlikely, however, that this type of battery can meet the expanding demand for energy density. It is now widely accepted both in academia and industries that battery chemistries beyond Li-ion need to be developed.[3, 4]
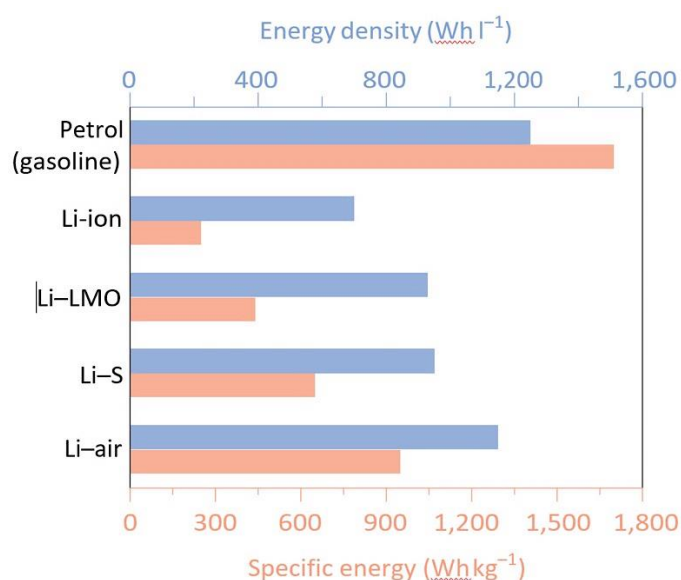
Fig. 1.1 | Bar charts showing the practical specific energy (orange) and energy densities (blue) of gasoline and typical Li batteries including the state−of−the−art Li−ion battery,

Li metal−LMO cell, Li−S and Li−air cells. Battery casings, separators and electrolytes are all taken into account, and Li metal cells are calculated based on 100 % excess Li.

Lithium metal is the ultimate choice for the anode in a Li battery, because it has the highest theoretical capacity (3,860 mAh g^{-1}, or 2,061 mAh cm^{-3}) and lowest electrochemical potential (-3.04 V versus the standard hydrogen electrode) among all possible candidates.[4, 5] Furthermore, a Li metal anode is indispensable for Li–S and Li–air systems, both of which are being intensively studied and considered for next-generation energy-storage applications.[6] The superiority of Li metal chemistry are summarized in **Fig. 1.1**. State of the art Li-ion cells can reach a specific energy of ~250 Wh kg^{-1}, which is an order of magnitude less than the practical value of petrol. With replacing the Li-ion based anode, a Li–LMO cell (where LMO is a lithium transition metal oxide) can deliver a specific energy of ~440 Wh kg^{-1}. Transition to non-intercalation cathode, such as Li-S and Li–air systems can further boost the specific energy to ~650 Wh kg^{-1} and ~950 Wh kg^{-1}, respectively. Volumetric energy density is important for space sensitive applications. Commercial Li-ion cell already possesses a relatively high value of ~700 Wh l^{-1}, but moving to a Li-air system would offer a practical value greater than 1,100 Wh l^{l}, which can be comparable to that of petrol.

Metallic Li as anode was used in the infancy of Li battery research, including in the first viable Li secondary batteries pioneered by Stanley Whittingham at Exxon in the 1970s. In the late 1980s, Moli Energy commercialized Li metal batteries using

a MoS$_2$ cathode and Li metal anode. The cycling was limited around hundreds of times, and millions of cylindrical-type cells were sold. Several accidents associated with fires brought safety concerns to public, ultimately leading to the mass recall of all the cells.[7, 8] The industry did not give up. In subsequent years, NEC and Mitsui conducted intensive reliability tests on over 500,000 Li metal cells but still failed to resolve the safety issue. At the same time, Sony developed carbonaceous anodes to replace Li metal anode and successfully built reliable Li-ion cells that we familiar with until now.[4] As a result, the commercialization of Li metal anodes was halted. However, Li-ion cells are approaching the limit of their capabilities, and attempts to revive the Li metal anode are becoming a necessity.

1.2 The state−of−the−art lithium ion battery

Among various type of batteries, the "rocking-chair" type is the most adopted in commercial batteries. Although the term "batteries" is often used, "electrochemical cell" is the more accurate term since battery may consists one or more cells in serious or in parallel. There are five major components in a cell including: the anode and the cathode for the redox reaction; the electrolyte for ion transport (no electrons allowed); the separator preventing short-circuit; and a container for the cell (**Fig. 1.2**).[9] Notices that Li-ions are travelling with the solvent shell in the electrolyte during charge and discharge, but resided as ions (Li$^+$) in the host (carbon or Li-metal oxide). Such desolvation process accompanies with redox reaction eventually stored as chemical

energy.[10]
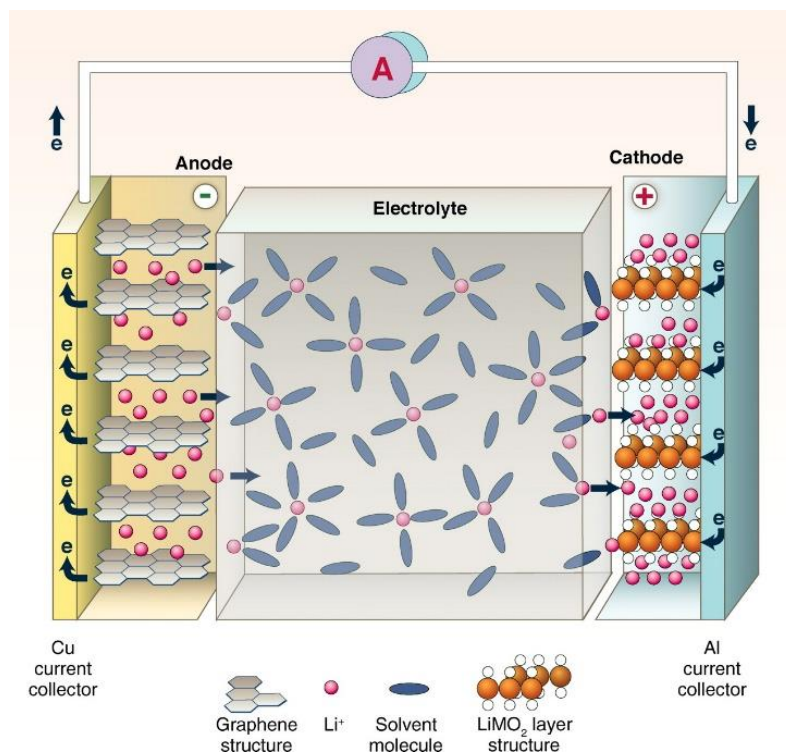
Fig. 1.2 | Schematic of typical lithium ion battery with carbon anode and lithium metal oxide cathode. Such "rock chair" type require lithium-ion shuttle between the electrodes.[9]

In a typical LIB that employs LiCoO2 and graphite as the electrodes, it follows the half and full chemical reactions shown in eq. 1 during cycling. The Li−ion can travel back and forth between the two electrodes, intercalating into cathode/anode during discharging/charging processes, respectively. Due to the shuttling of the Li−ion during the cycling, the Li−ion system is also known as "rocking−chair" battery.[11]

$$\text{Cathode:} \qquad \text{LiCoO}_2 \underset{\text{Discharge}}{\overset{\text{Charge}}{\rightleftharpoons}} \text{Li}_{0.5}\text{CoO}_2 + 0.5\text{Li}^+ + 0.5\text{e}^-$$

$$\text{Anode:} \qquad 6\text{C} + \text{Li}^+ + \text{e}^- \underset{\text{Discharge}}{\overset{\text{Charge}}{\rightleftharpoons}} \text{LiC}_6 \qquad\qquad \text{[eq. 1]}$$

$$\text{Full:} \qquad 2\text{LiCoO}_2 + 6\text{C} \underset{\text{Discharge}}{\overset{\text{Charge}}{\rightleftharpoons}} 2\text{Li}_{0.5}\text{CoO}_2 + \text{LiC}_6$$
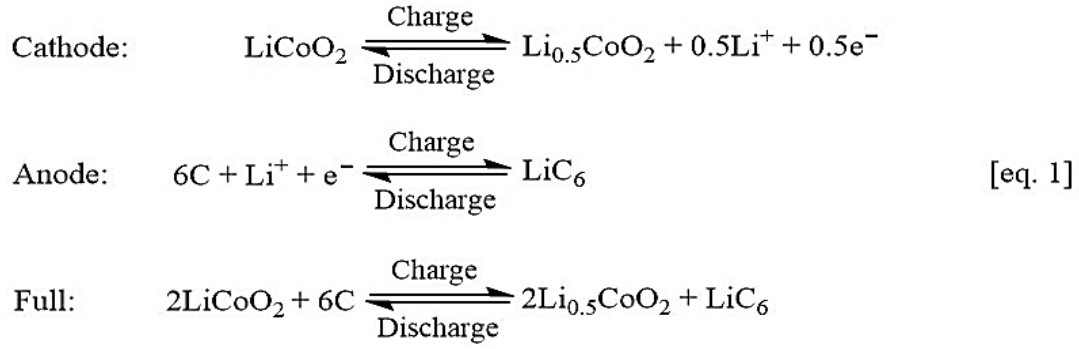
In order to have electrochemical reaction to occur for any electrochemical cell, the decrease in the Gibb's free energy is related to the electric work done by the cell, which expressed as:

$$\Delta G = -W = -n \times F \times \Delta E,$$

where F (96485 C or 26.8 Ah) is the Farady Constant, n (Coulomb or C) is the number of electrons charge involved in the stoichiometric reaction, while ΔE (V), also name the electromotive force (EMF), is the maximum voltage (potential difference) during operation.[12, 13] With such free energy consideration, the theoretical energy of a cell is:

$$Watthour(Wh) = voltage(\text{V}) \times ampare\text{-}hour(\text{Ah}),$$

and the actual energy from a battery device (when considering electrolyte and container) is about 50-70% of the above theoretical energy even at optimized charge discharge conditions.[10, 12, 13]

For performance EES device, many aspects need to be considered.[13, 14] While in a laboratory scale using EVs as an example, the following are mostly considered:

5

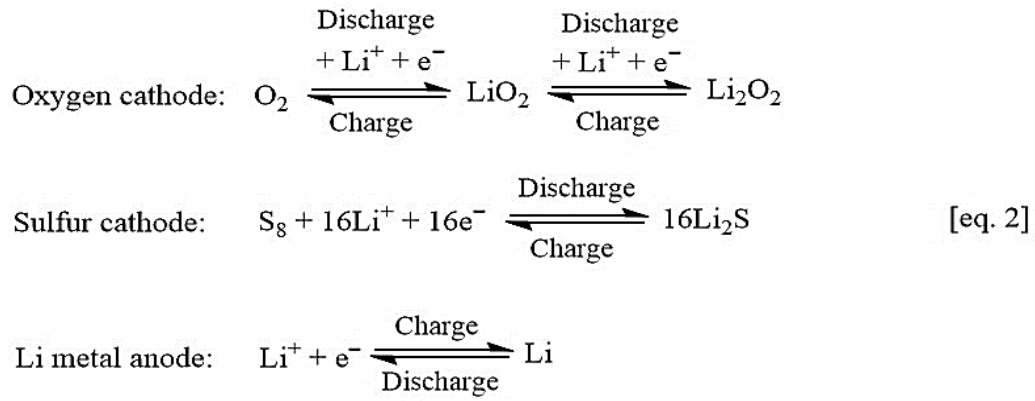1) Energy density (Wh kg^{-1}), which determines how far can the EV goes.

2) Power density (W kg^{-1}), which determines how fast we can (dis)charge.

3) Cycle life, which can lower the operation cost during lifetime of cell usage.

4) Electrochemical behavior, which fundamentally determines the qualification of a cell system. It will further affect the design strategies.

5) Charging efficiency, which determines how much the energy is wasted.

6) Other factors such as temperature window of operation, recyclability, self-discharge and etc., is out of this dissertation's scope.

1.3 Beyond lithium ion batteries: Higher energy density battery systems based on lithium metal anodes

Facing applications requiring much higher energy density such as longer range in EVs, Li-ion based cells have reached their limit. Li-metal based cells including Li-sulfur (Li-S) and Li-oxygen (Li-O$_2$) are considered as the promising candidates for the next−generation high energy batteries.[6] The total cell energy density depends on the matching between cathode and anode. Both the cathodes, S and O$_2$, as well as the anode, metallic Li, all exhibit significantly higher capacity compared to the state-of-the-art Li-ion chemistries. The electrode reactions of the two chemistries can be summarized in eq. 2. Such high capacities are originated from the usage of lighter elements as well as non-intercalation storage mechanism.

$$\text{Oxygen cathode:} \quad O_2 \underset{\text{Charge}}{\overset{\substack{\text{Discharge}\\ +Li^+ + e^-}}{\rightleftharpoons}} LiO_2 \underset{\text{Charge}}{\overset{\substack{\text{Discharge}\\ +Li^+ + e^-}}{\rightleftharpoons}} Li_2O_2$$

$$\text{Sulfur cathode:} \quad S_8 + 16Li^+ + 16e^- \underset{\text{Charge}}{\overset{\text{Discharge}}{\rightleftharpoons}} 16Li_2S \qquad \text{[eq. 2]}$$

$$\text{Li metal anode:} \quad Li^+ + e^- \underset{\text{Discharge}}{\overset{\text{Charge}}{\rightleftharpoons}} Li$$

and their higher uptake of Li^+. According to the eq.2, 2 Li^+ can be taken by each S or O_2, while in the conventional cathode such as $LiFePO_4$, each bulky $FePO_4^-$ can only store 1 Li^+.

As can be clearly seen, all these storage systems are based on a reliable Li metal anode. In the next chapter, key issues and challenges associated with Li metal anode will be further illustrated.

1.4 Key issues hindering a practical lithium-metal anode
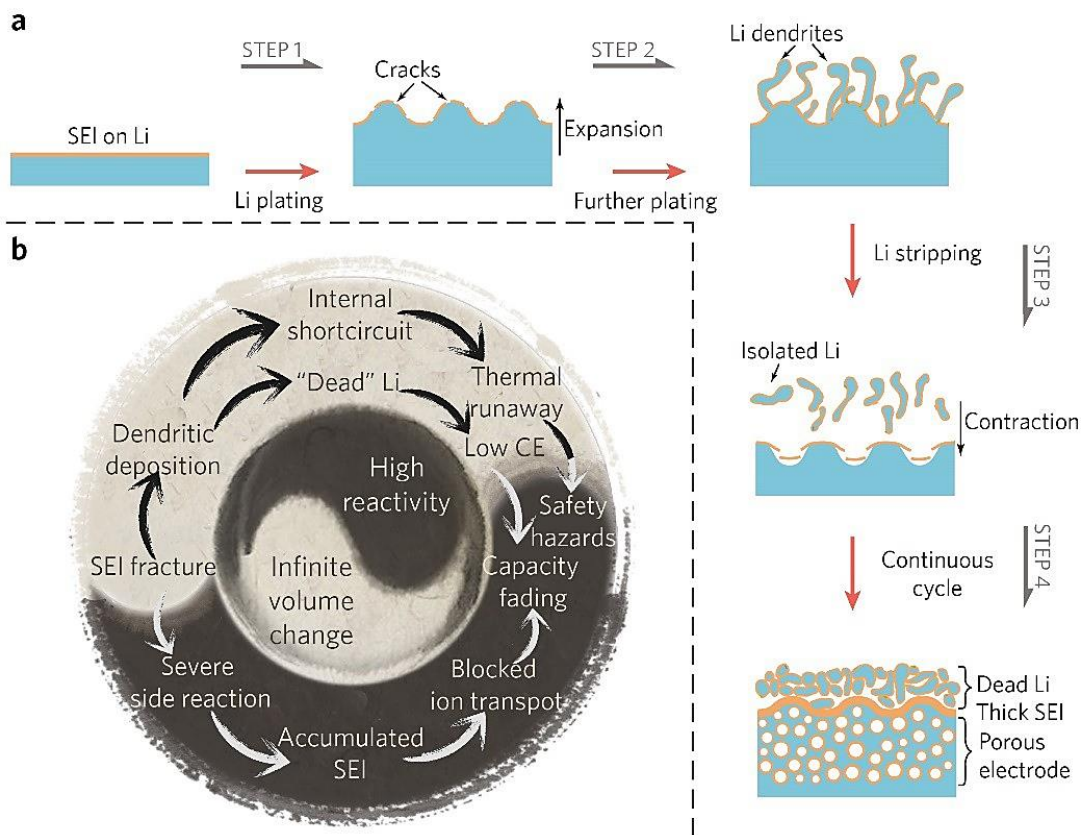
Fig. 1.3 | a, Schematic illustration of the Li stripping/plating process. [15]STEP 1: Li plating cause volume expansion which cracks the SEI film. STEP 2: further plating cause Li dendrite shoot out through the cracks. STEP 3: Li stripping produces isolated Li which later become part of the dead Li, while volume contraction further results in the SEI fracture. STEP 4: Continuous cycling causes repeated STEP 1−3 and finally form accumulated dead Li, thick SEI and porous Li electrode. **b**, Correlations of various phenomenon and problems presented in Li metal anode, where high reactivity and infinite relative volume change are two origins.

Fig. 1.3a summarizes the major problems of Li metal within plating/stripping processes. During Li plating, the huge volume expansion can rupture the SEI (STEP 1), promoting Li dendrite through the cracks (STEP 2). During stripping, volume contraction further fractures the fragile SEI, while stripping from the dendrite roots/kinks can break the electrical contact and produce "deal Li" (STEP 3). After continuous cycling (STEP 4), the repeated processes of STEP 1−3 result in porous Li electrode, accumulated thick SEI and excessive "dead Li", leading to blocked ion transport and capacity fading. More detailed correlations among the phenomena and the problems of Li metal are further summarized in **Fig. 1.3b**. We emphasize that among many challenges identified throughout the years, high chemical reactivity and infinite relative volume change should be regarded as the two root causes (center circle of **Fig. 2b**), which trigger the SEI fracture. The SEI fracture in conjunction with further side chemical reaction, dendrite formation and "dead Li" would finally bring about both safety hazards and capacity fading.
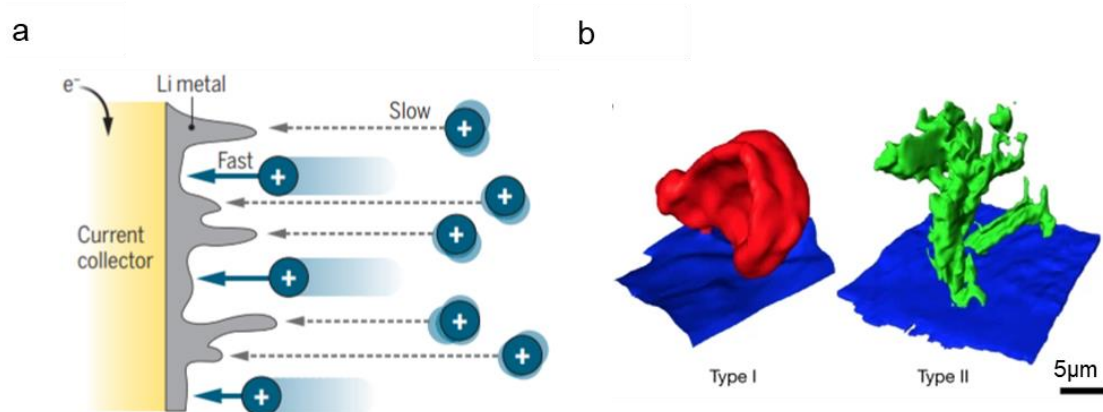

Fig. 1.4 | a, The uneven plating surface of the Li metal is due to the changeable mass transfer rate of Li ions (blue).[16] **b**, Three-dimensional reconstructions of the two types

of dendrite structures based on Cryo-STEM technology. [17]

Li dendrite formation is considered a key hurdle of the commercialization of Li metal batteries. As being mentioned previously, metallic Li was used at the infancy of Li battery research at first. The initial knowledge can be obtained from the electrodeposition field. Dendritic deposition is common for high-current electroplating of metals such as Cu, Ni and Zn, which has been comprehensively understood and successfully solved in industrial applications.[18] During electroplating, the surface of the Li metal becomes uneven due to the changeable mass transfer rate of Li ions (**Fig. 1.4a**). And cation concentration in the electrolyte maintains a gradient between the two electrodes under non-convection assumption. Once a critical current density J^* is reached, the current can only sustain for a certain period called the "Sand's time" τ, after which cations deplete and break the electrical neutrality at the plated electrode surface. This builds up a local space charge, bringing about the formation of ramified metal. This theory can well predict the electroplating of Li dendrites at current densities higher than J^*.[19, 20] However, since J^* is relatively large in commonly used electrolytes, most often, the cells will be operated far below J^*. Nevertheless, severe Li dendrites can still be observed, suggesting a different scenario from the ion-depletion theory.[21] Li dendrite growth is self-enhancing, where several theories were proposed to rationalize the phenomenon. On one hand, protrusions with high curvature yield considerably higher electric field at the tips, which tend to attract more Li-ions and result in favorable Li deposition.[22] On the other hand, the hemispherical tips enable three-dimensional (3D)

Li-ion diffusion rather than one-directional for flat surfaces, also leading to faster tip growth.[5, 23] With the support of cryo-scanning transmission electron microscopy (cryo-STEM), two main dendrite types coexisting on the lithium anode are identified (**Fig. 1.4b**).[17]

It shall be noted that volume change is a common phenomenon for all electrode materials. Intercalation based cells such as graphite, small volume change of ~10 % can still be observed.[24] Alloy−type anodes such as silicon encounter much larger volume change of near 400%, being the major challenge on their way to commercialization.[25] However, the relative volume change of Li metal anode, due to its "hostless" nature, is virtually infinite. From practical perspectives, the areal capacity of a single−sided commercial electrode needs to reach at least 3 mAh cm^{-2}, equivalent to ~14.6 μm Li. The value can be even higher for advanced batteries, which means that the movement of the Li metal interface during cycling can be as much as tens of μm. The SEI layer initially formed on Li metal surface is unlikely to accommodate this huge volume variation and thus would crack during continuous plating/stripping. The cracks locally enhance the Li−ion flux to amplify uneven Li deposition, while simultaneously exposing fresh Li to react with electrolyte.

1.5 Solid−electrolyte interphase formation on lithium metal surface

Thermodynamically, the voltage window of the cell depends on the operation voltage from both anode and cathode, and most the cases such window is larger than

the thermodynamic stability window of the liquid electrolyte. An interface, namely solid-liquid interface (SEI) is subsequently formed during operation which can kinetically stabilized the cell. As such layer is thermodynamically unstable, lots of previous studies trying to address this.

Since the pioneering studies by Peled *et al.* and Aurbach *et al.*, SEI has become a critical concept in battery research.[26-30] Due to the highly negative electrochemical potential of Li^+/Li, virtually any available electrolyte species can be reduced at the Li surface.[11] The passivation of SEI makes it possible to operate a cell under such reductive environment and extend the voltage window to 4 V and above. The early SEI explorations on Li surface and the derived theories have been extensively applied to carbonaceous anodes and demonstrated to be a great success.[31] However, compared with Li-ion chemistry, the lowest reduction potential nature makes Li anode imposes much more restrictive requirements on SEI. This lay requires high ion- conduction and electron-blocking capability, meanwhile, it needs to be homogeneous in composition and morphology. Due to huge volume change, significant interface fluctuation during cycling further requires good flexibility or even elasticity in SEI.[32, 33]
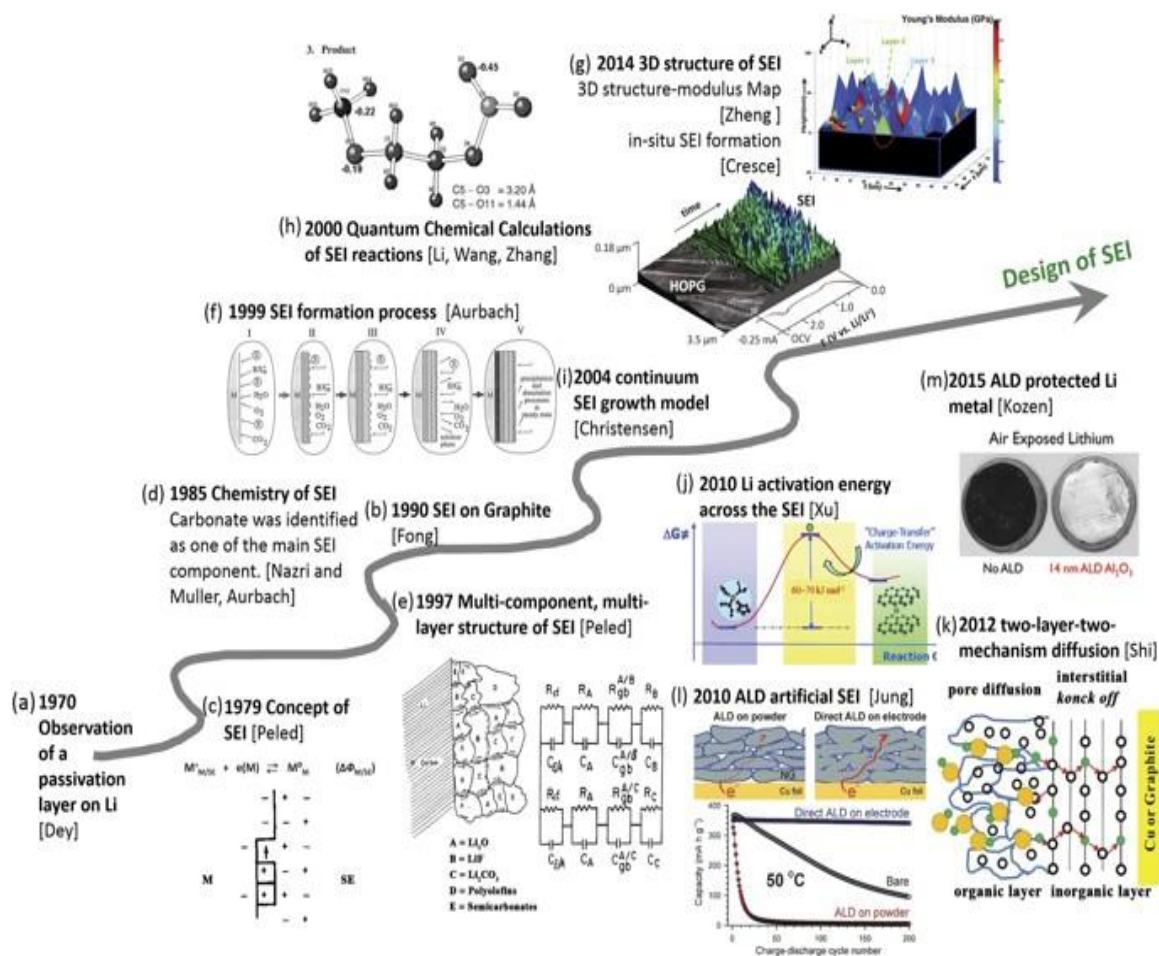
Fig. 1. 5 | A brief history of SEI on negative electrodes, from its discovery, understanding, to design, was summarized from experiments and calculations in the past four decades.[34]

According to previous studies, the SEI is basically a composite of organic and inorganic species, the composition and morphology of which are sensitive to the selection of electrolyte and electrodes systems.[28, 30] The progressive understanding of SEI over the past 50 years has been summarized in **Fig. 1.5** There are two models widely adopted, that can depict the morphological and compositional distribution within the SEI, namely, the layered and mosaic models .[27, 35] According to the layered model, the inorganic species are preferentially located in the inner layer of SEI directly

13

facing Li metal due to their lowest oxidation state, while the organic intermediates are more likely to be at the outer surface. As for the Mosaic model, it describes the SEI as a stacking of micro−domains of different species on the surface of metallic Li. In reality, it might be the combination of two cases, and the morphology might differ based on the electrolyte systems and additives employed. Recently, it was reported that the SEI can be visualized in high resolution by cryogenic transmission electron microscopy (cryo−EM), which confirms the existence of the two structures described above.[36]

Organic carbonates are the electrolyte solvents for the majority of the commercial Li-ion batteries. However, they are not ideal for Li metal batteries. It has been systematically studied that the initial SEI composition is mainly Li alkyl carbonates (ROCOOLi) via one-electron reduction of alkyl carbonates, which then can be further converted to Li_2CO_3 with trace amount of water.[29] Depending on the employed salts, Li halides can present in the SEI.[37] As reported recently by Gewirth et al., large-molecular-weight polymers can also form.[38] More stable components such as Li_2O, Li_2CO_3 and Li halides dominate in the inner layer of SEI close to Li while metastable ROCOOLi distributes at the outer layer.[30] Nevertheless, the overall SEI lacks flexibility, making them vulnerable during interfacial fluctuation. Furthermore, the possibility of forming "Mosaic" stacking imposes additional heterogeneity to the SEI.[27]

Ethers are more suitable electrolyte solvents for Li metal cells. Higher columbic efficiency (CE > 98%) with evident dendrite suppression can be achieved for several ether-based systems.[39] This was attributed to the formation of oligomers in the SEI with

good flexibility and strong binding to the Li surface.[30] However, ethers have been excluded from most of the commercial batteries mainly due to their low anodic decomposition voltage (<4 V vs Li+/Li) and high flammability.[11] Despite these shortcomings, strong motivation remains to further improve Li anode in ether electrolytes for they hold great promise in Li-S and Li-O$_2$ systems. With the development of new technologies, such as Cryogenic electron microscopy (cryo-EM),[40, 41] better upstanding of SEI formation and mechanism will be achieved.

1.6 Understanding the ion-transport properties and mechanism

Within a good electrochemical cell, the power limitation is likely coming from the low ionic conductivity. As part of the electrochemical reaction, ion transport is involved in all the above-mentioned component in the internal circuit, and most likely the case would be the rate limiting step in comparing to electronic transport at external circuit.

The ionic conductivity can be defined as follows:

$$\sigma = nZe\eta \tag{1}$$

where σ: conductivity; n: carrier concentration; Ze: charge of the conducting carrier; and Z=1 for 1 electron transfer mechanism; η: mobility.

From thermodynamic theory, the mobility and the self-diffusion coefficient can be related as follows:

$$\eta = \frac{ZeD}{kT} \qquad (2)$$

Where D: self-diffusion coefficient; k: Boltzmann constant; T: temperature.

For future high-energy density cells with require much wider voltage window, and intension for safer performance, making electrode in to "solid" could theoretically resolve all the problems that liquid based electrolyte is now facing. Unfortunately, state of art solid electrolyte still could not achieve sufficient room temperature ion conductivity (10 fold less) comparing to the liquid ones. Mechanical strength and formability are another issue before large implementation. Nevertheless, it is a promising direction for the research.

The ion-conduction mechanisms in solid-state conductors are significantly different from those in liquid electrolytes. In solution, ion salt is dissolved in the solvent. For instance, lithium ions are surround by the solvation shell form the anion of solvent. The diffusion of ions is limited by the friction of the conducting material. It is described by the Stokes-Einstein equation, with applying a friction coefficient.[11] Due to reasonably fast exchange between the solvating molecules and solvent molecules and uniform surroundings, the potential energy profile of mobile lithium ions in aprotic electrolytes can be considered almost horizontal (**Fig. 1.6**, right). In contrast, the diffusion of mobile species in a crystalline solid need to pass through periodic bottleneck points, which define an energetic barrier that separates the two local minima (typically crystallographic sites for lithium) along the minimum energy pathway (**Fig. 1.6**, left). This energy barrier is generally referred as migration or motional energy, E_m, which
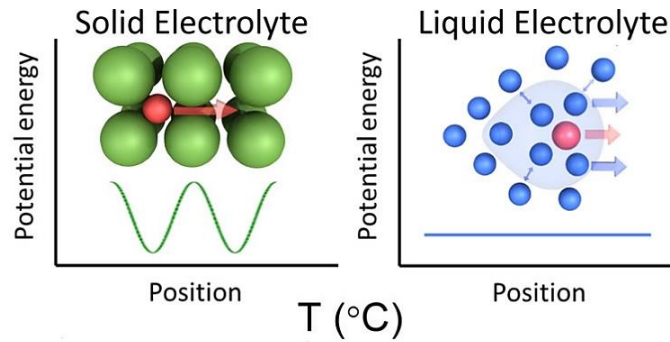
greatly influences ionic mobility and ionic conductivity.[42]

Fig. 1.6 | Potential energy of a mobile ion migration in solid electrolyte and liquid electrolyte.[42] Left and right show the potential energy of migration in a crystalline solid of an interstitial mobile ion and a charged species in red with a solvation shell of electrolyte molecules (highlighted in blue) in liquid electrolytes, respectively.

Diffusion of a conducting carrier is frozen in porous materials, and in this case, the diffusion constant is described by applying the random-walk model, with hopping frequency f and one-step distance d:

$$D = \frac{fd^2}{6}. \tag{3}$$

It should be noted that the factor 1/6 arises from three-dimensional unity and can be changed by the dimensions of the conduction mechanism. Given that the hopping frequency depends on the activation energy (E_a), the conductivity is described by the following equation:

$$\sigma = \frac{n(Ze)^2 d^2}{6kT} f_0 \exp\left(-\frac{E_a}{kT}\right)$$

$$= \frac{\sigma_0}{T} exp\left(-\frac{E_a}{kT}\right). \tag{4}$$

where E_a is the activation energy of diffusion.

The ionic conductivity of crystalline solids is also dependent on the number of interstitials, vacancies and partial occupancy on lattice sites or interstices, which is determined by the ionic energy gap or defect formation energy (E_f) in stoichiometric ion conductors (known as the intrinsic regime). In addition, interstitials and vacancies can be created by substitution of aliovalent cations, whose formation energetics is governed by the trapping energy, E_t (known as extrinsic regime). In both intrinsic and extrinsic regimes, the apparent activation energy E_a of ion conductivity contains contributions from both the defect formation energy E_f or E_t and the migration energy E_m.[43] E_a is equal to $E_m + E_f/2$ or $E_m + E_t/2$ for temperature-dependent concentrations of mobile lithium ions in intrinsic and substituted lithium-ion conductors, respectively. Plotting the logarithm of the product of conductivity and temperature as a function of the reciprocal of temperature yields apparent activation energy of lithium-ion conduction.

To quantify the ionic conductivity, it can be measured by electrochemical impedance spectroscopy (EIS). The specimen pellets or membranes can be sandwiched between two stainless steel blocking conductor and sealed in a coin-type cell. The conductivity of liquid electrolyte X-PC (X=Li, Na, Mg or Al) can be analyzed by saturating glass fiber membrane (Whatman, GF-C) in XPC. By sweeping the frequency range from 10^6 to 1 Hz and biased with alternating-current (AC) amplitude is 20 mV. The ionic

conductivity can be calculated using equation (5). The resistance can be obtained by fitting the Nyquist plot to the model circuit in **Fig. 1.8** using Zview software.

$$\sigma = \frac{L}{R \times S} \tag{5}$$

where σ is ionic conductivity (S/cm), L is the pellet thickness, S is the pellet area (cm^2) and R is the resistance (Ω) obtained from the measurement.
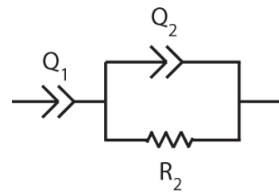

Fig. 1.7 | The equivalent circuit used for fitting impedance spectra. R_2 is a resistor and Q_1 and Q_2 are constant phase elements which are imperfect capacitors.

To measure the activation energies (E_a, eV), the impedances was taken in a hydrothermal oven at various temperatures (T, K). Conductivity at each temperature can be obtained at equilibrium as indicated by negligible difference from consecutive measurement. Based on the Nernest-Einstein relation (equation (4)) we mentioned before, the activation energy can be obtained from a plot of $\log(\sigma T)$ against $1/T$. Since $\log T$ does not vary much over a small temperature range, a simpler expression can be used by plotting $\log(\sigma)$ against $1/T$, each linear fitting should be qualified by coefficient of determination R^2 over 0.99.

$$\sigma = \frac{\sigma_0}{T} exp\left(-\frac{E_a}{kT}\right). \tag{4}$$

where σ_0 is a pre-exponential factor, T is the temperature, E_a is the activation energy and k is the Boltzmann constant.[44]

To understand the conduction contribution of cation, the transference numbers is measured by combining AC impedance and potentiostatic polarization techniques using symmetric cells, such as Li/electrolyte/Li cells. Usually, AC impedance test (10^6 to 1 Hz, 20 mV amplitude) can be measure for initial resistance (R^0) of the passivating layers. Then a constant small DC voltage (V, 20 mV) signal can be applied to symmetric cell, monitoring its initial current (I^0) till the current reaching a steady state current (I^s), which was followed by another AC impedance test to get steady-state resistance (R^s) of the passivating layers. The lithium-ion transference number can be calculated from equation (6).[45]

$$t_{Li^+} = \frac{I^s(V - I^0 R^0)}{I^0(V - I^s R^s)} \tag{6}$$

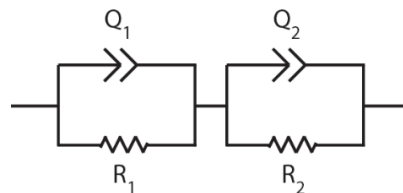The resistance can be obtained by fitting the Nyquist plot to the model circuit in **Fig. 1.8**.

Fig. 1.8 | The equivalent circuit used for fitting impedance spectra. R_1 and R_2 are resistors and Q_1 and Q_2 are constant phase elements which are imperfect capacitors.

1.7 Current approaches to solve lithium metal challenges

Several reviews papers have well summarized the recent development for Li-metal cells. There are four major challenges along with the development of the Li-metal anode. The first one is the formation and growth of Li dendrites during electrochemical deposition, which causes short circuit of the cell due to its penetration through the separator and eventually the thermal run-away.[46] The very recent accidents associated with Samsung Galaxy Note 7 has cost the company $5.3 billion for the recall. It would be considered much more severe if we switch to the lithium chemistry. The second challenge is related to plating and stripping process. The dendritic Li could also lead to an electrical detachment of Li from the current collector and become "dead Li", such unusable lithium significantly shortening the cycle life of the Li-metal cell. The third problem lies in the interfacial instability of Li metal in the organic electrolyte. Li metal has a high Fermi energy level and irreversibly reduces the liquid electrolyte, which results in formation of solid electrolyte interface (SEI) and decreases the Coulombic efficiencies. Meanwhile, such intrinsic high-reactivity of Li-metal with the organic electrolyte leads to side reactions on the Li-metal surface, results in electrolyte depletion and lower the conductivity. The fourth issue is the virtually infinite volume expansion of the electrode during Li deposition/dissolution. As a result, interfacial stability needs to be carefully controlled.[46]

Recently, various approaches have been adopted to resolve these issues of the Li-metal anode. The strategies for Li-metal batteries with liquid electrolytes are schematically summarized in **Fig. 1.9**. These strategies improve the Li-metal

anodes primarily by optimizing the organic electrolytes, and modifying the separators, constructing rational Li host materials, and protecting the Li interface via coating layers.[47] These methods are summarized here and the protection of Li-metal anodes with organic electrolytes is analyzed.
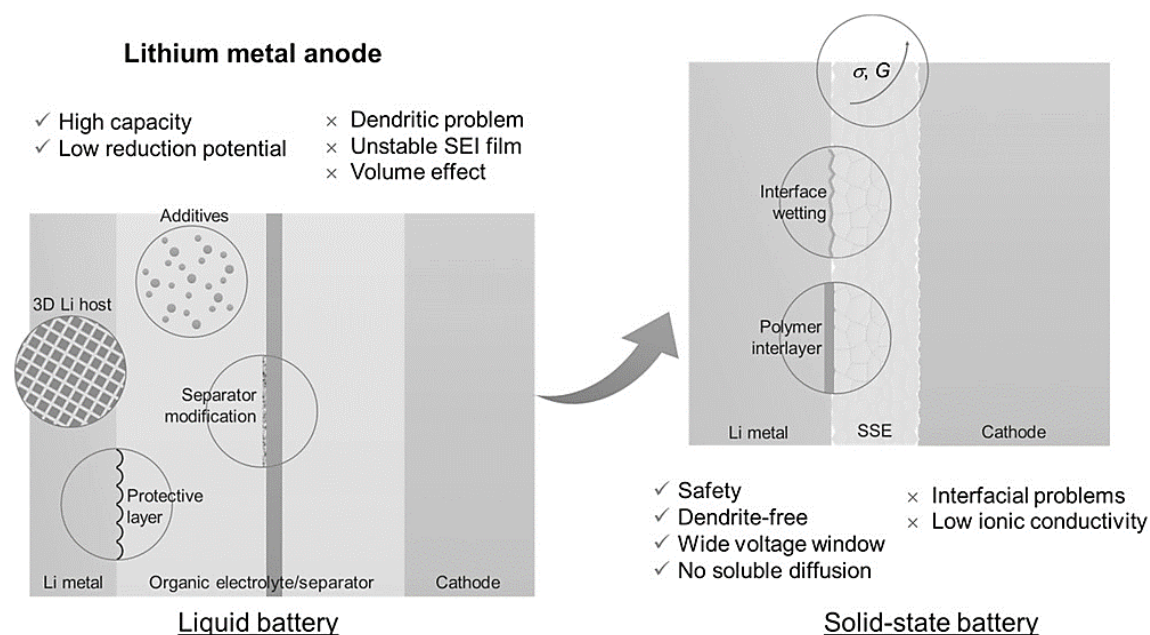
Fig. 1.9 | Development of Li-metal anodes from liquid batteries to solid-state batteries. Advantages and existing problems of Li-metal anodes and schematic of recent solutions for the Li-metal anode with organic liquid electrolytes (left). Advantages, problems, and current strategies to address the problems of Li-metal anode using SSEs (right).

While different approaches have been developed for Li-metal batteries using organic electrolytes, Li metal is thermodynamically unstable in organic electrolytes.[48] In other words, these methods are effective to extend the lifetime of Li-metal batteries, but could not solve the intrinsic instability of Li metal in liquid-

electrolyte batteries. limiting the development of Li-metal batteries.

On the cell configuration level, the Solid-state electrolytes (SSEs) can fundamentally change the behavior of Li deposition, and could be an ultimate solution to the issues of Li-metal anode in liquid electrolytes. SSEs permit stable Li-metal anodes, since the solid nature of the electrolyte can effectively block Li dendrites and provide a large electrochemical stability window (0–5 V), superior thermal stability, and direct multiple cell stacking for high voltage design.[49] This non-liquid system allows batteries to tolerate both high voltages and temperatures, which enable solid-state Li-metal batteries to be safer and possess higher energy densities than liquid electrolyte systems. Moreover, SSEs are single-ion conductors, and they have a high Li-ion transference number close to 1 and negligible electronic conductivity. In Li–S batteries, the SSEs can eliminate the poly- sulfide dissolution problems. Therefore, it is expected to resolve the problems of Li-metal anode in solid-state batteries. However, challenges remain on the interface between SSEs and electrodes due to thermodynamic instability in contact with Li-metal anode, limiting the development of Li-metal batteries. Moreover, low Li-ion conductivity of SSEs and the interfacial resistance of Li-metal and the solid electrolyte.

On the other hand, modification of lithium metal electrode through electrode framework design really make sense. The inhomogeneous Li-ion flux distribution usually leads to the non-uniform Li nucleation. The non-uniform Li nucleation on

the planar Li foil electrodes further induces the inhomogeneous Li deposition and dendrite proliferation. Superior to simple Li- foil anodes, Li-metal anodes with structure engineering, such as coated Li-powder electrode pressed on a current collector and Li-metal anode with microstructured surface (modified mechanically by microneedle or micropatterned stamp), are beneficial to uniform Li deposition.[50, 51] Recently, nanotechnology has greatly benefited the development of Li-metal anodes. Rational 3D electrode frameworks with novel architectures have been designed to control the Li plating/stripping behavior and improve the Li-metal anode stability. The ideal framework for Li-metal anode should hold a large specific surface area to reduce the local current density and create a homogeneous Li-ion flux, which is crucial for uniform Li-ion nucleation. Porous structure with sufficient pore volume in the Li substrate is desired to accommodate the Li volume change effectively upon cycling. In addition, the Li host substrate should possess mechanical and electrochemical stability, high electrical or ionic conductivity for fast electron/ion transfer, and a low gravimetric density for a high energy density.

Regardless the above-mentioned design, the interface is the key for all the design to work. Instead of forming SEI from native electrode electrolyte interaction, Li metal anode could be further stabilized through the interface engineering. An ideal interface requires high lithium conductivity, meanwhile, the current flux should be even by improving the cation concentration and contribution (transference number) and preferably mechanical stiffness.

Recently, a group of functional porous crystalline frameworks such as metal-organic frameworks (MOFs), or porous coordination polymers (PCPs) are becoming a hot topic of research. They are a class of compounds which consist of metal clusters or nodes linked by organic moieties. MOFs are highly crystalline and electrical insulators, are compatible with a wide range of mobile cations, and present regular pore networks that allow, in principle, swift ion movement. [52] Details will be given in the next section.

1.8 Interface Engineering by Functional Crystalline Porous Frameworks

Over the past decade, interest in the field of nanoporous materials has grown tremendously because of their outstanding performance and broad applications for uses such as in gas storage, gas separation, superhydrophobic interfaces, catalysis, energy conversion, energy storage, and optoelectronics. Chemists have found ways to prepare a wide variety of porous materials; however, it had proven difficult to synthesize organic polymer networks with discrete pores until the concept of reticular chemistry, which uses topologically designed building blocks, was proposed to construct these porous materials.

Previous reported solid lithium ionic conductors are attractive due to their inherent advantages in term of safety and device fabrication. However, their ionic conductivities at room temperature are typically more than an order of magnitude below the

requirement for normal battery operation. In contrast, organic liquid electrolytes feature very fast ionic transport properties ($>10^{-3}$ S cm^{-1}) but introduce the obvious flammability of carbonate solvents.[53]

Herein, it will be interesting to strategically combine the ability of high conductive liquid electrolytes with the rigidity of framework within one material that has a solid-like mechanical modulus for dendrites blocking and liquid-like room-temperature ionic conductivities for Li$^+$ transport. Many works along this direction have been carried out recently by the Archer group and Goodenough group in which polymer-based nanocomposites are used as the host for the loading of liquid electrolytes, including PVDF-HFP/Al$_2$O$_3$, PEO/Al$_2$O$_3$, and PVDF-HFP/PVP/Sb$_2$O$_3$. [54-56] As expected, these nanocomposites reveal a good mechanical strength to overcome the dendrites problems, providing an alternative approach to fabricate robust solid electrolytes. However, their nanopores are less controllable with relatively dynamic frameworks, which may allow dendrites to pass through causing a short-circuit.[57] Therefore, the goal of my current stage research is to utilize such frameworks for an artificial SEI and might be later for solid electrolyte for Li metal protection.

Both metal-organic frameworks (MOFs) and covalent-organic frameworks (COFs) are considered as excellent platforms to be explored. They are highly crystalline, electrically insulating features enable them the great candidate for ion transport. Their nanoporous feature, well-defined rigid pores, high surface area, large pore volume and open pore structure bring them highly designable (**Fig. 1.10**). Comparing to other well

know porous materials, MOFs and COFs can also introducing chemically functionalized pores, thereby combing intended chemical and physical properties to the materials.[58]
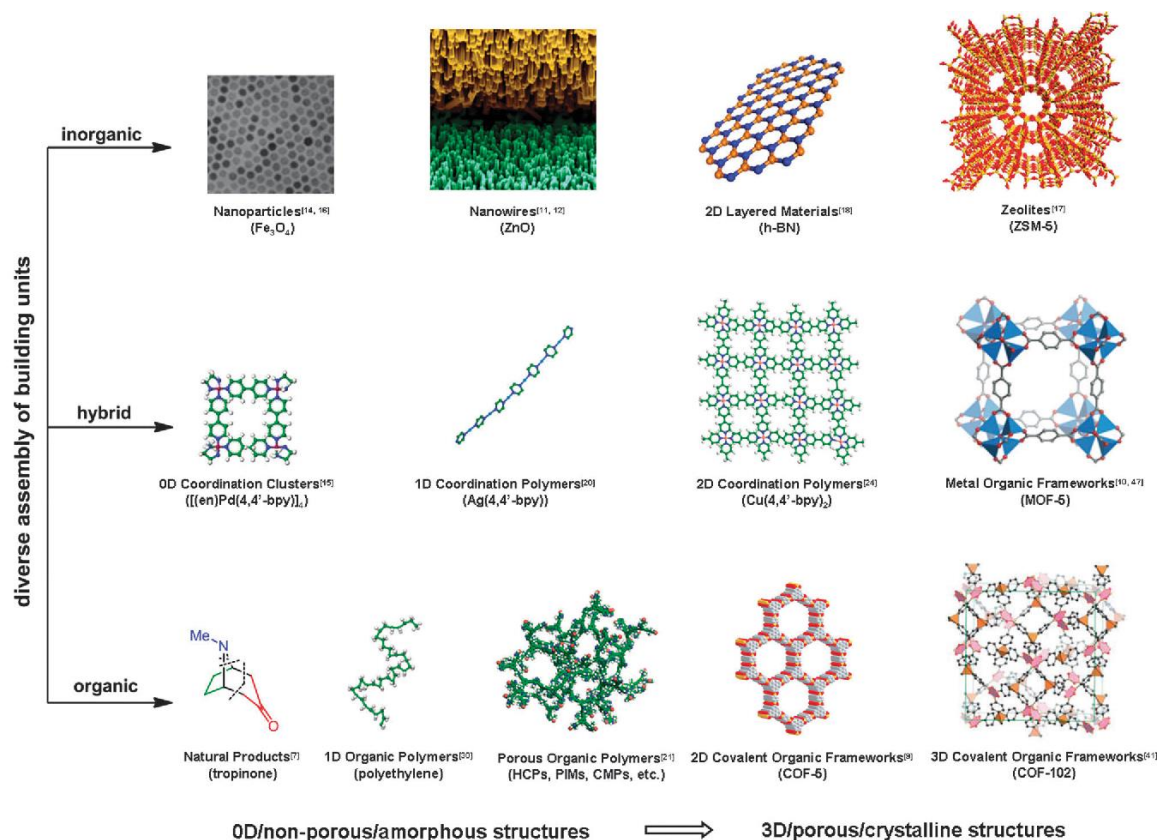

Fig. 1.10 | Selected examples for diverse assembly of building units to construct inorganic/hybrid/organic chemical architectures, ranging from the discrete 0D/non-porous/amorphous structures to the extended 3D/porous/crystalline structures. For clarity, many related systems, such as active carbons, mesoporous silicas, periodic mesoporous organosilicas, mesoporous carbons, and supermolecules are not included herein.

27

1.8.1 Metal-organic Frameworks (MOFs)

Utilizing reticular chemistry, the first family of porous materials to be synthesized was metal–organic frameworks (MOFs), which network polyatomic inorganic metal-containing clusters with polytopic linkers. Benefit from the coordination versatility of the constituent metal ions combines with the functional diversity of the organic linker molecules to create immense possibilities. There are various types of metal-organic frameworks (MOFs) including different classifications. Based on the different organic ligands we can divide MOFs into metal carboxylic acid frameworks[59], metal azolate frameworks[60], and mixed ligands frameworks. For metal carboxylic acid frameworks, it is easier to control the structures and modify the organic ligands, while the stability and predictability of the structures are better for metal azolate frameworks. These properties can be recognized by the framework design principles. For example, the sp^3 O atom in the carboxylate usually coordinates variably (typically up to three metal ions) (Figure 10). In comparison, each N-donor of azolate generally coordinates with only one transition-metal ion in the same direction as its lone electron pair as those in pyridines.[60]

As shown in **Fig. 1.11,** the rich chemical architecture of MOFs is founded on the structural diversity of the secondary building units (SBUs) – rendering MOFs permanently porous and mechanically stable. Numerous MOFs have been well investigated primarily for their gas adsorption properties as well as for possible application in sensing, drug delivery, catalysis, and optoelectronics.[61]
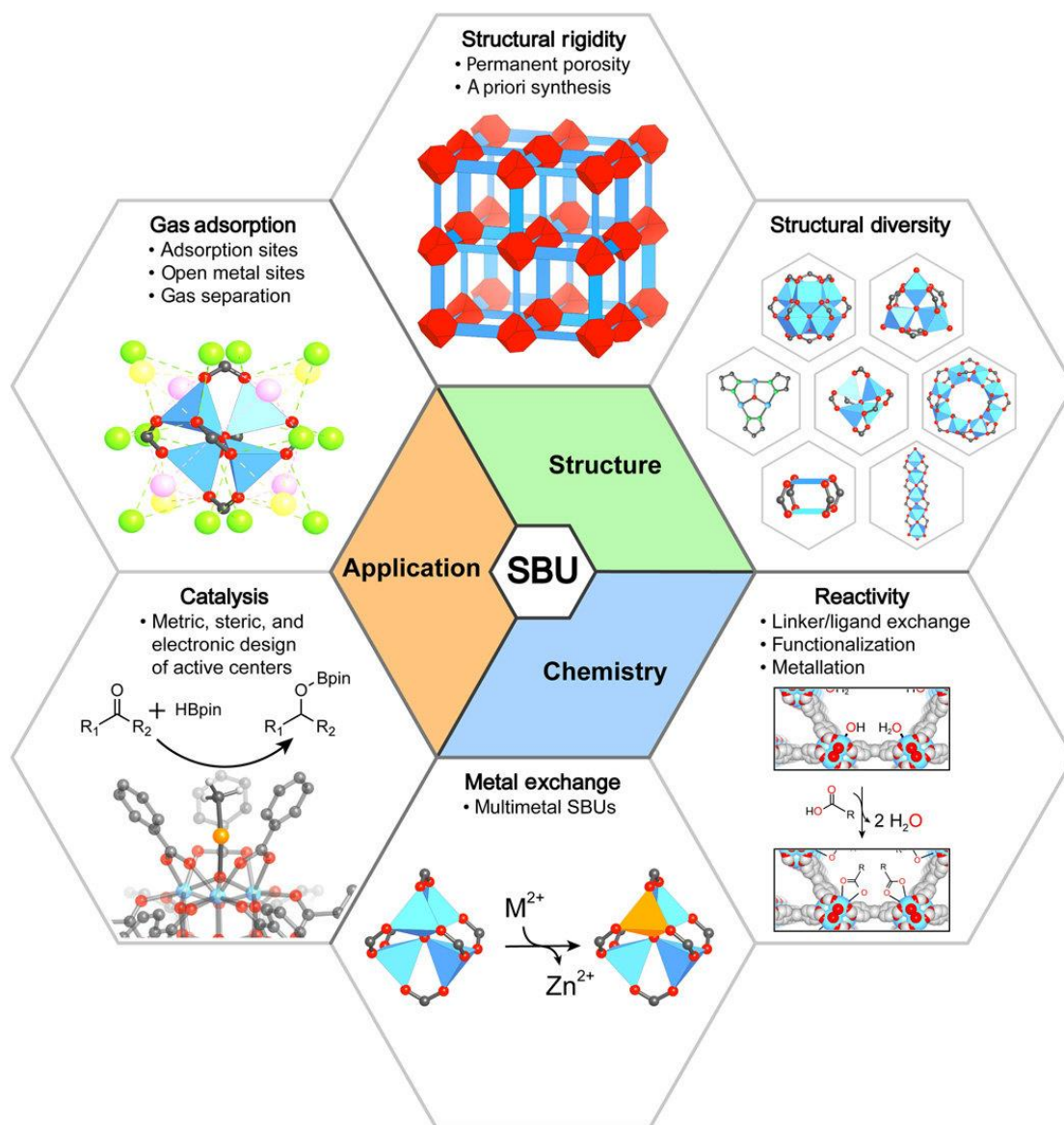
Fig. 1.11 | The impact of SBU on the structure, chemistry and applications of MOFs.[62]

Recently, the potential impact of these materials as solid electrolytes (composite) has been confirmed by numerous examples for high proton conductivity[63, 64], the exact mechanism for such conductivity improvement was not clearly mentioned.
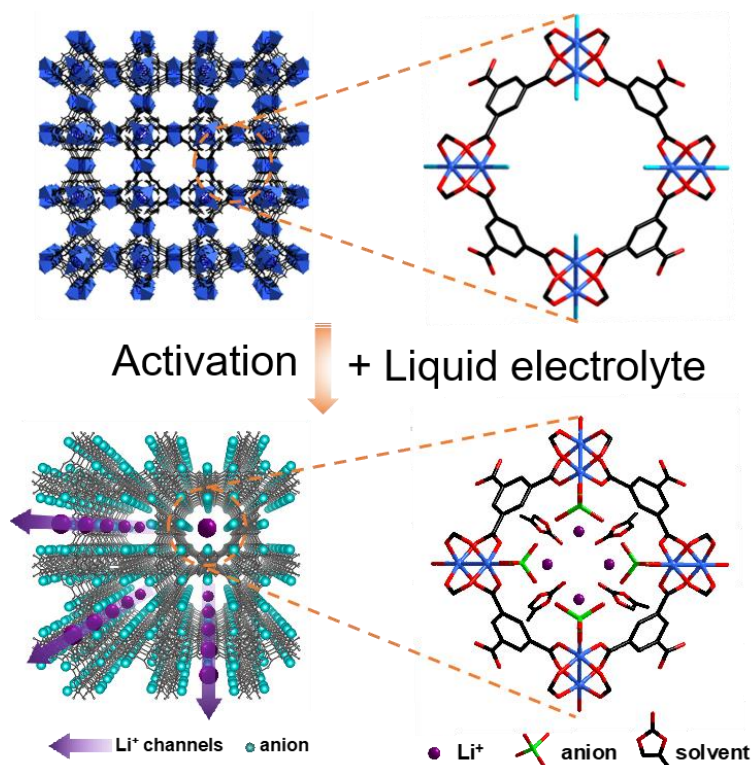
Fig. 1.12 | Schematic of biomimetic ionic channels in a MOF scaffold (dark gray) with bound ClO_4^- ions (cyan dots), enabling fast transport of solvated Li^+ ions (purple dots). Structure of HKUST-1 made from copper nodes (blue) and BTC ligands (black).[65]

Inspired by biomimetic ionic channels, artificial ionic channels constructed from MOF (e.g. HKUST-1, MIL-100) have been explored.[65] As shown in **Fig. 1.12**, HKUST-1 is constructed from Cu (II) paddle wheels and benzene-1,3,5-tricarboxylate (BTC) ligands (linkers) . Removing the coordinated solvent by heating, and results in open metal sites (OMSs). Removing the coordinated solvent results in nanoporous HKUST-1 scaffolds with open metal centers (OMSs). In the presence of $LiClO_4$ in propylene carbonate (PC; the solution is denoted as LPC), ClO_4^- ions complexes to the OMSs spontaneously, forming ClO_4^- decorated MOF channels, which renders the MOF scaffolds into ionic-channel analogs with fast lithium-ion conductivity and low

activation energy.

1.8.2 Covalent-organic Frameworks (COFs)

In 2005, Yaghi and co-workers demonstrated the utility of the topological design principle in their synthesis of porous organic frameworks connected via covalent bonds, which were the first successful examples of covalent organic frameworks (COFs).[66] COFs are covalent porous crystalline polymers that enable the elaborate integration of organic building blocks into an ordered structure with atomic precision. Since this landmark paper, the chemical synthesis of COFs has progressed significantly, and they show great potential for functional exploration. Because they are composed of light-weight elements linked by strong covalent bonds, COFs have low mass densities, possess high thermal stabilities, and provide permanent porosity.[67] As shown in **Fig.1.13**, COFs are composed of two main components: linkages and linkers. The molecular units chosen possess the functionality necessary to form specific linkages in a chemically and geometrically defined fashion to construct the framework material.
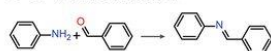
COF linkages

B−O bond formation
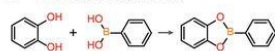
boronate ester, boroxine, borosilicate, spiroborate

C=N bond formation

imine, hydrazone, azine, squaraine, oxazole

C=N(Ar) bond formation
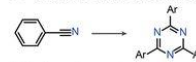
triazine, phenazine

C=C bond formation
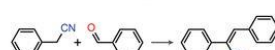
alkene

C−N bond formation
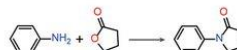
imide, β-ketoenamine, amide

B=N bond formation

borazine

COF linkers

I   II   III   IV   V   VI
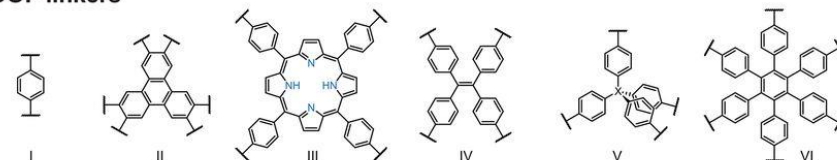
C=N(Ar) CTF-1 (**hcb**)
B−O COF-5 (**hcb**)
C=N COF-366 (**sql**)
C=N 4PE-1P-COF (**kgm**)
C−N PI-COF-5 (**dia**)
C=N HPB-COF (**hxl**)
B−O COF-108 (**bor**)
B−O COF-102 (**ctn**)

COF structures

CTF-1   COF-108
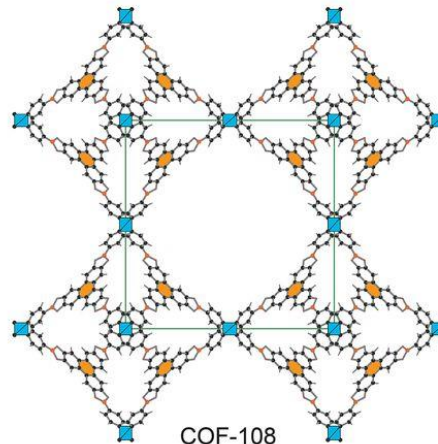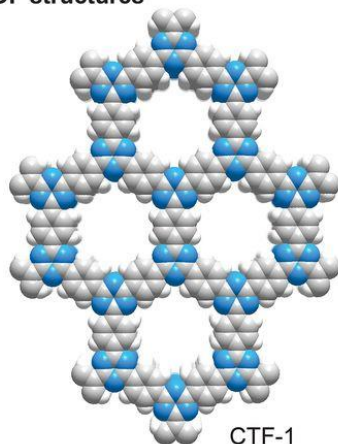
Fig. 1.13 | Linkages, linkers, and framework structures. Shown are examples of various linkages and linkers that have been used for building COFs.[68]

Depending on the dimensions of building block, COFs structure can be categorized into either two (2D) or three-dimensional (3D) COFs. 3D COFs, which extend this

32

framework three dimensionally through a building block containing a sp3 carbon or silane atom, characteristically possess high specific surface areas (in some cases larger than 4000 m^2 g^{-1}), numerous open sites, and low densities (as low as 0.17 g cm^{-3}). These features make 3D COFs ideal candidates for gas storage. The two-dimensional layered covalent organic frameworks (2D COFs) stack functional π-electron systems in van der Waals contact with maximal π-orbital overlap ideal for charge transport and exhibit open porous channels that run parallel to the direction of stacking.[69-73] 2D COFs have attracted intense contemporary interest as structurally precise materials for gas storage, optoelectronic devices, separation and catalysis since Yaghi and co-workers synthesized the first two 2D COFs containing 1, 4-benzenediboronic acid.[74] Up to now, most of the 2D COFs have been linked by boronate esters, as well as by triazine, imine, hydrazone, enamine, and borazine, in which their conductivities are not compared to the conductive polymers.[75] 2D COFs based on a porphyrin unit have demonstrated a good semiconducting property. However, their conductivity is not high enough for an electrode material because they are linked by boronate esters.

Chapter 2. MOF-Based Electrolyte Modulators for Lithium-Ion Batteries towards Electric Vehicle Applications

2.1 Introduction

Similar to other electrochemical devices, lithium-ion batteries experience polarization, which compromises their power output, energy efficiency, lifespan, and safety.[76] Generally, polarization of batteries is associated with charge/ion transport in the active materials and electrolytes, design and manufacture of the batteries, and how the batteries are charged and discharged, which is commonly catalogized as activation polarization, ohmic polarization, and concentration polarization.[77] Activation polarization arises from charge-transfer resistance at electrolyte-electrode interface; ohmic polarization is attributed to ionic resistance of electrolytes and electrical resistance of cell components; concentration polarization arises from ion-concentration gradient in electrolytes and active materials developed during charging and discharging. For a given battery, the overpotential due to ohmic polarization is dependent of charging and discharging current, while the overpotential due to concentration polarization is dependent of both current and duration of current applied, and a high current and long duration dramatically exacerbate the concentration polarization.[78]

Towards electric-vehicle applications, where fast charging, dynamic acceleration and regenerative braking require high-current charging and discharging of batteries, it is of particular importance to minimize polarization of the batteries.[79, 80] For example, fast charging a 90-kWh battery pack to 80% pack capacity in 15 min corresponds to a

charging power of 300 kW and a C-rate of 5, inevitably resulting in severe polarization.[81] During dynamic acceleration and regenerative braking, the polarization contributed by mass transport of electrolytes (ionic resistance and concentration gradient) accounts for a significant portion of the total polarization. For example, in a hybrid pulse power characterization (HPPC) test of batteries designed for hybrid electric vehicles, polarization of electrolyte contributed to 43 % of the total polarization. In addition, the contribution increased to 65 % in an ISO (International Standard Organization)-energy-cycle test where the current loads are higher and applied for longer times. Consistently, contribution of concentration polarization of electrolyte increased from ~ 15% of the total polarization in the HPPC test to 35% in the ISO-energy-cycle test.[82]

Minimizing the ionic resistance and concentration polarization of electrolytes, in the context of electric vehicle applications, is highly critical, which can be achieved through increasing the ionic conductivity and lithium-ion transference number t_{Li}^{+} of electrolytes. Nevertheless, lithium-ion batteries are operated as a system that requires simultaneous and synergistic functioning of their constituting components; malfunction of a component may compromise the performance and result in device failure. For example, low-viscosity solvents (e.g., nitrile) were used as co-solvents for traditional carbonate electrolytes, which gives rise to high ion mobility and alleviates the ohmic polarization.[83, 84] However, the use of such nitriles often deteriorates the passivation layers on electrodes and compromises cycle life of the batteries. Various strategies have been explored to increase t_{Li}^{+} and mitigate concentration polarization, which

include adopting highly concentrated electrolytes and bulky anions, grafting anions onto polymers, and complexing anions with inorganic particles.[85, 86] Such strategies lead to improved t_{Li}^+ but at cost of ionic conductivity.[87, 88] For example, highly concentrated electrolyte, 7 M LiTFSI in DME and 1,3-dioxolane (DOL), provides a high t_{Li}^+ of 0.73 yet with an ionic conductivity 90% lower than its 1.0 M counterpart.[89] Grafting the anions of electrolytes on polymers resulted in electrolytes with t_{Li}^+ higher than 0.8, yet with ionic conductivities two to three magnitudes lower than the liquid-electrolyte counterparts.[90] Besides ionic resistance and concentration polarization of electrolytes, electrode-electrolyte interface could also significantly contribute to the total polarization. To date, various electrolyte additives have been explored, which assist to stabilize electrolyte interface and prolong cell lifetimes at lower rates. The use of such additives, however, also results in the formation of resistive solid electrolyte interphase (SEI) films, which compromises the performance at higher rates.[91, 92] From a systematic perspective, developing electrolyte systems, which can simultaneously provide high t_{Li}^+, high ionic conductivity, stable and low-resistivity electrolyte interface, is critically important yet highly challenging.

We envision that this can be achieved by using an electrolyte modulator that is based on metal organic framework (MOF), exemplified herein by UMCM-309a, a MOF constructed from hexanuclear zirconia (Zr_6) building clusters and 1,3,5-tris(4-carboxyphenyl)benzene linkers (BTB) (**Fig. 2.1b**). UMCM-309a possesses a two-dimensional (2D) structure with an interlayer spacing of 7.01 Å and elliptical pores with a pore-window size of 7.2 Å × 12.6 Å.[93] In electrolytes containing lithium

bis(trifluoromethanesulfonayl)imdie (LiTFSI) (1.0 M in DME and DOL with 1:1 volume ratio), UMCM-309a adsorbs LiTFSI from the electrolytes and concentrates it within the pores, owing to the similar sizes of the pores and TFSI$^-$ anions (2.9Å × 8.0 Å)[94]. Meanwhile, open metal sites (OMSs) in UMCM-309a can be readily generated upon removal of the hydroxyl groups and terminal H_2O molecules from the Zr_6 sites (**Fig. 2.1b**), which complex with the anions with altered ion-pair interactions, leading to increased t_{Li^+} and high ionic conductivity.

Furthermore, preferrable adsorption and complexation of the anions afford UMCM-309a with surface charge, which enables electrophoretic incorporation of UMCM-309a with high ionic conductivity into SEI films, forming electrolyte interface with low resistivity and high modulus (Fig. 1b). Note concentration polarization of electrolyte occurs especially during high-rate operation, where rapid consumption of lithium ions causes lithium-ion deficiency near electrodes and the resultant unbalanced anions are subsequently repelled from the region, resulting in a Li-salt concentration gradient and a reverse potential against the cell voltage.[95-97] Nevertheless, with the presence of UMCM-309a in the SEI films, unbalanced anions are immobilized within the deficient region, which results in a negative electric field assisting to recruit surrounding lithium ions and suppress the concentration polarization. Combining high t_{Li^+}, high ionic conductivity, and the ability to form robust electrolyte interface with low resistivity and anti-concentration-polarization capability (**Fig. 2.1a**), such a MOF-based electrolyte modulator, denoted as hereinafter ITM, afford a simple yet effective approach to mitigate polarization of electrolyte, the major component of battery

37

polarization in electric vehicles.

2.2 Experiment methods

2.2.1 Synthesis of IMP.

The IMP was synthesized according to a reported hydrothermal approach.[98] Briefly, $ZrCl_4$ (0.37 mmol) and BTB (0.25 mmol) were dissolved in 30 mL of dimethylformamide (DMF) and 10.75 mL of 12 M HCl. The mixture was sealed in a Teflon lined autoclave and heated at 120 °C for 2 days. After cooling to room temperature, the IMP powders collected by centrifugation were successively washed by DMF for 3 times and by acetone over 3 days. The sample was dried at 120 °C overnight and further heated at 350 °C (under vacuum) for 12 h to thermally activate the IMP. The activated IMP were dispersed into liquid electrolytes (LFS/LPF from BASF, home-made LBF) at a 1wt. % (in an Argon-filled glove box). The resulting colloidal-like suspension was ultrasonicated for 30 min and magnetically stirred overnight to achieve homogeneity.

2.2.2 DFT calculations.

All computations were performed by means of spin-polarized DFT methods using the DMol³ code.[99, 100] The generalized gradient approximation (GGA) and the Perdew-Burke-Ernzerhof (PBE) exchange-correlation functional were employed.[101] The van der Waals interactions were described using the empirical correction in the Grimme

scheme, and the density functional semicore pseudopotential (DSPP) was adopted for the relativistic effects of transition metal atoms, in which the core electrons are replaced by a single effective potential with some degree of relativistic corrections introduced into the core.[102, 103] The double numerical plus (DNP) polarization was chosen as the basis set for other elements.[99] Self-consistent field (SCF) calculations were performed with a convergence criterion of 10^{-6} au on the total energy of electronic computations. To ensure high quality results, the real-space global orbital cutoff radius was chosen as high as 5.3 Å and thermal smearing with a width of 0.01 Ha was applied to the orbital occupation to speed up the convergence. Since the simplified IMP cluster structure was placed in a length of 60 Å box cube, the Monkhorst-Pack k-point sampling of $1\times1\times1$ mesh were used in this calculation.[104]

2.2.3 In situ Raman.

A Raman spectrometer (Dilor, SuperLabram II) equipped with 633 nm laser and a custom-made Cu|Li cell with quartz window was used to analyze the electrolyte concentration in vicinity of Cu during Li^+ plating. The cells injected with 5 mL of electrolyte were assembled and sealed in the glove box. The distance between electrodes (1 cm^2) was fixed at 0.3 cm and the laser beam was focused on the neighboring Cu foil at a fixed position (0.1cm). The spectra were collected every 1 min upon applying the plating current of 3 mA cm^{-2} at Cu.

2.2.4 Finite element simulation.

The LiFePO$_4$|Li conceptual cell was modeled on COMSOL Multiphysics® by using the Batteries and Fuel Cells Module platform on the basis of the pseudo two-dimensional (P2D) model developed by Newman et al. [78, 105]The parameters inputs in the simulation, which based on the experimental data accordingly, were listed in the **Table 2.3**. The LiNi$_{0.5}$Co$_{0.3}$Mn$_{0.2}$O$_2$|graphite conceptual cell for DST simulation used Batteries and Fuel Cells Module on the basis of the pseudo two-dimensional model developed by Newman et al. [78]And the parameter inputs in the simulation were based on the experimental data, which were listed in Table **2.4**.

2.2.5 Electrochemical characterizations.

The measurement of ionic conductivity was carried out in a home-made electrolyte cell, where two identical titanium plates (1×1 cm^{-2}) served as blocking electrodes. The reference conductivities of LFS and LPF were acquired from the manufacturer datasheets. The ionic resistance was estimated by the extrapolated interception of the Nyquist plots with the real axis. The determination of t_{Li}^+ was performed through the combination of EIS technique and potentiostatic polarization. The Li|Li cells were polarized by a constant voltage bias of 20 mV (ΔV) for 1 h, during which the initial current (I_0) was monitored until reaching the steady-state current (I_{ss}), and the interfacial resistance was recorded by the EIS before (R_0) and after (R_{ss}) the potentiostatic polarization. The t_{Li}^+ thereby could be calculated with the following expression: $t_{Li}^+ = I_{ss} (\Delta V/I_0R_0)/(I_0(\Delta V/I_{ss}R_{ss}))$.[106] The CV tests (Biologic VMP3) were conducted in SS|Li cells at scan rate of 1 mV s^{-1} between -0.2 V and 5 V (*vs.* Li/Li$^+$).

2.2.6 Li-metal cell tests.

The LiFePO$_4$ cathode sheets were prepared by mixing LiFePO$_4$ (Shenzhen Dynanonic Co), super P, and polyvinylidene fluoride (PVDF) with a weight ratio of 90:5:5 in N-methyl-2-pyrrolidone (NMP). The resulting slurries were uniformly coated on carbon-coated Al foils and dried in a vacuum oven at 120 °C for 24 h. The half-cell (LiFePO$_4$|Li) tests were performed with coin-type cells (CR 2032), polyethylene-based separator (Celgard, 25 μm), thin Li foil (40 μm) and 60 μL of LFS-based electrolyte. Three-electrode flow cell (LiFePO$_4$|Li|Li) tests were carried out in a commercial air-tight split cell (MTI) (see schematic in **Figs. 2.12a-b**), which was assembled by LiFePO$_4$ (12 mm), Li disk (14 mm) and Li foil as cathode, anode and reference electrode, respectively. The reference was inserted between cathode and anode with separations of glass fiber membranes (Whatman, GF/C) and 2 mL of LFS-based electrolyte. All cells were fabricated in an Argon-filled glove box (O$_2$/H$_2$O < 1 ppm). The galvanostatic cycling of cells were performed between 2.5 to 4.2 V (vs. Li/Li$^+$) with 1C-rate equals to 140 mA g^{-1}. Before the pulsed 50C discharge tests, the LiFePO$_4$|Li cells were charged to 4.2V by a low rate of 0.3C. The loading levels of LiFePO$_4$ for three-electrode and rate tests were 2-3 mg cm^{-2} and a higher ~ 6 mg cm^{-2} loading was applied for the long-term cycle tests (2C).

2.2.7 Pouch-type full cell tests.

Dry (without electrolyte) and sealed LiNi$_{0.5}$Co$_{0.3}$Mn$_{0.2}$O$_2$|graphite pouch cells (200 mAh, balanced at 4.4 V) were purchased from Li-FUN technology, where the single

side loadings of the anode were 12 mg cm^{-2}. The cells were opened, dried, electrolyte-filled (LPF-based) and sealed in the glove box. Afterwards the cells were rested for 24 h, charged under 10 mA (0.05C) to 3.5 V, and then held at 3.5 V until the currents dropped below 0.05C. The activated cells were degassed and replenished with electrolyte in the glove box. The total added volume of electrolyte was 0.85 mL. The conventional DST protocol was scaled to C-rates, where 5C discharge herein corresponds to the maximum peak power output. Voltage cutoffs of 4.2 V and 4.4 V were applied for galvanostatic cycling (400 mA) and full-DST-cycles (heavy-duty), respectively. All electrochemical tests were conducted at ambient temperature (25 ℃) and minor temperature fluctuation may have occurred due to facility management.
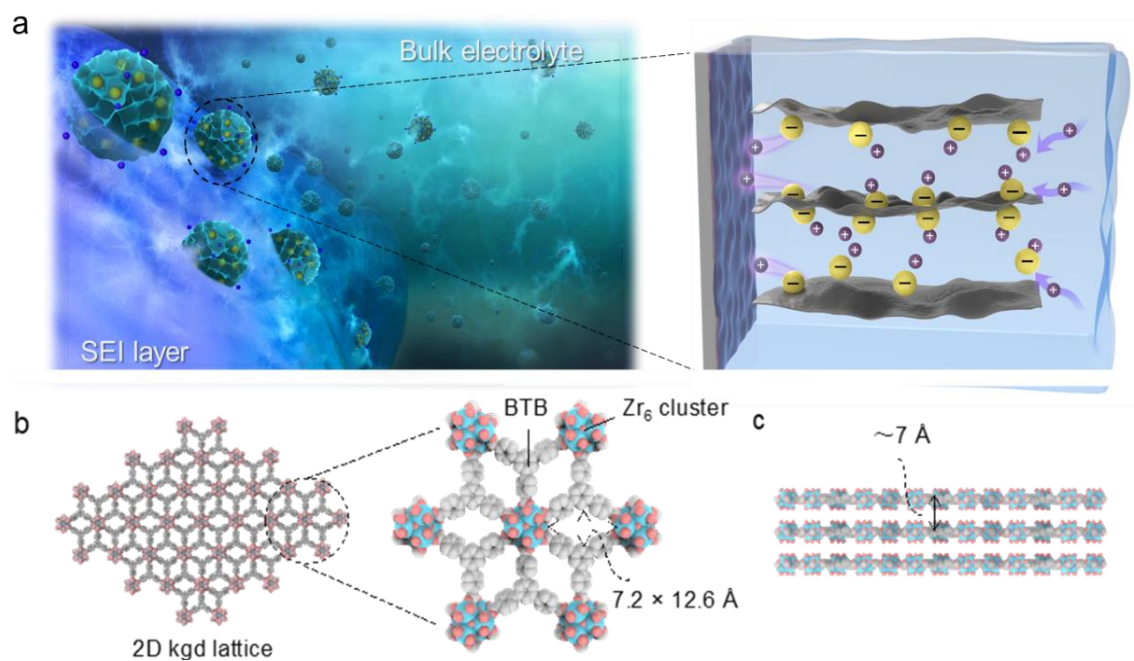
2.3 Results and Discussions

Fig. 2.1 | A FAIM strategy for mitigation of concentration polarization in lithium ion batteries. **a**, A schematic illustrates a FAIM layer formed on an electrode with incorporated IMP. The incorporated IMP create an electric field upon occurrence of lithium-ion deficiency, which assists to recruit the surrounding lithium ions and depress the polarization. Structural representation of IMP with kgd topology (blue, pink and grey spheres represent Zr, O and C atoms, respectively): **b**, top-down views and **c**, cross-sectional view.

Such a field-assisted-ion-modulation (FAIM) strategy is illustrated in **Fig. 2.1a-b**, where UMCM-309a, a metal organic framework (MOF). is used as ion-transport modulation particles (denoted as IMP) in electrolytes of lithium bis(trifluoromethylsulfonyl)imide (LiTFSI). UMCM-309a, constructed from hexanuclear zirconia (Zr_6) building clusters and 1,3,5-tris(4-carboxyphenyl)benzene linkers (BTB), exhibits a layered structure (interlayer spacing 7.01 Å) with elliptical pores (pore-window size 7.2 Å × 12.6 Å).[107] The size of the TFSI$^-$ anions (2.9Å × 8.0 Å)[94] well matches the pore size, allowing their effective adsorption within UMCM-309a.   Meanwhile, the hydroxyl groups and terminal H_2O molecules in the Zr_6 sites can be readily removed by heat treatment, which generates open metal sites (OMSs) that complex with the anions. The complexation also liberates the associated lithium ions, collectively leads to increased t_{Li+} and lithium-ion conductivity. In addition, the adsorption and complexation of the anions afford IMP with net surface charge, allowing

43

their spontaneous electrophoretic deposition onto the electrodes during during charging and discharging, forming robust FAIM coatings (high modulus of $\approx$23.47 GPa).

As illustrated in **Fig. 2.1b**, the IMP (UMCM-309a) is composed by 6-connected hexanuclear Zr_6 basic building blocks and 3-connected tritopic 1,3,5-tris(4-carboxyphenyl)benzene linkers (BTB^{3-}), infinitely augmenting to a 3,6-connected 2D network with an overall kagome dual (kgd) topology.[98] In the Zr_6 cluster, each Zr atom coordinates to two μ_3-O^{2-} O atoms, one μ_3-OH$^-$ group, two O atoms from two BTB links, one terminal OH$^-$ group, and one H_2O molecule. The resulting $Zr_6(\mu_3\text{-O})_4(\mu_3\text{-OH})_4$ octahedral cores connected by trigonal carboxylate ligands generate elliptical windows with a size of 7.16 × 12.61 Å (atom-to-atom distance).[108] The stacking of the monolayer by an interlayer spacing of 7.01 Å gives rise to a 2D structure resembling other prominent 2D materials (**Fig. 2.1c**).
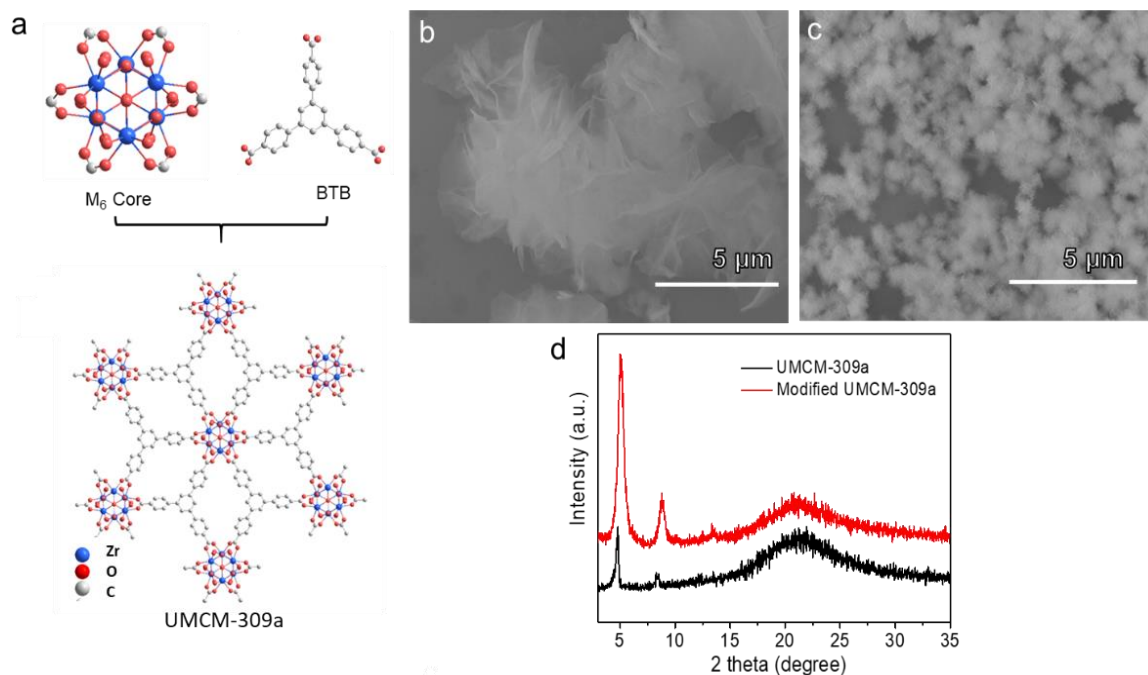
Fig. 2.2 | Synthesis of UMCM-309a. **a**, A schematic of UMCM-309a synthesis route. **b**, SEM image of UMCM-309a synthesis by original literature method. **c**, SEM images of modified UMCM-309a. **d**, PXRD patterns of UMCM-309a and modified UMCM-309a.

The UMCM-309a was synthesized according to a reported hydrothermal approach, [109] the simplified synthesis route is illustrated in **Fig. 2.2a**. We modified the particle size by dilute the solvent. From the scanning electron microscopy (SEM) images, we can see the particle size of UMCM-309a is obviously shrink from approximately 9 μm in diameter (**Fig. 2.2b**) to 400 nm of the modified method (**Fig. 2.2c**). The nanoscale particles enable a better dispersion in the solvent and larger surface area to participate the potential reactions. And from the powder X-ray diffraction (PXRD) pattern (**Fig.**

2.2d), the as-synthesized UMCM-309a maintains the same structure as the reported one.
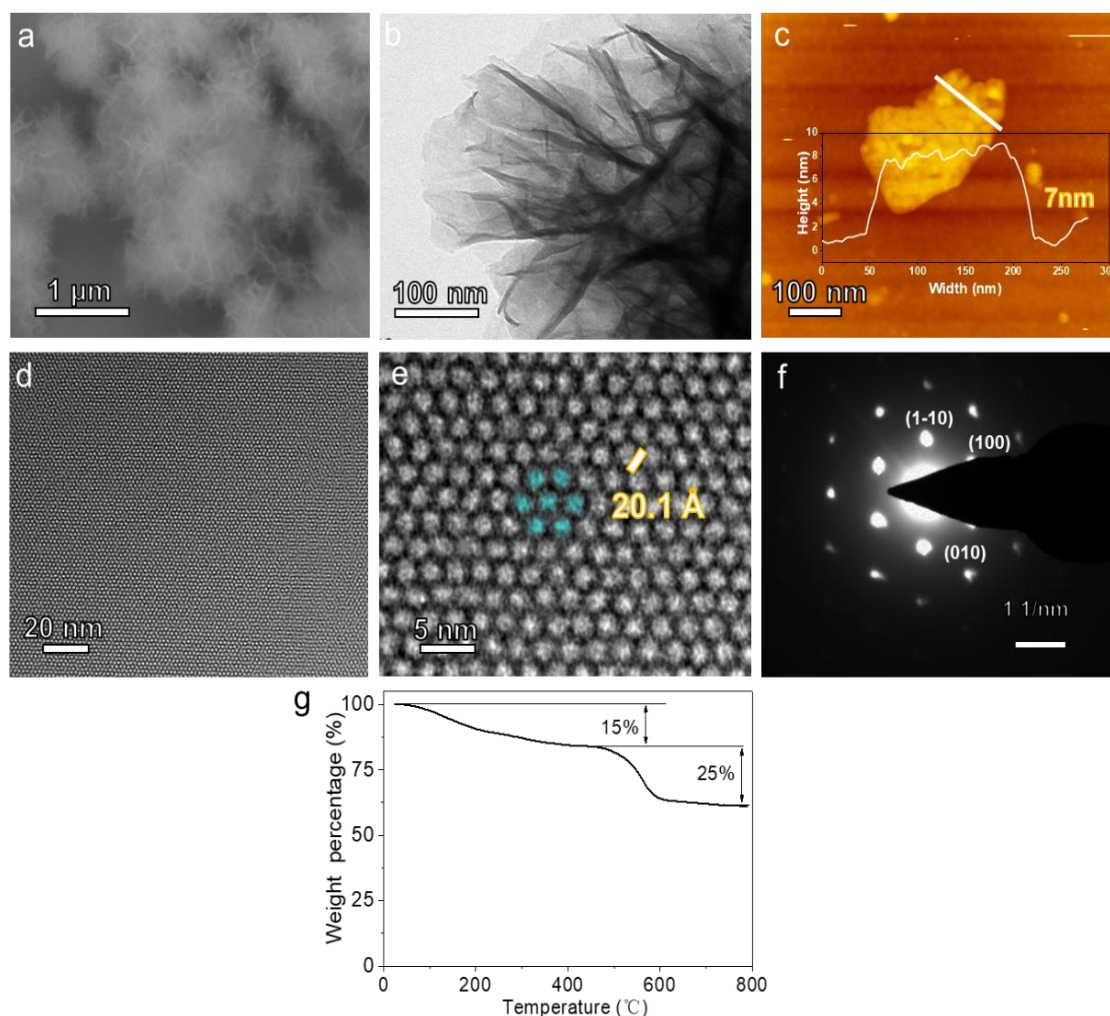
Fig. 2.3 | Physical characterization of as-synthesized UMCM-309a. **a**, SEM images of UMCM-309a. **b**, TEM image of a UMCM-309a particle.**c**, AFM micrograph and height distribution of UMCM-309a measured along the white line. **d-f**, HRTEM images and h, SAED pattern of modified UMCM-309a that are composed of nanosheets exhibiting highly ordered microporous structure. **g**, TGA curve of pristine UMCM-309a in Argon flow.

Its microstructure and morphology were further imaged by SEM (**Fig. 2.3a**),

transmission electron microscopy (TEM, **Fig. 2.3b**), The as-synthesized UMCM-309a exhibits flower-like spherical assemblies composed of wrinkled 2D nanosheets. The particulate size of the assemblies, the average nanosheet size, and the thickness were approximated to 800 nm and 150×300 nm^2, respectively. And through atomic force microscopy (AFM, **Fig. 2.3c**), the thickness was measured approximately 7 nm. The PXRD pattern (**Fig. 2.2d**) of the sample gives only three broad peaks, where the calculated d spacing of d (001) = 8.3 Å corresponds to the theoretical interlayer spacing. To confirm the 2D structure further, high-resolution TEM (HR-TEM) was analyzed. The HR-TEM image along with the selected area electron diffraction (SAED) pattern show clear lattice fringes with the dark spots representing Zr$_6$ clusters (**Fig. 2.3d**). The HR-TEM imaging in dark field mode evidently verifies the proposed kgd topology of Zr$_6$ clusters as determined by the arrangement of the bright spots (**Figs. 3.3e-f**). Meanwhile, the measured distance between adjacent clusters (20.1 Å) is consistent with the basic parameter of a hexagonal unit cell (a=b = 20.06 Å).[109] The TGA curve (**Fig. 2.3g**) displays two segments of weight loss. The first gradual loss of 15% up to 400 °C is ascribed to the elimination of guest molecules and capping hydroxyl groups.[98] The subsequent second loss of 25% arises from the decomposition of organic linkers (BTB) or structural collapse, supporting the superior thermal stability of UMCM-309a. Thus, the activation temperature 350°C was determined.
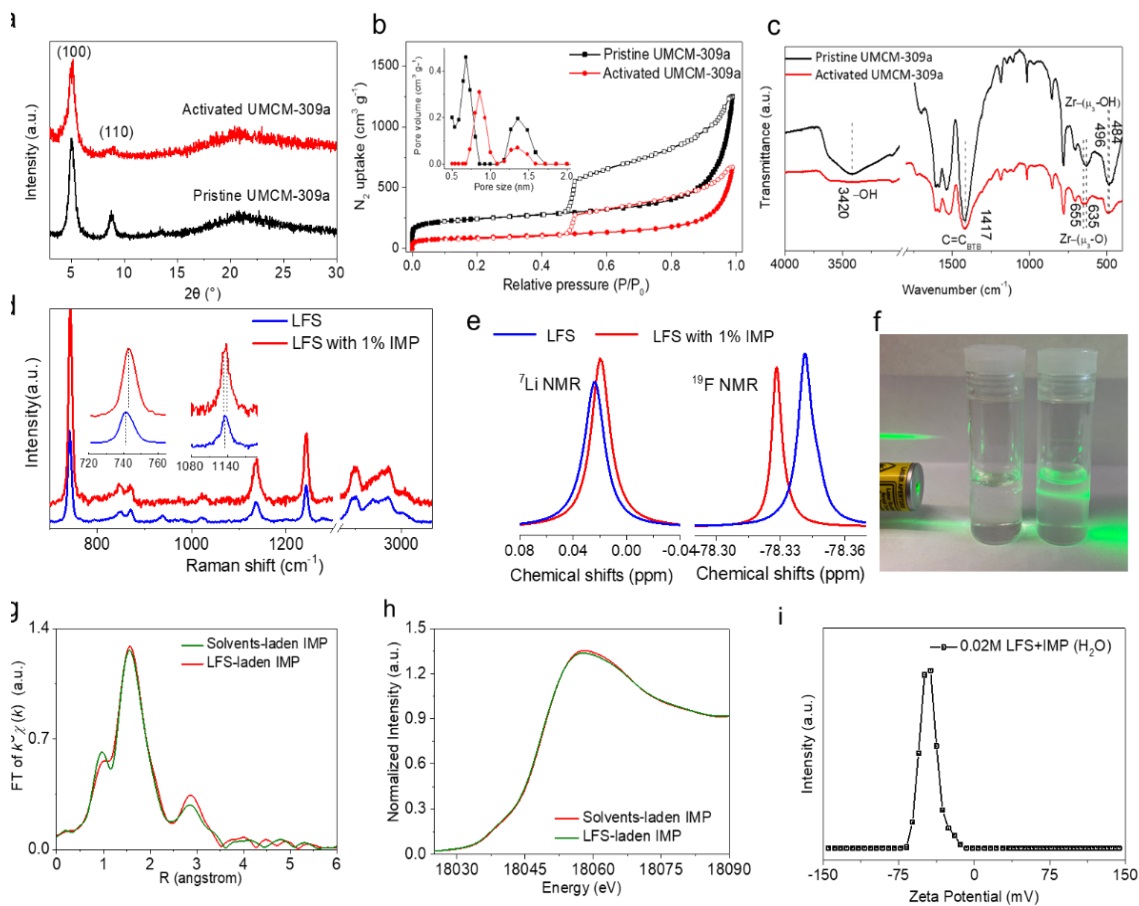
Fig. 2.4 | Physical characterization of activated UMCM-309a and electrolyte with IMPs.

a, PXRD patterns of pristine UMCM-309a and activated UMCM-309a. **b**, N₂ adsorption isotherms of pristine and activated UMCM-309a measured at 77 K, and the experimental pore size distributions calculated from adsorption data using the DFT slit-pore model (inset). **c**, IR spectra of pristine UMCM-309a and activated UMCM-309a. **d**, Raman spectra of the electrolytes (1.0 M in LiTFSI in 1,3-dioxolane (DOL) and 1,2-dimethoxyethane (DME), denoted as LFS) with and without IMP. Inset showing the spectra for S-N-S and SO₂ vibrations. **e**, ⁷Li and ¹⁹F NMR spectra of the electrolytes with and without IMP. **f**, A photograph showing Tyndall effect in solutions with different compositions: (left) LFS; (right) LFS with 1% IMP additives. **g**, R-space of

the extended x-ray absorption fine structure (EXAFS) spectra of IMP in DOL/DME with and without LiTFSI. **h**, Zr K-edge EXAFS spectra in R-space. **i**, Zeta potential of 1% IMPs in 0.02 M LiTFSI aqueous solution.

The open metal sites (OMSs) were exposed, or activated, by thermal treatment at 350 ℃ under dynamic vacuum. The structural integrity and evolution of the activated IMP were further probed by PXRD, N_2 isotherms, and infrared spectroscopy (IR). A slight broadening of the diffraction peaks was observed for the PXRD of activated IMP (**Fig. 2.4a**), indicating a well-preserved crystal structure with minor loss of crystallinity. The pore structure of IMP was further characterized by nitrogen adsorption/desorption isotherms. As shown in **Fig. 2.4b**, the pristine IMP exhibits a high Brunauer–Emmett–Teller (BET) surface area 831 $m^2\,g^{-1}$, and a huge N_2 volume uptake at relative pressure (P/P$_0$) between 0.5 and 1, which is attributable to the numerous slit-like marcopores formed by the nanosheet assemblies. In addition, the corresponding pore size distribution derived from Density Function Theory (DFT) model manifests two micropores at 6.8 and 13.7 Å, which correspond to the interlayer spacing/small planar opening and large planar opening, respectively. There was an increased pore size from 6.8 to 8.6 Å compared with the pristine sample, which originate from nanosheet shrinkage and expanded interlayer spacing due to the departure of hydroxyl, respectively.[110] **Fig. 2.4c** compares the IR spectra of pristine and activated IMP. The IR vibrations at 1417 cm^{-1} (C=C) pertaining to organic linkers (BTB) are marginally unaffected after activation. While the signal at 484/635 cm^{-1} associating with Zr–(μ_3-

O)/Zr–(μ_3-OH) and the board peak at 3420 cm^{-1} associating with –OH respectively display shifted positions and vanishing intensity, verifying the generation of OMSs.[111] To investigate the interactions between LFS and IMP, Raman spectroscopy was performed on LFS and LFS with 1% IMP (by weight). As shown in **Fig. 2.4d**, the intensive peaks appearing at 741, 1136, and 1242 cm^{-1} belong to the signature S–N–S bending vibration, and the SO$_2$ and CF$_3$ symmetric stretching vibrations of anions (TFSI$^-$), respectively.[112] A group of peaks between 2800 and 3050 cm^{-1} represent the stretching vibrations in the C–H bond of the solvents (DOL/DME). Upon the addition of IMP in LFS, both CF$_3$ and C–H peaks exhibit a minor change, while the S–N–S band appreciably shifts from 741 to 743 cm^{-1} and the SO$_2$ band splits into two peaks (1132/1138 cm^{-1}), clearly signifying the breakdown of anion structural symmetry and the alteration of its coordination status.[111] As shown in **Fig. 2.4e**, the local chemical environments of Li$^+$ and TFSI$^-$ ions in LFS and LFS with 1% IMPs were further studied by nuclear magnetic resonance (NMR) spectroscopy. The ^{7}Li NMR spectra of LFS and LFS with 1% IMP show a subtle chemical shift relative to the well discernable shift found in their ^{19}F NMR spectra, illustrating analogous NMR spectroscopic behavior of Li$^+$ ions while showing a distinct chemical environment of TFSI$^-$ ions bound on IMP. The ultrasonic dispersion of activated IMPs in LFS yields a colloidal suspension as evidenced by a significant Tyndall effect under laser radiation (**Fig. 2.4f**). Synchrotron powder X-ray adsorption spectroscopy (XAS) was employed to elucidate the local structure of Zr$_6$ clusters. The X-ray absorption near edge structure (XANES) and extended X-ray absorption fine structure (EXAFS) provide information regarding the

oxidation state and coordination status of Zr^{4+}, respectively. The solvents (DOL/DME)-laden IMP was compared with LFS-laden IMP to study the impact of LiTFSI on Zr-based OMSs. As shown in **Fig. 2.4g**, the white line of Zr K-edge in XANES spectrum shows no obvious change with addition of LiTFSI, suggesting the same Zr^{4+} valence state. [113] **Fig. 2.4h** shows the R-space of EXAFS spectra, the first peak at 1.6 Å is due to the contribution of the nearest Zr-O, while the second peak at 2.9 Å is attribution to the Zr-Zr, respectively.[38,39] Relative to the reference sample without LiTFSI, the sample loaded with LiTFSI shows increased peak intensities particularly for the higher R-peak (2.9 Å), signifying new coordination of LiTFSI to Zr sites.[114] Thus, Zr in LFS-laden IMP can from new coordination with LiTFSI, deeply impacting on the electrochemical performance of LiTFSI in DOL/DME electrolyte. The ability to adsorb and complex anions confers IMP negative surface charge (e.g., a *zeta* potential of - 45 mV in 0.02 M aqueous LiTFSI solution), enabling their electrophoretic deposition on electrodes (**Fig. 2.4i**).
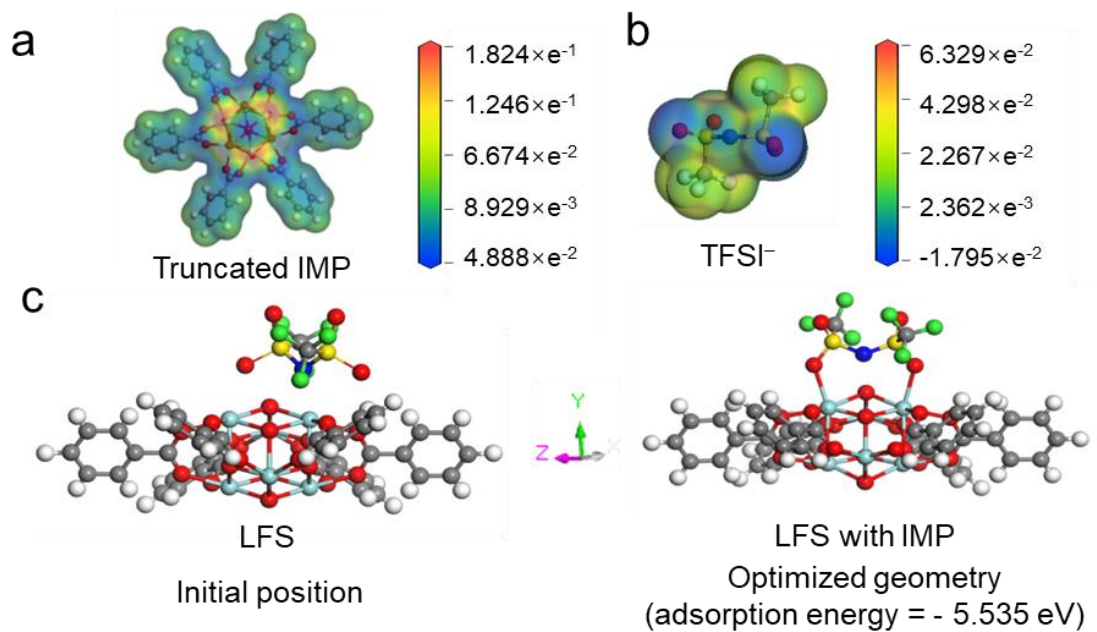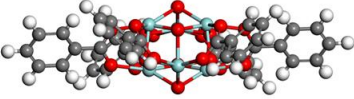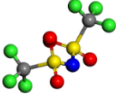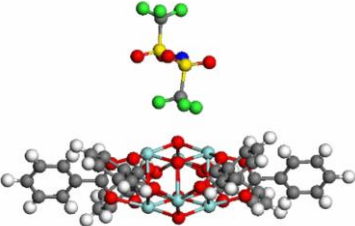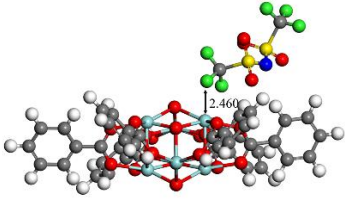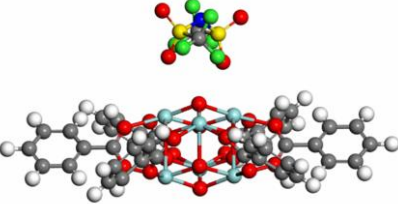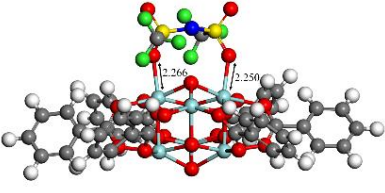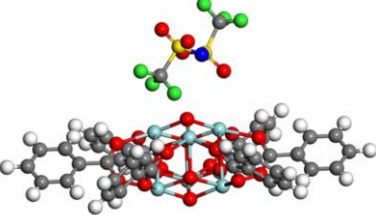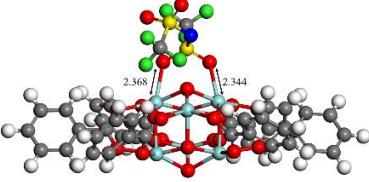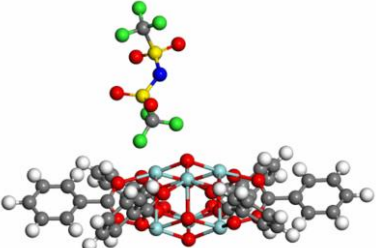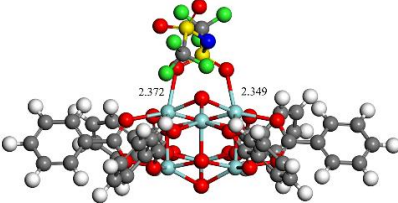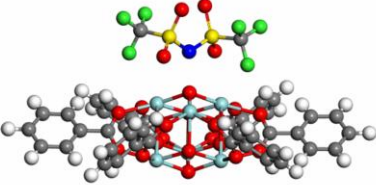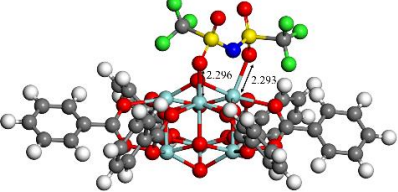
Fig. 2.5 | DFT calculations. a, b, Electrostatic potential distribution of truncated UMCM-309a and a TFSI– anion; **c,** initial and optimized adsorption configurations of a TFSI– anion on a truncated IMP (cyan: Zr, red: O, grey: C, white: H, blue: N, yellow: S, green: F).

Table 2.1 DFT calculations of TFSI$^-$ adsorption configurations at different initial positions on IMP clusters.

IMP cluster	TFSI$^-$
E = -96591.050eV	E = -49677.469 eV
C O Zr F N S H	

Initial position	Geometry optimization
E_{link1} = -146272.008 eV	E_{ads1} = -3.489 eV
E_{link2} = -146273.819 eV	E_{ads2} = -5.300 eV
E_{link3} = -146273.644 eV	E_{ads3} = -5.126 eV
E_{link4} = -146273.690 eV	E_{ads4} = -5.171 eV
E_{link5} = -146274.040 eV	E_{ads5} = -5.521 eV
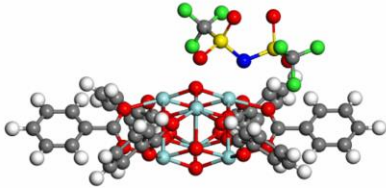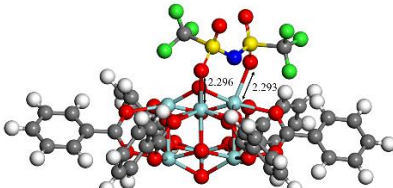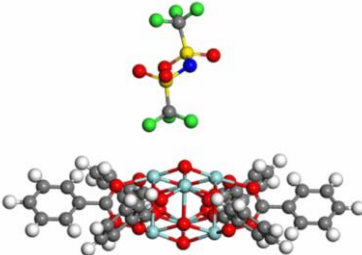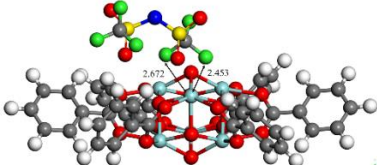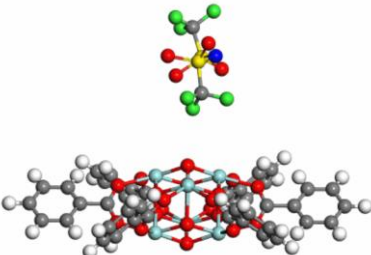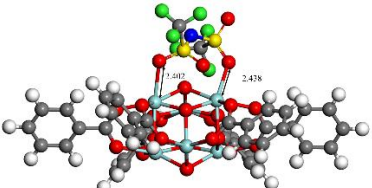
E_{link6} = -146274.054 eV	E_{ads6} = -5.535 eV
E_{link7} = -146272.037 eV	E_{ads7} = -3.518 eV
E_{link8} = -146273.986 eV	E_{ads8} = -5.467 eV

Table 2 show the electrostatic potential (EP) distribution of a truncated Zr_6 cluster and a $TFSI^-$ anion obtained by density functional theory (DFT). The most negative EP region of the $TFSI^-$ anion is localized around the oxygen atoms of $(CF_3SO_2)_2N^-$, whereas the space close to the Zr^{4+} centers provides the most positive EP for accommodating $TFSI^-$ anions (**Figs. 3.5a-b**). The subsequent geometry optimization suggests that the most favorable binding structure is where the two oxygen atoms from $(CF_3SO_2)_2N^-$ bind to the nearest adjacent Zr atoms in planar direction (**Fig. 2.5c**).

Table 2.2 Summary of mass and molar concentration of Zr/Li by ICP-AES analysis of LFS-laden IMP.

Element	Mass concentration (mg kg^{-1})	Molar concentration (mmol kg^{-1})
Zr	115.4899	1.2691
Li	43.6985	6.2426

The relative molarity between the LFS (1 M) before and after adsorption by 1% IMP was determined by ICP-AES analysis. Assuming the volume of IMP is negligible compared to the electrolyte volume, we vacuum dried the sample and weighed the mass of solvent loss from the electrolyte in order to deduct the excess part of LFS which is not interact with IMP (48%). The DOL/DME electrolyte shows a comparable mass density of 1.13 g cm^{-3}. The estimated molar mass of IMP is 1518 g mol^{-1}, given a formula of $Zr_6O_6(BTB)_2$, and LiTFSI is 287 g mol^{-1}. The molarity ratio from the ICP between Li:Zr $\approx$ 5 and Li: IMP (Zr_6) $\approx$ 30. Assume there is 100 g of the mixture sample in total, then the amount of the solvent loss is 48 g, and the remaining part is LiTFSI and IMP mixture, which is 52 g in total. Assume the mass of the LiTFSI, denoted as m_{LiTFSI}, is x g. And the mass of the IMP, denoted as m_{IMP}, is (52-x) g. Therefore, the molar concentration ratio between IMPs and absorbed LiTFSI can be calculated by the following equations:

$$M_{LiTFSI} : M_{IMP} = n_{LiTFSI} : n_{IMP} \approx 30$$

$$\frac{x \ g}{287 \ g \ mol^{-1}} : \frac{(52-x) \ g}{1518 \ g \ mol^{-1}} \approx 30$$

$$m_{LiTFSI} = 44.22\ g$$

$$n_{LiTFSI} = \frac{44.22\ g}{287\ g\ mol^{-1}} = 0.153\ g\ mol^{-1}$$

$$V_{solvent} = \frac{48\ g}{1.13\ g\ mol\ cm^{-3}} = 42.48\ cm^3 = 0.04248\ l$$

$$M_{LiTFSI} = \frac{0.153\ g\ mol^{-1}}{0.04248\ l} = 3.6\ M$$

Where, M_{LiTFSI} and M_{IMP} is the molarity of LiTFSI and IMP in the mixture, n_{LiTFSI} and n_{IMP} is the number of moles of LiTFSI and IMP in the mixture, $V_{solvent}$ is the volume of DOL/DME.
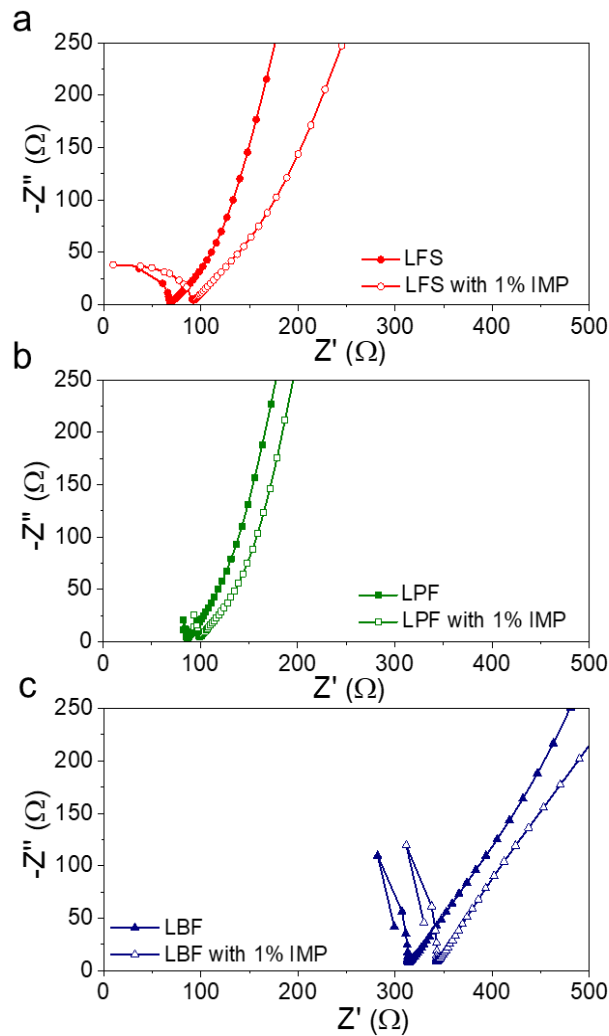
Fig. 2.6 | Nyquist plots for measuring ionic conductivity of electrolytes: **a**, LFS and LFS with 1% IMPs; **b**, LPF and LPF with 1% IMPs; **c**, LBF and LBF with 1% IMP.

Note: the ionic resistance was estimated by the extrapolated interception of the Nyquist plots with real axis.

The ionic conductivity of electrolytes was measured in a home-made cell using identical Titanium electrodes. The ionic resistance was estimated from the Nyquist plots of electrochemical impedance spectroscopy (EIS) (**Fig. 2.6**). Given the ionic resistance, fixed cell parameters and conductivity of reference electrolyte (LFS, 10.9 mS cm^{-1}), a slightly decreased ionic conductivity of 8.9 mS cm^{-1} was obtained for the LFS with 1% IMP.
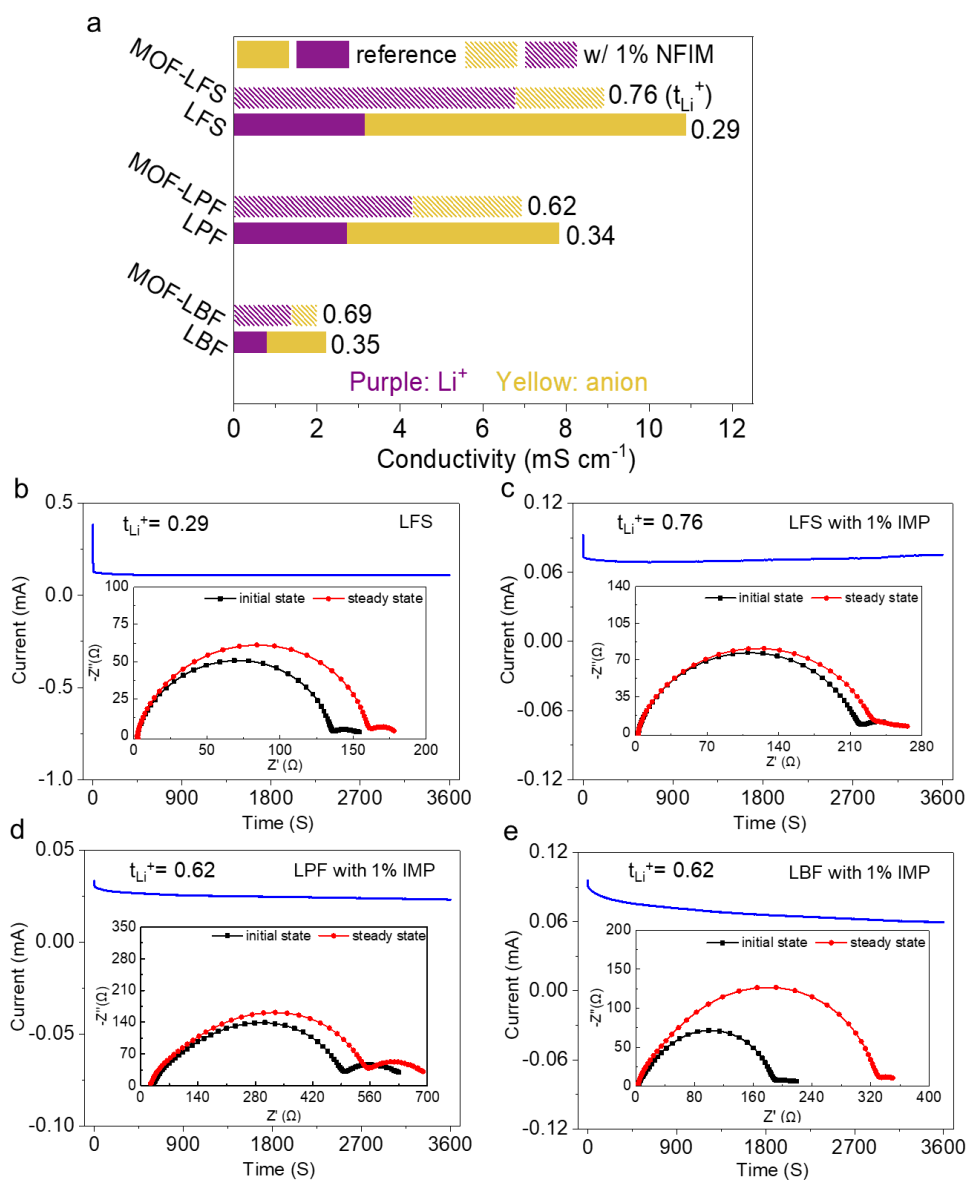
Fig. 2.7 | Comparison of t$_{Li}^+$ using different electrolytes with or without IMP. **a,** Conductivity of anions and lithium ions, and t_{Li}^+ in different electrolytes with and without IMP. Potentiostatic polarization of electrolytes in Li|Li cells (inset: Nyquist plots of initial and steady states). **b,** LFS; **c,** LFS with 1% IMPs; **d,** LPF with 1% IMPs; (e) LBF with 1% IMPs.

To partition the conductivity contributions from Li^+ ion and anions, t_{Li^+} was measured in symmetric Lithium cell (Li|Li) configuration using a classic potentiostatic polarization method.[115] As shown in **Fig. 2.7a**, adding 1% IMP into LFS dramatically enhances the t_{Li^+} from 0.29 to 0.76, revealing that the additive selectively reduces the anion mobility and promotes the cation conduction. To exclude a pure "size-matching" effect between $TFSI^-$ (7.9 × 3.9 Å) and IMP (8.6 Å) that leads to the improved t_{Li^+}(**Figs. 3.7b-c**),[116] the adsorption effect of IMP towards electrolytes with smaller anions (PF_6^-: 5.1 Å[117], BF_4^-: 4.8 Å[118]) were also validated (**Figs. 3.7d-e**).[106] 1M Lithium hexafluorophosphate ($LiPF_6$) in ethylene carbonate and diethylene carbonate mixture (1:1 by volume) (abbreviated as LPF) and 1M Lithium tetrafluoroborate ($LiBF_4$) in propylene carbonate (abbreviated as LBF) were compared with respective electrolytes with 1% IMP. As summarized in **Fig. 2.7a**, the additive of 1% IMP slightly compromises the ionic conductivities of bare electrolytes by average of 9%, while substantially improving their t_{Li^+} by average of 109%, thus categorizing the IMP as a novel and unique two-dimensional additive.
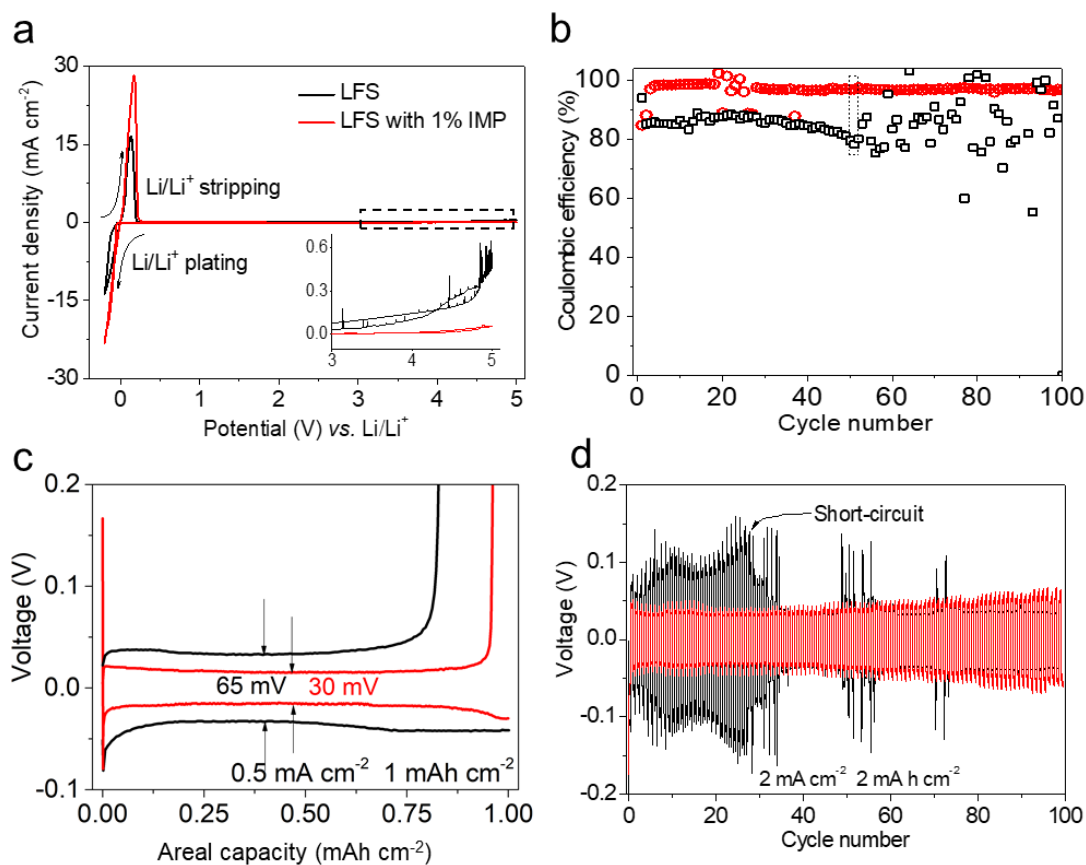
Fig. 2.8 | a, CV curves of SS|Li cells between –0.2 to 5 V (*vs.* Li/Li$^+$). **b**, Coulombic efficiency of Cu|Li cells at plating areal capacity of 1 mAh cm^{-2} and **c**, is the voltage profiles at 50th cycle. **d**, Galvanostatic cycling of Li|Li cells at areal capacity of 2 mAh cm^{-2} and current density of 2 mA cm^{-2}.

The electrochemical stability of LFS with 1% IMP was evaluated using stainless steel plate (SS) as working electrode and Li metal as counter/reference electrodes (SS|Li). As shown in **Fig. 2.8a**, the cyclic voltammetry (CV) curves were performed in a potential window between –0.2 and 5 V (*vs.* Li/Li$^+$), in which notable redox peaks near 0 V could be assigned to the Li/Li$^+$ stripping-plating processes on SS. Compared

with the reference cell, the cell with 1% IMP shows sharp redox peaks with approximately doubled peak current density, hinting at a significantly improved Li^+ ionic mobility and remarkable electrochemical stability of IMP against Li^+.[119] The Coulombic efficiency of Li/Li^+ stripping-plating, defined as the ratio of stripped to fixed plated amount of Li (1 mAh cm^{-2}), was further evaluated on a Cu substrate at a current density of 0.5 mA cm^{-2} (denoted as Cu|Li cell). As shown in **Fig. 2.8b**, the cell with 1% IMP exhibits exceptional cyclic stability with an average Coulombic efficiency of 96% for 100 cycles and a typical voltage hysteresis of 30 mV (50th cycle). In contrast, the reference cell shows a deteriorated Coulombic efficiency of 78% and a voltage hysteresis of 65 mV at the 50th cycle (**Fig. 2.8c**), which are followed by disordered profiles indicative of dendritic Li proliferation. The galvanostatic cycling of Li|Li cells (2 mA cm^{-2}) in **Fig. 2.8d** is consistent with the results from the Cu|Li cells. At the initial stage, the reference cell suffers from a higher voltage polarization (180 mV) than the cell using 1% IMP (75 mV) at the 15th cycle. Afterwards the reference cell exhibits huge voltage fluctuation and abrupt voltage drop (cell failure) after 25 cycles, whereas the cell using IMP maintains stable voltage (75~100 mV) for 100 cycles.
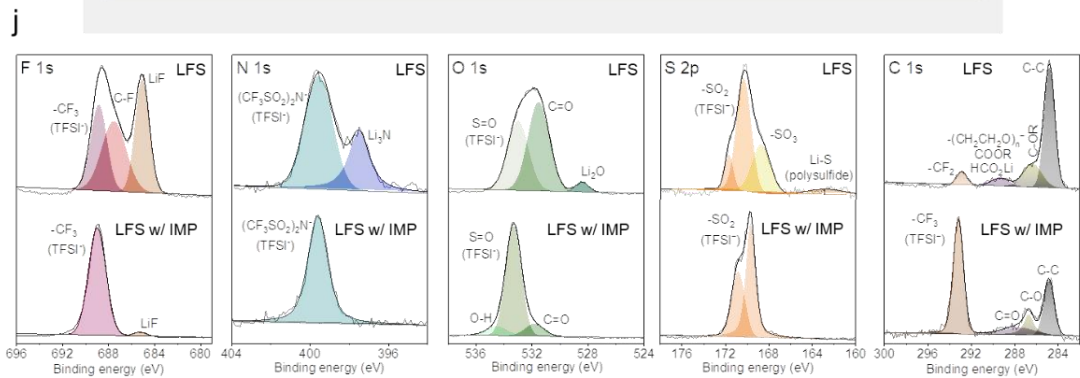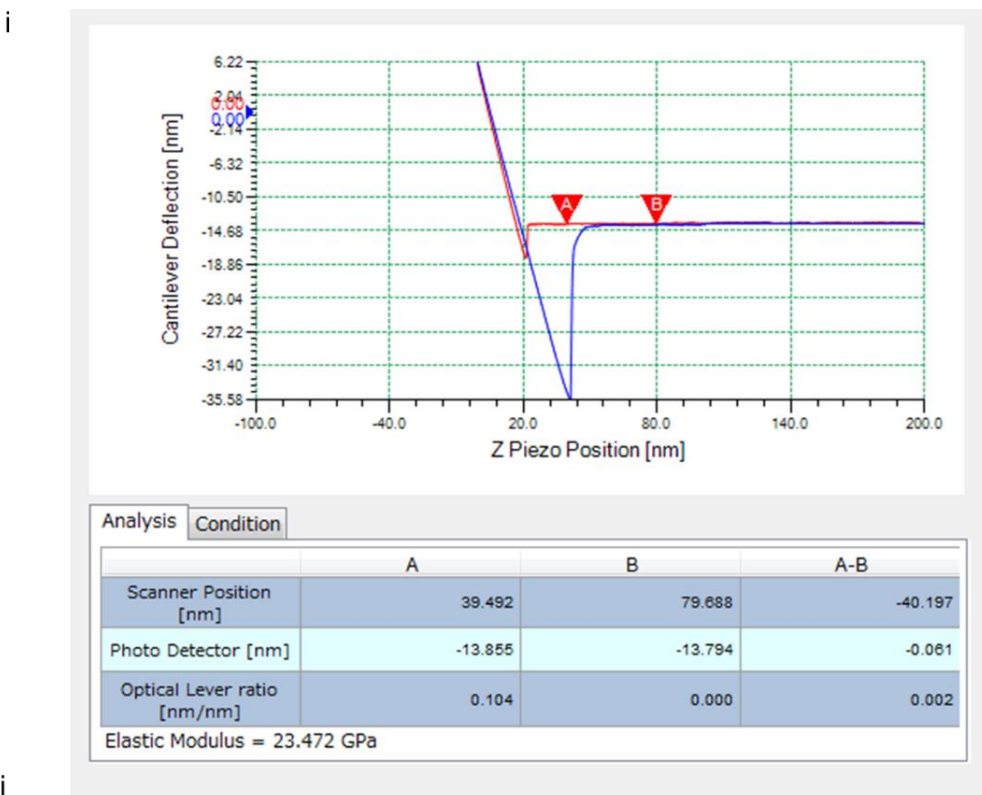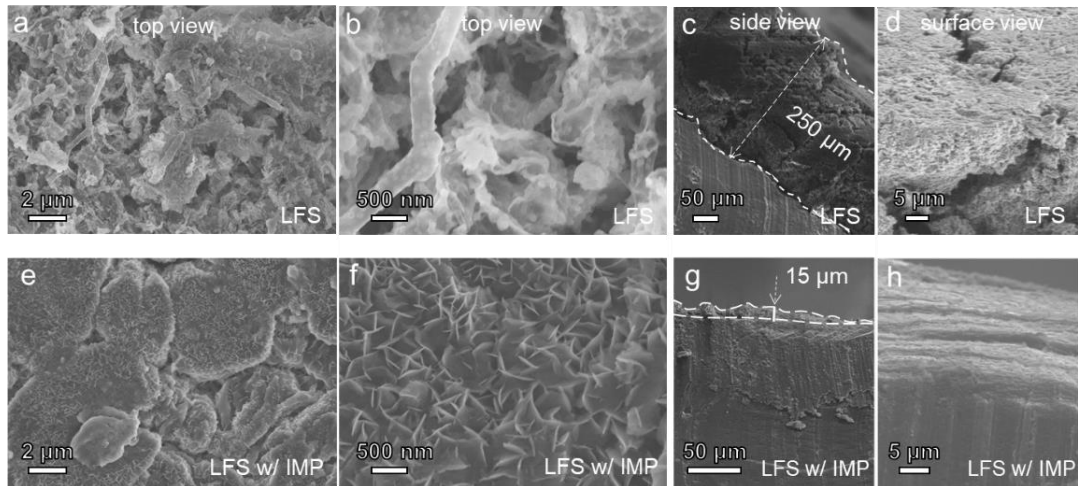
Fig. 2.9 | The formation of FAIM layer on lithium electrodes. Post-cycle evaluations of

Li harvested from Li|Li cells (25 cycles): SEM images Li cycled in **a-d** LFS and **e-h**

LFS with 1% IMPs; **i**, Measurement of the elastic modulus of FAIM layer after cycling by atomic force microscopy. **j**, F 1s, N 1s, O 1s, S 2p, C 1s spectra from XPS analysis of cycled Li.

Without IMP, as-formed interphase exhibits a porous and filamentous structure with a thickness of ~250 μm (**Figs. 3.9a-d**). With IMP, as-formed interphase is much denser (~15 μm in thickness) and incorporated with IMP (**Figs. 3.9e-h**). As suggested by atomic force microscopy (**Fig. 2.9i**), the FAIM layer on the LMA exhibits Young's modulus (23.47 GPa), much higher than the routine SEI (0.63 GPa), and far more than 6.0 GPa, which was predicted by Newman et al. for Li dendrite suppression). Consistently, the cell with IMP maintains a lower and stable overpotential (45-55 mV) for over 100 cycles, whereas the cell without IMP displays a higher and fluctuated overpotential (e.g., 55~120 mV) and a short-circuit failure after 25 cycles (Figure 3e). Furthermore, **Fig. 2.9j** shows the x-ray photoelectron spectroscopy (XPS) of the Li electrodes after 25 cycles.   The deconvoluated peaks at the binding energy of 688.9 eV (F 1s spectra), 399.6 eV (N 1s), 533.0 eV (O 1s), 171.7/170.3 eV (S 2p) and 293.2 eV (C 1s) are ascribable to $(CF_3SO_2)_2N^-$ (TFSI$^-$) in ionic status.   Several concurrent signals at 687.5/685.1 eV (F 1s), 397.5 eV (N 1s), 531.5/528.4 eV (O 1s), 168.7/163.0 eV (S 2p), and 292.9 eV (C 1s) could be assigned to C–F/LiF, Li_3N, C=O/Li_2O, –SO_3/Li–S, and –CF_2, respectively, all of which are derived from the decomposition of TFSI$^-$.[120, 121] These studies suggest that IMP assists to stable electrolyte-electrode

interface and electrolyte, which is consistent with the reduced cell ohmic and interfacial resistance.
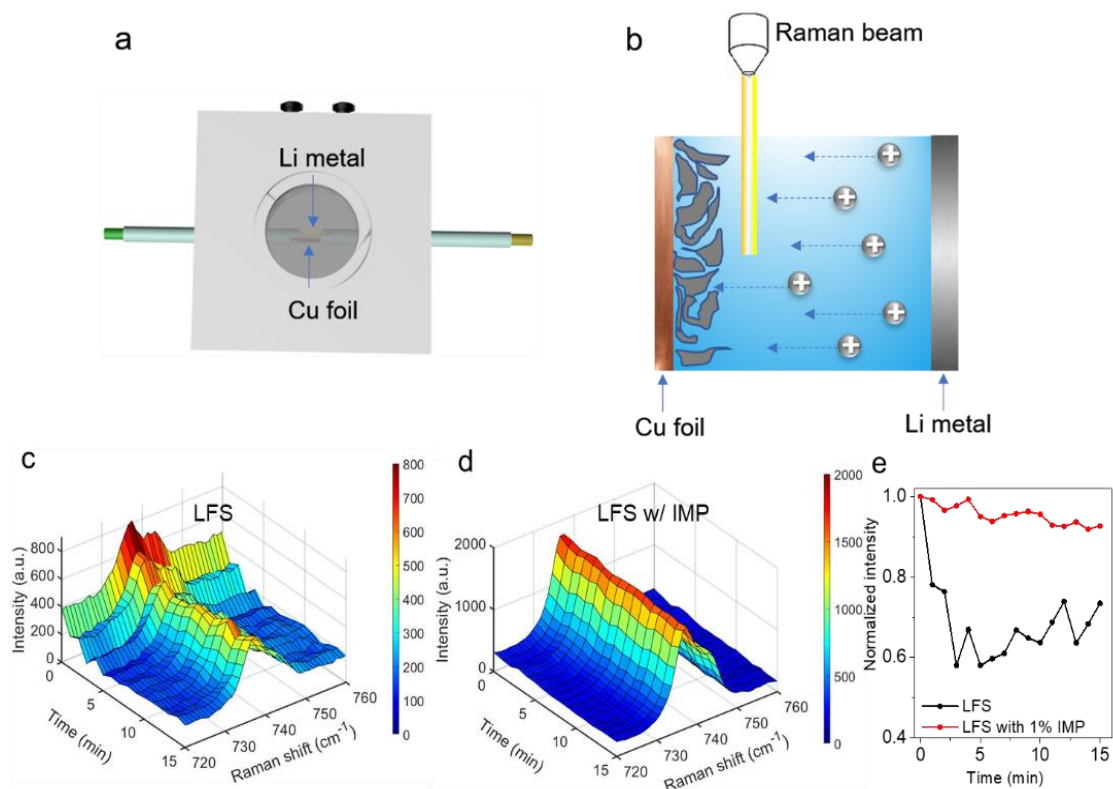
Fig. 2.10 | *In situ* Raman test collected from the Cu surfaces of Cu|Li cells. a, Apparatus setup of in situ Raman measurement, a custom-made Cu|Li cell with quartz window; **b,** Illustration of Raman beam in the cell. *In situ* Raman spectra of **c,** LFS and **d,** LFS with 1% IMP, and **e,** corresponding normalized intensity of TFSI$^-$ signal during time frame.

To explore the connections between these post-cycle evaluations and the excellent

electrochemical performances, *in situ* Raman spectroscopy was applied on the Cu surface of the Cu|Li cell to investigate the dynamics of TFSI$^-$ ion flux during the Li/Li$^+$ plating process on Cu (3 mA cm^{-2}). The custom-made cell and apparatus setup were illustrated in **Figs. 3.10a-b**, and the signals of TFSI$^-$ (S–N–S vibration) were collected every 1 minute and plotted in chronological order. As shown in **Fig. 2.10c**, the cell with the reference electrolyte exhibits an immediate sharp decline of TFSI$^-$ intensity upon applying the current, followed by a dramatic reduction of 58% (relative to the initial intensity) during a time interval of 15 minutes (**Fig. 2.10d**).[122] Such change unambiguously originates from the concentration polarization that instantly depletes local electrolyte at high current densities. In contrast, the cell with 1% IMPs (**Fig. 2.10e**) robustly maintains the characteristic intensity with a maximum reduction of 92% throughout the test, denoting that the IMP effectively buffers the concentration change and circumvents electrolyte depletion during Li/Li$^+$ plating, which would otherwise lead to a deteriorating electrode-electrolyte interface and the proliferation of dendritic Li.[123] Hence, the bound anions by IMP establish a negatively-charged anti-polarization region preventing the draining of LiTFSI especially at heavy load currents, thereby contributing to the affinitive and conductive interfaces.
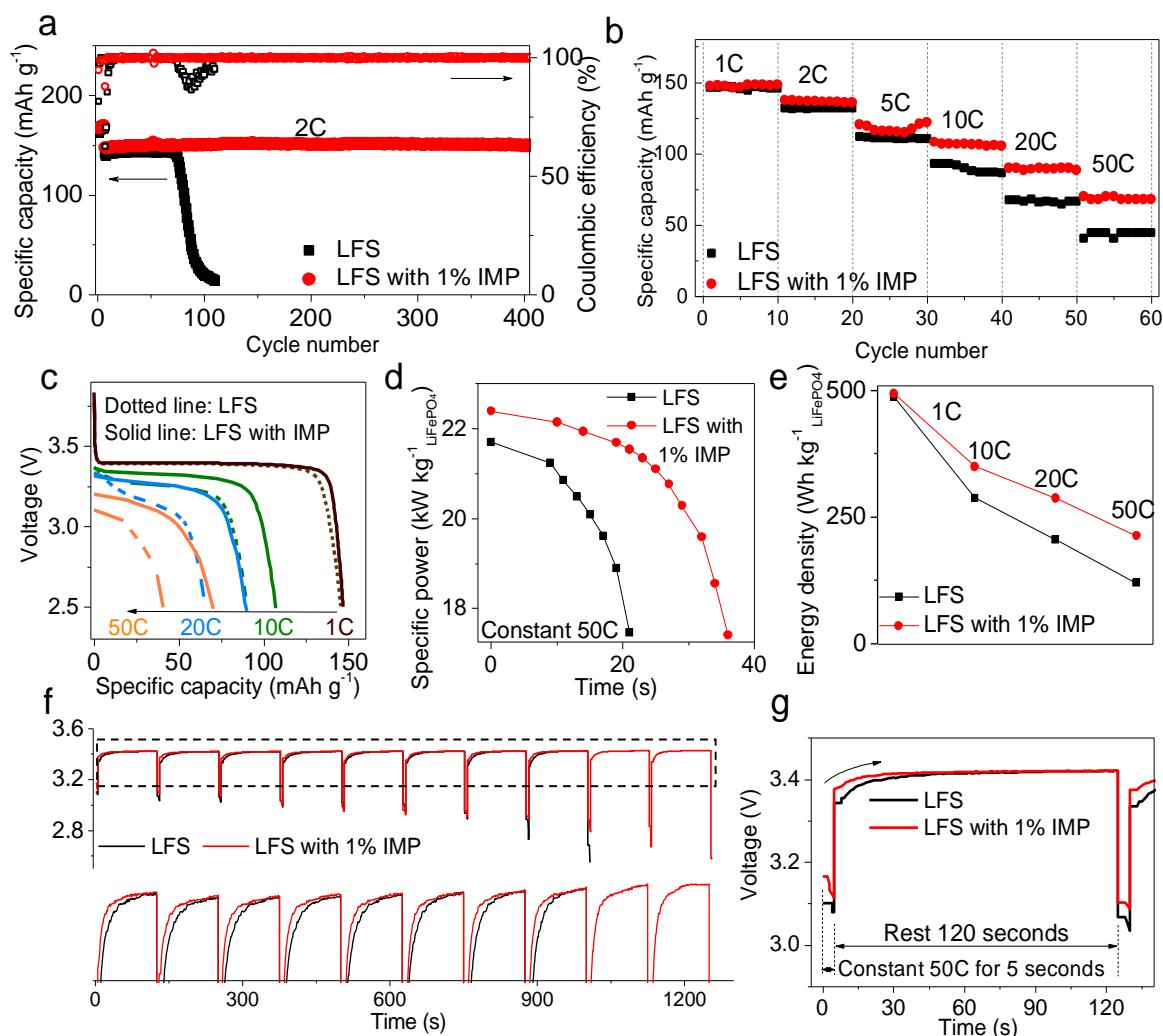
Fig. 2.11 | High-rate performance of LiFePO₄|Li protype cells with and without IMP. **a,** Long-cycle stability of LiFePO₄|Li cells under 2C (initial 5 cycles at 0.5C). **b,** Rate tests of LiFePO₄|Li cells from 1C to 50C. **c,** Discharge profiles of LiFePO4|Li cells at 1/10/20/50C. **d,** Power outputs of LiFePO**4**|Li cells at constant 50C. **e,** Energy outputs of LiFePO4|Li cells at 1/10/20/50C. **f,** Plots of voltage vs. time of LiFePO4|Li cells with and without IMP under pulse discharged at 50C for 5 s followed by a rest of 120 s repeatedly. The curve underneath is the magnified portion of the plot above. **g,**1st pulse discharge profile of LiFePO₄|Li cells at 50C (5 s) followed by rest period of 120 s.

The ability to mitigate concentration polarization, reduce overpotential, and stabilize electrode interface enables the fabrication of batteries with improved high-rate performance. As demonstration, prototype cells were assembled without and with IMP, which are denoted as reference cell (without IMP) and modulated cell (with IMP), respectively. **Fig. 2.11a** shows the galvanostatic cycling of $LiFePO_4$|Li cells consisting of a $LiFePO_4$ cathode (1 mAh cm^{-2}) and Li anode (10 mAh cm^{-2}), where the reference cell and modulated cell cycled at 2 C retain a capacity of 142 mAh g^{-1} for 400 and 70 cycles, respectively. The modulated cell exhibits a higher capacity (**Fig. 2.11c**), longer discharging time (**Fig. 2.11d**), and greater energy output (**Fig. 2.11e**), particularly at high C rates. For example, the modulated and reference cells provide an initial power of 22.4 and 21.7 kW kg^{-1} at 50 C, delivering power for 36 and 20 s before reaching the cutoff voltage, respectively. In this process, the modulated cell provides a total energy output of 213 Wh kg^{-1}, which is 78% higher than that of the reference cell (120 Wh kg^{-1}) calculated based on the mass of $LiFePO_4$.

As shown in **Fig. 2.11e**, compared with the reference cell that delivers energy output of 489, 289, 206, and 120 wh kg^{-1}, the modulated cell provides a higher output of 494, 350, 288, and 213 wh kg^{-1} at the C-rate of 1, 10, 20, and 50, respectively, corresponding to 1 %, 21 %, 40 %, and 78 % of output enhancement. The improved performance is attributable to IMP, which mitigates the polarization particularly during high-rate operation. For confirmation, the cells were discharged at 50 C for 5 s followed

by a rest of 120 s repeatedly, which allows the as-developed polarization to dissipate during the rest. Figure 4f shows the voltage-time profile for the 1st discharge-rest circle. The high-rate discharge generates a concentration polarization, which is dissipated during the rest period, which is manifested by the increasing cell voltage during the rest period.   The modulated cell shows a recovery time (time to reach 0.99 equilibrium cell voltage) that is ~ 50% shorter than the reference cell (**Figs. 2.11f-g**).   This observation strongly suggests that IMP also mitigates concentration polarization through facilitating dissipation of the polarization.   Aided by the rest procedure that dissipates the concentration polarization, the reference cell delivers a higher enhancement of energy output (115%, 120 to 258 wh kg^{-1}) than the modulated cell (47%, 213 to 313 wh kg^{-1}), indicating that the dissipation was more beneficial for the reference cell due to its severer concentration polarization.
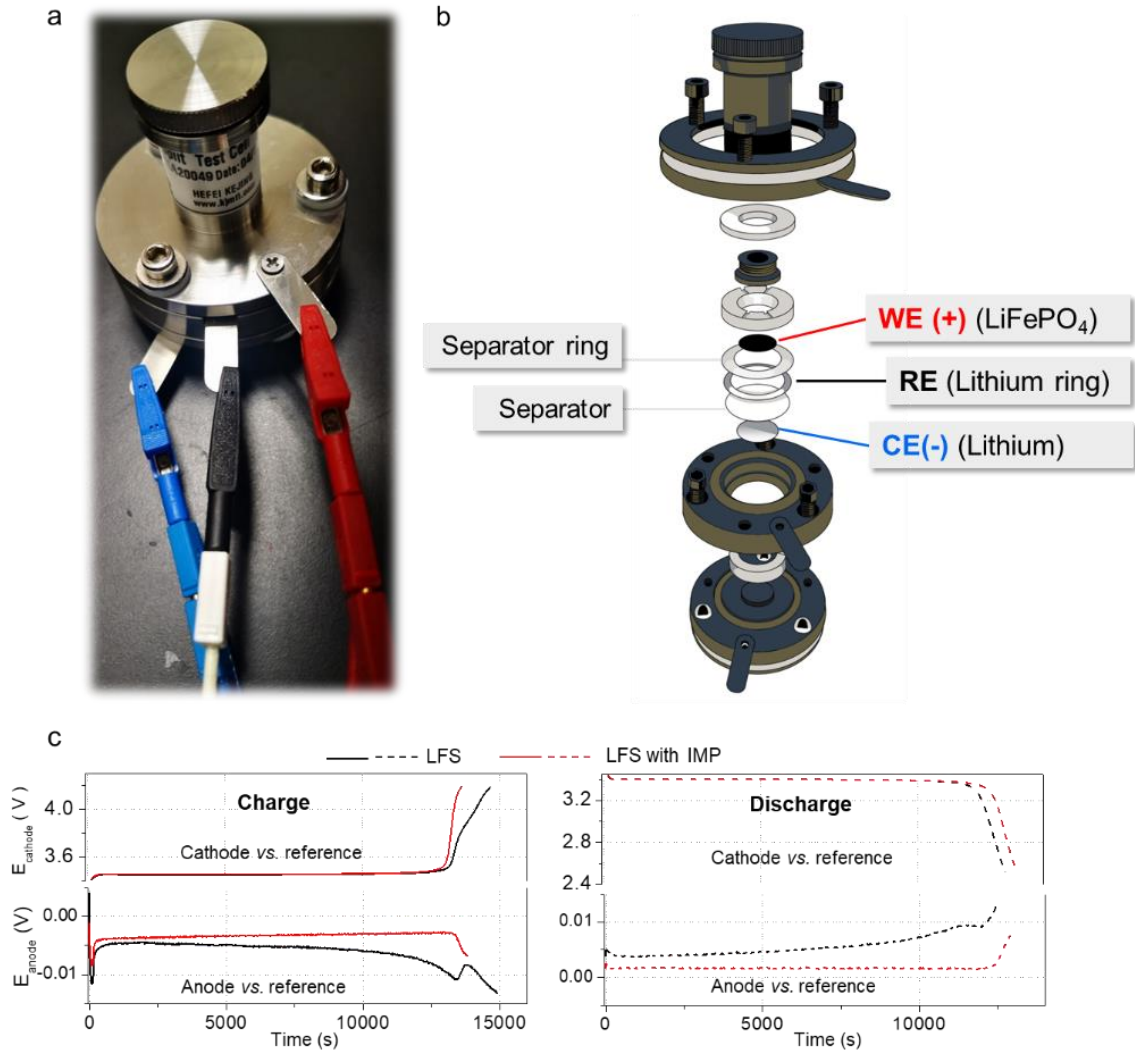
Fig. 2.12 | Three-electrode test. **a**, A photograph and **b**, an exploded schematic view of three-electrode flow cell setup. **c**, Charge and discharge curves of cathode and anode with respect to reference electrodes in three-electrode configuration (LiFePO4|Li|Li).

The polarization in the LiFePO4|Li cells was further investigated in three-electrode flow cells (LiFePO4|Li|Li, with a Li metal reference electrode) (**Figs.2.12a-b**) and COMSOL Multiphysics simulation. Anode and cathode voltage in the flow cells were monitored during cycling at 0.3C (**Figs. 2.12c**). The cathodes in both cells display a similar voltage plateaus of 3.45 V during charging and discharging. The anode in the

modulated cell shows a stable overpotential (2-3 mV) during charging and discharging, while the anode in the reference cell shows increasing overpotential (5-11 mV during charging and 4-10 mV during discharging), indicating IMP mainly depresses anode polarization at low C-rate. Note a sudden decrease of the anode overpotential near the cutoff voltage is also observed in the reference cell, which is attributable to destabilization of electrode interface or electrolyte. In accordance with the Bulter-Volmer equation, the kinetic current (I) for parasitic reactions of an electrode is exponentially proportional to the overpotential (v) ($I \propto eV$).   The use of IMP leads to dramatic 1 to 4 folds reduction of anode overpotential (2-3 vs. 4-11 mV), signifying 6 to 54 folds reduction of parasitic reactions with improved electrode interface and cycling lifespan.
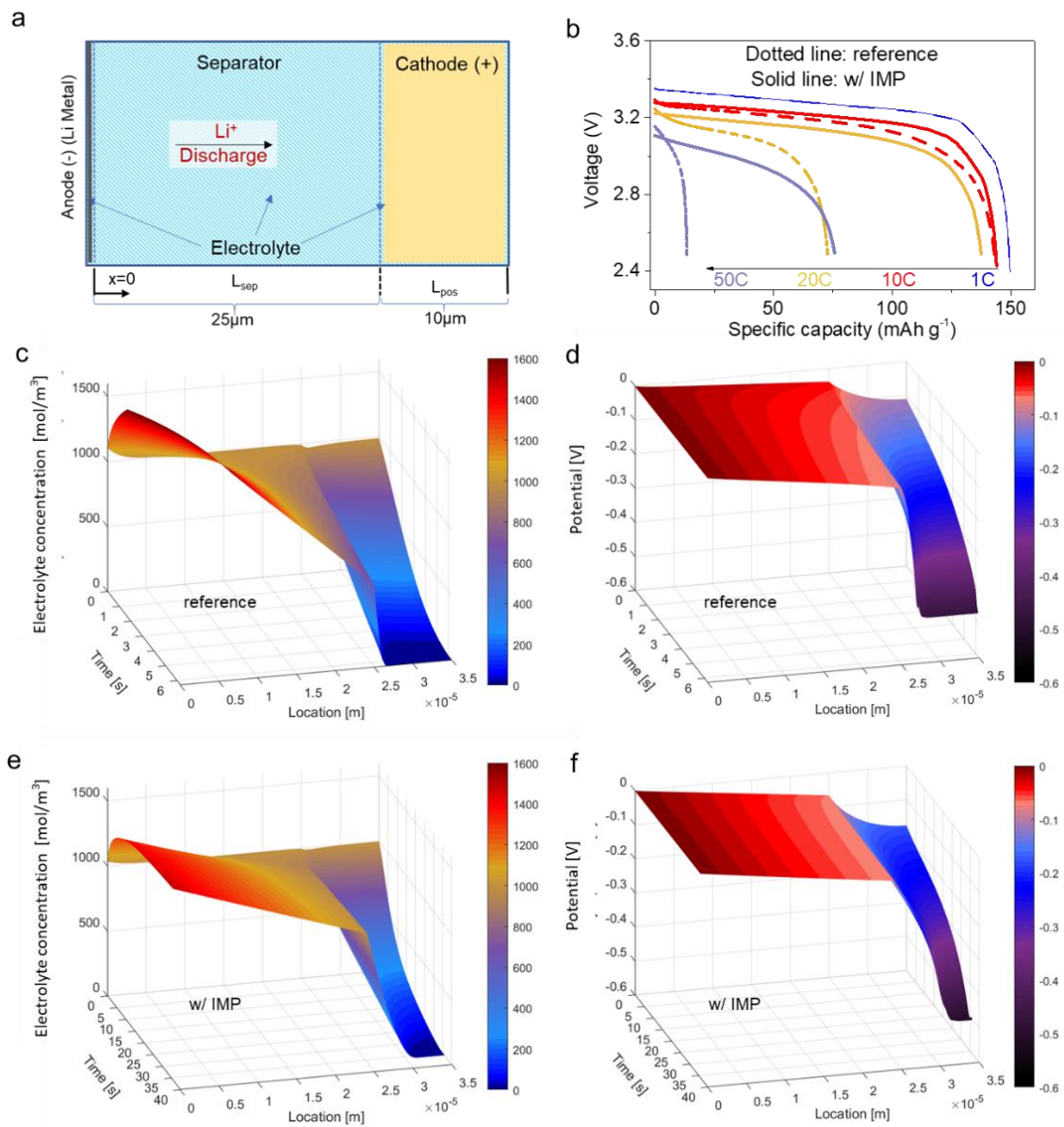
Fig. 2.13 | COMSOL simulation. a, Schematic of LiFePO4|Li cell model with 1-D coordination shown. **b,** Discharge profiles of simulated LiFePO4|Li cells as a function of C rates (1/10/20/50C). (**c, e**) Concentration profiles and (**d, f**) electrolyte potential drops simulated from constant 50C discharging modeled in LiFePO4|Li cells.

Table 2.3 Li-ion P2D model governing equations and boundary conditions. [124, 125]

Governing equations	Boundary conditions
Positive electrode, $i \in \{p, n\}$	
$\epsilon_i \dfrac{\partial c_e(x,t)}{\partial t} = \dfrac{\partial}{\partial x}[D_{\text{eff},i} \dfrac{\partial c_e(x,t)}{\partial x}] + a_i(1-t_+)j(x,t)$ (e1)	$-D_{\text{eff},i} \dfrac{\partial c_e(x,t)}{\partial x}\Big|_{x=0,\,L_s+L_p} = 0$ (b1) $c_e(x,t)\big|_{x=L_s^-} = c_e(x,t)\big|_{x=L_s^+}$ (b1')
$\dfrac{\partial c_{s,i}(x,r,t)}{\partial t} = D_{s,i}\dfrac{1}{r^2}\dfrac{\partial}{\partial r}\left(r^2\dfrac{\partial c_{s,i}(x,r,t)}{\partial r}\right)$ (e2)	$-D_{s,i}\dfrac{\partial c_{s,i}(x,r,t)}{\partial r}\Big|_{r=0} = 0$ (b2) $-D_{s,i}\dfrac{\partial c_{s,i}(x,r,t)}{\partial r}\Big|_{r=R_{s,i}} = j(x,t)$ (b2')
$a_i Fj(x,t) = -\dfrac{\partial}{\partial x}[\boldsymbol{\kappa}_{\text{eff},i}\dfrac{\partial \Phi_e(x,t)}{\partial x}] + \dfrac{\partial}{\partial x}[\boldsymbol{\kappa}_{\text{eff},i}\Upsilon T(x,t)\dfrac{\partial \ln c_e(x,t)}{\partial x}]$ (e3) $\left(\Upsilon := \dfrac{2(1-t_+)R}{F}\right)$ $\dfrac{\partial}{\partial x}[\sigma_{\text{eff},i}\dfrac{\partial \Phi_s(x,t)}{\partial x}] = a_i Fj(x,t)$ (e4) $j(x,t) = 2k_{\text{eff},i}\sqrt{c_e(x,t)(c_{s,i}^{\max}-c_s^*(x,t))c_s^*(x,t)}\ \sinh[\dfrac{0.5R}{FT(x,t)}\eta_i(x,t)]$ (e5) $\eta_i(x,t) = \Phi_s(x,t) - \Phi_e(x,t) - \mathbf{U}_i$ (e6)	$-\boldsymbol{\kappa}_{\text{eff},i}\dfrac{\partial \Phi_e(x,t)}{\partial x}\Big|_{x=0,\,L_s+L_p} = 0$ (b3) $\Phi_e(x,t)\big|_{x=L_s^-} = \Phi_e(x,t)\big|_{x=L_s^+}$ (b3') $-\sigma_{\text{eff},i}\dfrac{\partial \Phi_s(x,t)}{\partial x}\Big|_{x=L_s+L_p} = I_{app}(t)$ (b4) $-\sigma_{\text{eff},i}\dfrac{\partial \Phi_s(x,t)}{\partial x}\Big|_{x=L_s} = 0$ (b4') $\Phi_s(x,t)\big|_{x=0} = 0$ (b4")
Separator, $i = s$	

$$\epsilon_i \frac{\partial c_e(x,t)}{\partial t} = \frac{\partial}{\partial x}[D_{\mathrm{eff},i} \frac{\partial c_e(x,t)}{\partial x}] \quad (e1')$$

$$0 = -\frac{\partial}{\partial x}[\kappa_{\mathrm{eff},i} \frac{\partial \Phi_e(x,t)}{\partial x}] + \frac{\partial}{\partial x}[\kappa_{\mathrm{eff},i} T(x,t) \Upsilon \frac{\partial \ln c_e(x,t)}{\partial x}] \quad (e3')$$

$$-D_{\mathrm{eff},s} \frac{\partial c_e(x,t)}{\partial x}\Big|_{x=L_s^-} = -D_{\mathrm{eff},p} \frac{\partial c_e(x,t)}{\partial x}\Big|_{x=L_s^+} \quad (b1'')$$

$$-\kappa_{\mathrm{eff},s} \frac{\partial \Phi_e(x,t)}{\partial x}\Big|_{x=L_p^-} = -\kappa_{\mathrm{eff},p} \frac{\partial \Phi_e(x,t)}{\partial x}\Big|_{x=L_p^+} \quad (b3'')$$

Table 2.4 Algorithm parameter list of the COMSOL simulations for LiFePO4|Li.

Code	Value [Unit]	Description
i_1C	3 [A m^{-2}]	1C discharge current
t_plus	0.29/0.76	Li-ion transference number (control/experiment)
sigma	0.42/0.22 [S m^{-1}]	Ionic conductivity of the electrolyte (control/experiment)
cl_0	1000 [mol m^{-3}]	Initial electrolyte salt concentration
c_ref	1000 [mol m^{-3}]	Reference electrolyte salt concentration of ionic conductivity interpolation
L_sep	25×e^{-6} [m]	Length of the separator
L_pos	10×e^{-6} [m]	Length of the positive electrode
T	298 [K]	Temperature
rp_pos	8×e^{-6} [m]	Particle radius positive electrode
epsl_pos	0.3	Electrolyte phase volume fraction of the positive electrode
epss_filler_pos	0.14	Conductive filler phase volume fraction of the positive electrode
epss_pos	0.56	Electrode phase volume fraction of the positive electrode
cs0_pos	1000 [mol m^{-3}]	Initial concentration of the positive active electrode material
k_pos	4.8×e^{-10} [m s^{-1}]	Reaction rate coefficient of the positive electrode
brugg	3.3	Bruggeman coefficient

A 1-D model on the basis of the pseudo two-dimensional (P2D) model is implemented to simulate the galvanostatic charge of the Li|electrolyte| LiFePO$_4$ cell by using COMSOL Multiphysics$^®$. The lithium-ion battery model generally consists of three components of the battery: positive electrode (cathode), separator, negative electrode (anode), which are denoted respectively by the indexes p, s, and n. It should be noted that lithium metal is used as the anode (and could be treated as a 2D electrode surface, thus allowing the anode part to be neglected in the simulation), while the cathode here is a porous electrode with coexisting solid and liquid phases. In this model, we considered an isothermal scenario without discussing energy balance. And the governing equations and boundary conditions of the Li-ion P2D model are summarized in **Table 2.3**.

The COMSOL simulation was conducted on conceptual LiFePO$_4$|Li cells on the basis of the prototype cells,[105] which comprise a planar anode (Li) at 0 μm, a separator between 0 to 25 μm, a cathode (LiFePO$_4$) between 25 to 35 μm, and electrolyte with a $t_{Li}{}^+$ of 0.76 and 0.29 for the modulated and reference cell, respectively (**Fig. 2.12a**). The simulated discharge profiles are similar to the experimental ones (**Fig. 2.12b**), where the modulated cell show increasing improvements with increasing C-rate from 1, 10, 20 to 50. With a C-rate of 50, the modulated cell delivers a discharge capacity of 76 mAh g^{-1} for a duration of 36 s, which outperforms the reference cell (13 mAh g^{-1} for 6 s). **Figs. 2.12c-f** further show the concentration and overpotential profiles of the electrolyte at 50C. The electrolyte concentration rapidly changes (1.0 M to 1.5 M and 0 M at anode and cathode ends, respectively) in the reference cell, resulting in a reversal

74

potential of – 0.5 V in 6 s (**Figs. 2.12c-d**). The modulated cell shows a slower

polarization process (1.0 M to 1.3 and 0 M at anode and cathode ends, respectively),

resulting in a reversal potential of – 0.5 V in 36 s (**Figs. 2.12e-f**). Hence the earlier

electrolyte exhaustion at cathode end of reference cell leads to a huge overpotential that

limits its discharge duration and attainable capacity.
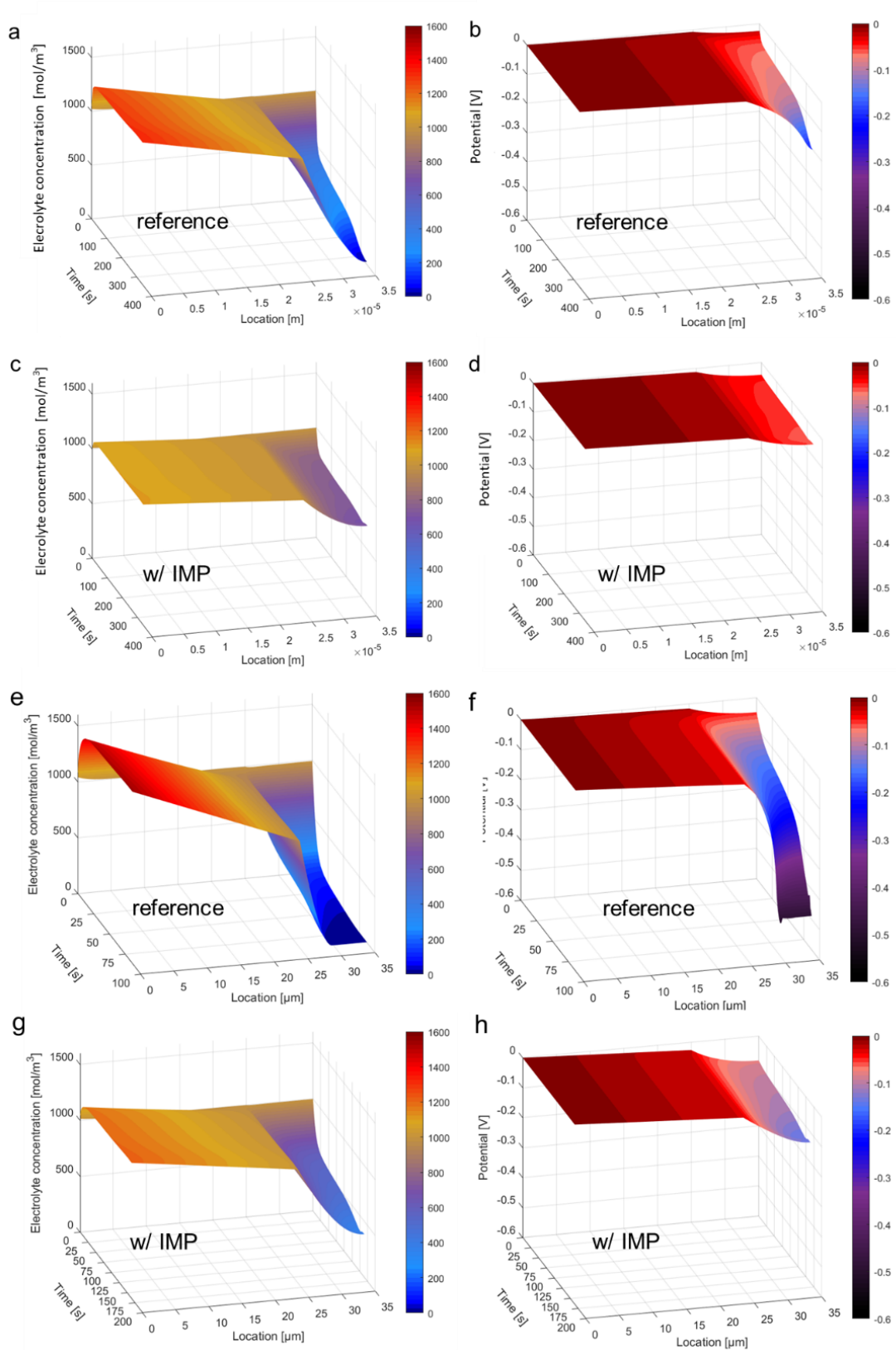
Fig. 2.14 | (a, c) Concentration profiles and **(b, d)** electrolyte potential drops simulated

from constant 10C discharging modeled LiFePO₄|Li cells. Note: (a-b) and (c-d) depict

the cells using electrolyte parameters from LFS and LFS with 1% IMP, respectively. (**e,**

g) Concentration profiles and (**f, h**) electrolyte potential drops simulated from constant

20C discharging modeled LiFePO$_4$|Li cells.

With a C-rate of 10 (**Figs. 2.14a-d**), though no electrolyte exhaustion occurs for

both cells, the modulated cell consistently shows mitigation of polarization. With a C-

rate of 20 (**Figs. 2.14e-h**), the reference cell develops analogous concentration gradient

and reversal potential to the results at 50C in 100 s; whereas the modulated cell exhibits

notably mitigated polarization (1.0 M to 1.22 M and 0.39 M at anode and cathode ends,

respectively) in 166 s, corresponding to a reversal potential of -0.13 V. Hence the

modulated cell avoids the complete electrolyte depletion. Therefore, the modulated cell

suppresses the concentration polarization that otherwise could be rate-limiting when

the cell is operated at higher C-rate.
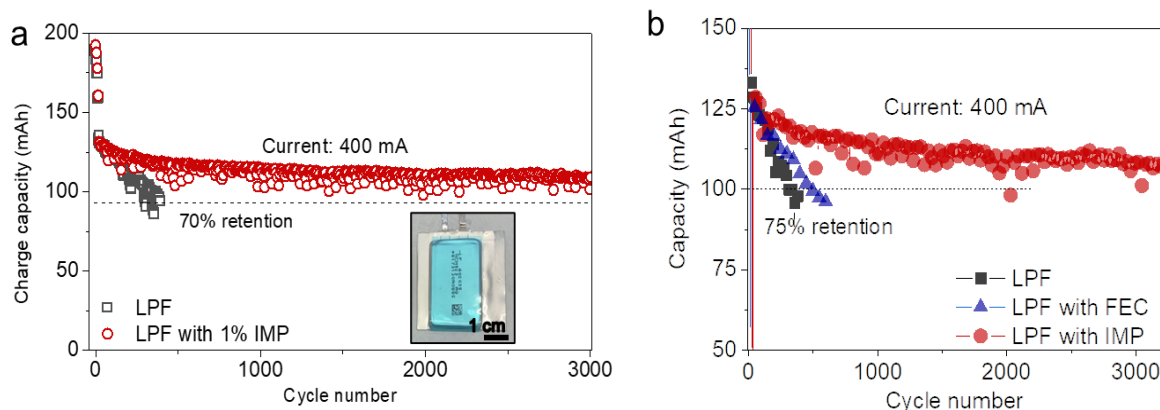
Fig. 2.15 | Pouch cells performance with IMP. a, Long-term cycling of commercial pouch cells (LiNi0.5Co0.3Mn0.2O2|graphite) at 400 mA (initial cycles at 20/30/50/100/200 mA) and voltage cutoff of 4.2 V. The inset shows a photograph of the commercial pouch cell (200 mAh). **b,** Cycle comparison of pouch cells with FEC and IMP.

Furthermore, the practicability of 2DM was demonstrated in pouch cells (200 mAh), which are composed of a $LiNi_{0.5}Co_{0.3}Mn_{0.2}O_2$ cathode, graphite anode, and LPF electrolyte ($LiPF_6$-based). **Fig. 2.15a** shows the stability tests at 400 mA (2C), where the reference cell benchmarks a 70% capacity retention at the 350th cycle. In contrast, the cell with 1% 2DM consistently maintains the capacity above the benchmark for over 2000 cycles. To assess the degree of improvement by 2DM, the cell added with commercial FEC (2% in weight) was also compared. As shown in **Fig. 2.15b**, the cell with FEC shows improvement over the reference by hitting the benchmark at 600th cycle, which is much less effective than adding 2DM. This performance comparison highlights that the novel class of two-dimensional additives potentially outperform conventional additives owing to the anti-polarization effect.
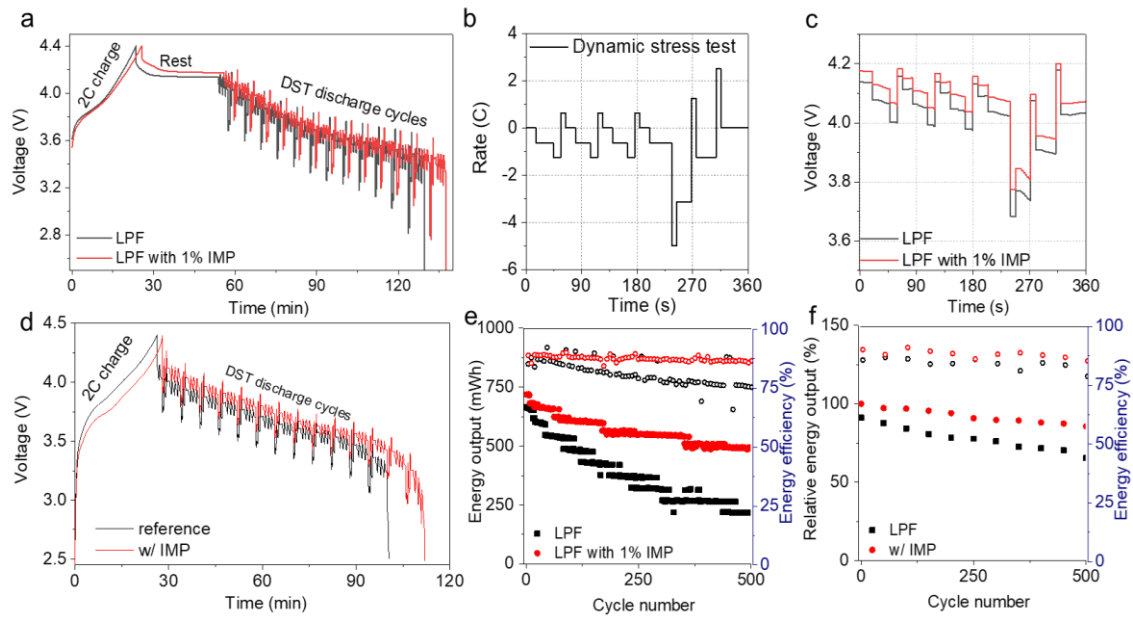
Fig. 2.16 | DST tests. a, Cycle protocol for DST scaled to rates (where 5C corresponds to maximum peak power). **b**, A representative DST cycle, and **c**, a full constant-charge/DST-discharge profile. **d**, Simulated decay profiles of charge capacity of pouch cells and **e**, A full simulated constant-charge/DST-discharge profile. **f**, Simulated LiNi0.5Co0.3Mn0.2O2|graphite cells discharged by DST.

The cells were also subjected to dynamic stress test (DST) to mimic dynamic operation of electric vehicles such as fast-charging, regenerative braking, and road driving. The conventional DST protocol was scaled to C-rates, where 5C discharge herein corresponds to the maximum peak power output. The cells were subjected to full-DST-cycles including: 1) charging at 2 C to a cutoff voltage of 4.4 V; 2) resting for 30 min; and 3) repeating DST followed the pattern illustrated in Figure 6b till reaching a cutoff voltage of 2.5 V. **Fig. 2.16a** shows the voltage profiles in response to the pattern

79

during the first cycle.　　The modulated cell shows a higher open-circuit voltage (4.14 V vs. 4.17 V) indicating an improved charge-accepting capability. The modulated cell also shows a higher discharging voltage (e.g., 3.68 V vs 3.77 V when discharged at 240 s) and charging voltage (e.g., 4.18 V vs. 4.20 V when charged at 312 s), consistent with a mitigated polarization **Fig. 2.16b** shows the voltage profiles of the 1st full-DST-cycle. The modulated cell delivers a higher cell voltage and energy output decreasing from 719 to 492 mWh after 500 full-DST cycles, which outperforms the reference cell (from 664 to 216 mWh), corresponding to an energy retention of 70% and 32%, respectively (**Fig. 2.16c**). The modulated and reference cell show a similar initial energy efficiency of 89%, and display to a respective decrease to 86% and 76% after 500 full-DST cycles. Note that the average C-rate in the DST is ~ 0.9 C; however, the cells subjected to the DST exhibit noticeably shortened cycling lifespan, in comparison with the tests under a constant-current rate of 2 C. The adoption of IMP, nevertheless, effectively mitigates the polarization and improves power response, energy output and cycle lifespan, which are essential for vehicle application.

Table 3.5 Algorithm parameters of the COMSOL simulations for $LiNi_{0.5}Co_{0.3}Mn_{0.2}O_2$|graphite cell DST.

Code	Value [Unit]	Description
epsl_pos	0.313	Electrolyte phase volume fraction positive electrode
brugl_pos	2.98	Bruggeman coefficient for tortuosity in positive electrode
epsl_neg	0.318	Electrolyte phase volume fraction negative electrode
epsl_sep	0.370	Electrolyte phase volume fraction separator
brugl_sep	3.15	Bruggeman coefficient for tortuosity in separator
k_neg	$2 \times e^{-11}$ [m s^{-1}]	Reaction rate coefficient negative electrode
k_pos	$5 \times e^{-10}$ [m s^{-1}]	Reaction rate coefficient positive electrode
cl_0	1000 [mol m^{-3}]	Initial electrolyte salt concentration
i_1C	29.93 [A]	1C discharge current
L_neg	$67 \times e^{-6}$[m]	Length of negative electrode
L_sep	[m]	Length of separator
L_pos	[m]	Length of positive electrode
T	298 [K]	Cell temperature
E_max	4.4 [V]	Maximum cell voltage
E_min	2.5 [V]	Minimum cell voltage
kappa_film	$5 \times e^{-6}$ [S m^{-1}]	SEI layer conductivity
M_sei	0.16 [kg mol^{-1}]	Molar mass of product of side reaction
rho_sei	$1.6 \times e^3$ [kg m^{-3}]	Density of product of side reaction
dfilm_0	1 [nm]	Initial SEI layer thickness
alpha	0.67	Ageing parameter
J	$8.4 \times e^{-4}$	Ageing parameter
f	$2.0 \times e^2$ [s^{-1}]	Ageing parameter
H	6.7	Ageing parameter
i1C_loc	0.96943[A m^{-2}]	Ageing parameter
no_cycles	1000	Number of cycles
t_plus	0.3(ref)/0.8(exp)	Lithium ion transference number
Eeq_SEI	0.1[V]	Equilibrium potential of SEI formation reaction

To further illustrate how a mitigated polarization may prolong the cycling lifespan of the batteries, a simulation was conducted on conceptual cells, which contain a graphite anode and a $LiNi_{0.5}Co_{0.3}Mn_{0.2}O_2$ cathode, and $LiPF_6$-based electrolytes with and without IMP. The simulation of cycling charge/discharge tests used Batteries and Fuel Cells Module on the basis of the pseudo two-dimensional model developed by Newman *et al.* [78]And the parameter inputs in the simulation were based on the experimental data, which were listed in Table 6.The static charge profile takes a 2C constant rate with a 4.4 V cutover voltage, while the dynamic discharge profile takes a (360-second) periodic loading with a 2.5 V cutoff voltage. The cells were subjected to the full-DST cycling protocol. The current for parasitic reactions in the electrode is assumed to be proportional to the overpotential of the electrodes. Due to the lack of reliable model for the parasite reactions in the cathode, overpotential-driven parasitic reactions in the anode were simulated, which was related to consumption of electrolyte and decay of the anode capacity. As shown in **Fig. 2.16e and Fig.3.16c** , the reference cell displays higher overpotential in a full cycle (**Fig. 2.16d**) and a faster decay of the energy output and lower energy efficiency, which is consistent with the experimental results. The simulated cell shows a decay rate of energy output less than the experimental cell, which could be ascribed to the parasite reactions in the cathode that are not included in the simulation.

2.4 Conclusions

In summary, we have developed a simple yet effective strategy to mitigate concentration polarization through a FAIM layer that is spontaneously formed on the

electrodes during normal operations of lithium-ion batteries. Such FAIM layers effectively modulate the transport of electrolyte, suppress concentration polarization and stabilize electrode-electrolyte interface, leading to improved power and energy output and prolonged cycle lifespan. In light of the rapid growth in electric vehicles, this IMP technique offers a low-cost yet effective approach towards high-performance batteries for dynamic and strenuous operations, such as fast-charging and instant braking charging.

Chapter 3. Uniform Surface Potential Distribution Induced by in-situ Cross-linked Artificial Solid Electrolyte Interface for Stable Lithium Metal Batteries

3.1 Introduction

As the most successfully commercialized energy storage system, lithium-ion batteries (LIBs) have numerous applications in the fields of portable devices and electric vehicles.[8, 12, 126] The state-of-the-art LIBs based on intercalated/de-intercalated graphite anode have fallen behind the expanding demands for high-energy energy storage systems due to their capacity limitations.[127] Alternatively, lithium metal is considered as the ideal anode material for next-generation lithium batteries owing to its extremely high theoretical specific capacity (3,861 mAh Kg^{-1}), most negative reduction potential (-3.04 V versus standard hydrogen electrode) and lightest density (0.53 g cm^{-3}) of all metals.[128, 129] However, lithium metal anode (LMA) still suffers from several critical issues including poor cycling stability, low Coulombic efficiency (CE) and severe safety concerns.[130, 131] Fundamentally, lithium metal is highly reactive with liquid organic electrolyte, which leads to the formation of unstable solid electrolyte interface (SEI). This fragile SEI fails to accommodate the infinite volume fluctuation caused by uncontrollable striping/plating of lithium metal and suffers reiterated growth and break, which in return promotes the continues consumption of electrolytes and lithium metal leading to decreased CE and poor lifespan.[132, 133] Moreover, the nonuniform SEI implies inhomogeneous local surface potential and current density,

which induces uneven lithium ion flux followed by generation of lithium dendrites, resulting in increased risk of piercing through the separator and even severe safety issues of short circuit.[134] In light of significance of SEI layer for high-performance LMA, considerable efforts have been devoted to reinforce the stability of the original SEI or construct robust artificial SEI films.[135-137] Specific lithium salts such as $LiNO_3$, Li_2S_x, LiFSI et al.[138-142] and additives like fluoroethylene carbonate (FEC) and vinylene carbonate (VC) et al.[143-146] are employed in the electrolytes to produce homogenous SEI films by preferential decomposition. However, most of the electrolyte-derived SEI films are not robust enough to withstand the growth of lithium dendrites.[147] In addition, these sacrificial components are consumed successively upon cycling, which causes structure evolution of SEI and limited stability of LMA.[133] Constructing functional artificial SEI is another promising strategy to prevent the liquid electrolyte depletion and lithium dendrites growth.[148] An ideal artificial SEI layer should be able to protect lithium metal from electrolyte deposition, regulate uniform lithium deposition and be electrochemically and mechanically stable during repeated charging-discharging process.[149] Inorganic compounds such as Li_3N,[150] LiF,[144, 151] $Li_{13}In_3/LiCl$,[152] LLZO[153] and Li_xSn_y[154] et al. have been reported to improve lithium striping/plating dynamics.[155] Nevertheless, these inorganic lithium compounds usually present inferior interfacial contact with LMA and poor mechanical strength to accommodate the volume fluctuation during cycling, which causes limited lifespan. Recently, polymeric artificial SEIs have attracted considerable attention due to their structure robustness, improved ionic conductivity and low interfacial resistance. Various polymers (such as PEO,

PVDF and PAA)[156-159] and polymer composites (such as PEO/LLZO, mPPy-GO, m-SiO$_2$/PVDF)[160-162] have been attempted to protect LMA. Although enhanced performance has been obtained, the layered structure of this *ex-situ* prepared LMA still suffers from large resistance and unavoidable lithium consumption. Recently, a series of polymers with reactive sites toward lithium metal have been attempted to form *in-situ* artificial SEI layer to stabilize LMA.[143, 163-165] Benefiting from the passivated lithium surface and robust structure of coated polymers, longer cycling life has been achieved, indicating that synthesizing polymer SEI via *in-situ* route is a promising strategy for high-performance LMA. However, these *in-situ* generated polymer SEIs still face challenges such as nonuniform distribution, weak binding affinity with lithium metal and uncontrollable morphorlogy, etc.,[143] which leads to uncontrollable lithium deposition in cycling. Therefore, designing polymeric artificial SEI via *in-situ* route with better functionality and structure control at molecular level to enforce LMA protection is still highly desired.

Surface potential distribution of SEI layer is a key factor that regulates homogenous Li$^+$ flux to reduce the generation of lithium dendrites, but such factor was rarely considered in designing artificial SEI. Herein, a monomer with rich chemical functionalities, namely 2,3,7,8-tetrakis((trimethylsilyl)ethynyl)pyrazino[2,3-*g*]quinoxaline-5,10-dione (PQ), was employed to form an artificial SEI with uniform surface potential distribution on LMA in two steps. First, a self-assembly monolayer of PQ was grafted on the surface of lithium metal due to its high reactivity with lithium. Then *in-situ* polymerization between diketone in PQ and active terminal alkyne

generated by deprotected of TIPS groups by Tetra-n-butylammonium fluoride (TBAF) yielded a polymeric PQ artificial SEI (PPQ). Such chemical passivation of the lithium metal surface protects it from electrolyte decomposition. Moreover, the cross-linked electronegative network also enables uniform Li deposition as a lithium ion redistributor. Additionally, the robust structure accommodates the large volume fluctuation and prevent the generation of lithium dendrites. As a result, the modified LMA (PPQ-stabilized Li) exhibits an impressive electrochemical performance, including an improved CE of 98% and prolonged cycling stability with ultra-thin (50 μm) lithium anode at current density of 0.5 mA cm^{-2}. Full cells using LiNi$_{0.8}$Co$_{0.1}$Mn$_{0.1}$O$_2$ (NCM) as cathode and PPQ coated ultra-thin lithium metal as anode delivered a higher initial capacity of 183. 6 mAh g^{-1} and there was still 140.0 mAh g^{-1} remained after 350 cycles with high average CE up to 99.9%.

3.2 Experimental Methods

3.2.1 Raw Materials

Organic solvents, reagents and starting materials were purchased from Adamas®, Alfa Aesar, Sigma-Aldrich or Acros Organics, and were used without further purification. Monomer 2,3,7,8-tetrakis((trimethylsilyl)ethynyl)pyrazino[2,3-g]quinoxaline-5,10-dione was synthesized according to the literatures. [1,2] Thick lithium foils (450 μm) and ultra-thin lithium foils (50 μm) were purchased from China Energy Lithium Co., Ltd.

3.2.2 Synthesis of poly(pyrazinoquinoxaline) powder material (PY-NBu₄)
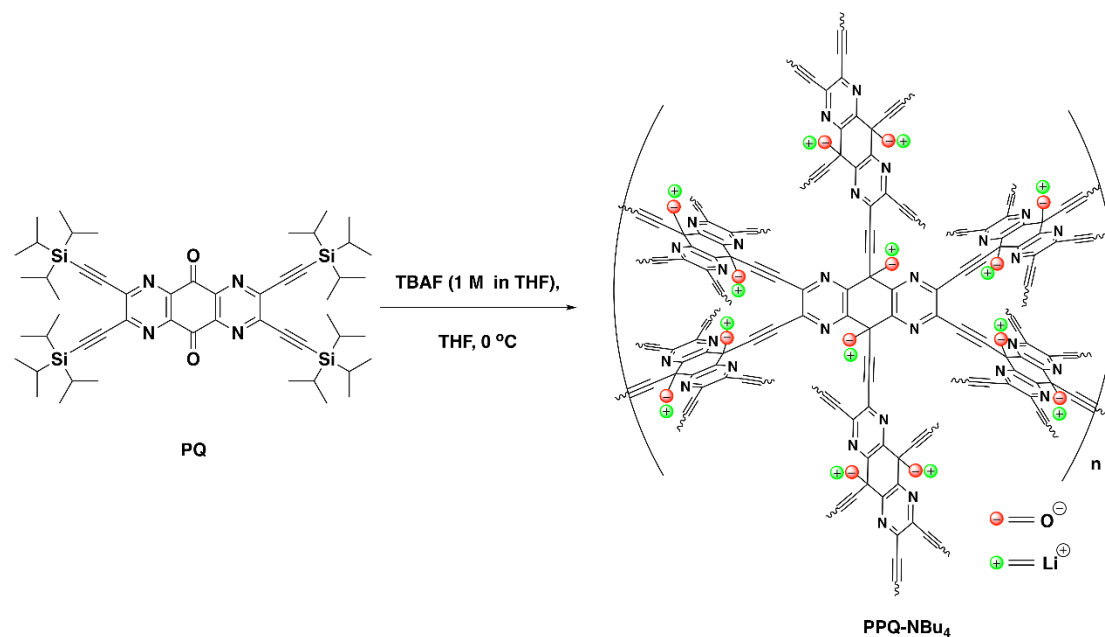
Fig. 3.1 | Synthetic route of polymeric PQ (PPQ) powder with NBu4 ion (PPQ-NBu4) by solution method.

The synthesis route is illustrated in **Fig. 3.1**. An oven dried three-neck flask was charged with 2,3,7,8-tetrakis((trimethylsilyl)ethynyl)pyrazino[2,3-*g*]quinoxaline-5,10-dione (1 g, 1.07 mmol) and anhydrous THF (500 mL) under N_2 atmosphere. To this solution, TBAF (1 M in THF, 9.42 mL, 9.4 mmol) diluted in 50 mL of THF was added dropwise over 10 min at 0 °C. A rapid color change from brown to black was observed. The mixture was stirred at 0 °C for 8 h. The resulting cross-linked polymer network was collected by suction filtration, washed with THF (50 mL *3), and then grounded with a mortar. After being extracted in a Soxhlet extractor sequentially with THF for 24 h, and then dichloromethane for 24 h, the black powder was collected and dried in an oven at 60 °C overnight to yield 0.368 g of the desired polymer. This material was used

for FTIR, Raman, XRD, TGA (**Fig. 3.2**). solid-state ^{13}C NMR (101 MHz): δ (ppm)

177.37, 144.89, 141.53, 107.94, 102.39, 18.85, 11.56 (**Fig. 3.3**).
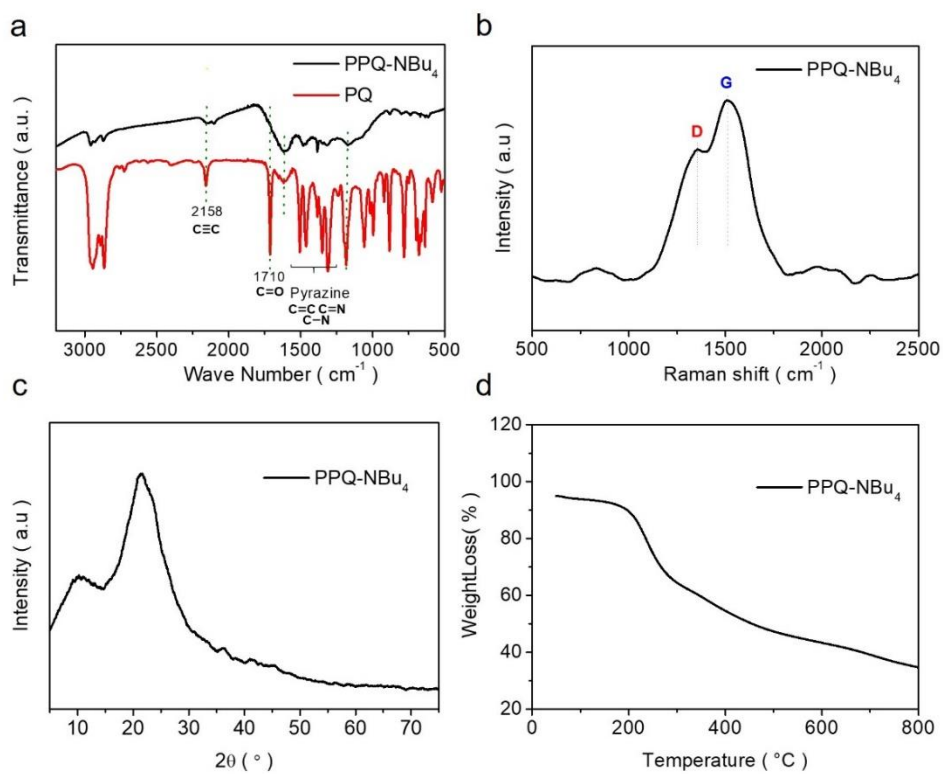
Fig. 3.2 | a, FTIR spectrum of PPQ-NBu₄ powder and PQ monomer. **b-d**, Raman

spectrum, XRD pattern and TGA curve of PPQ-NBu₄ powder.
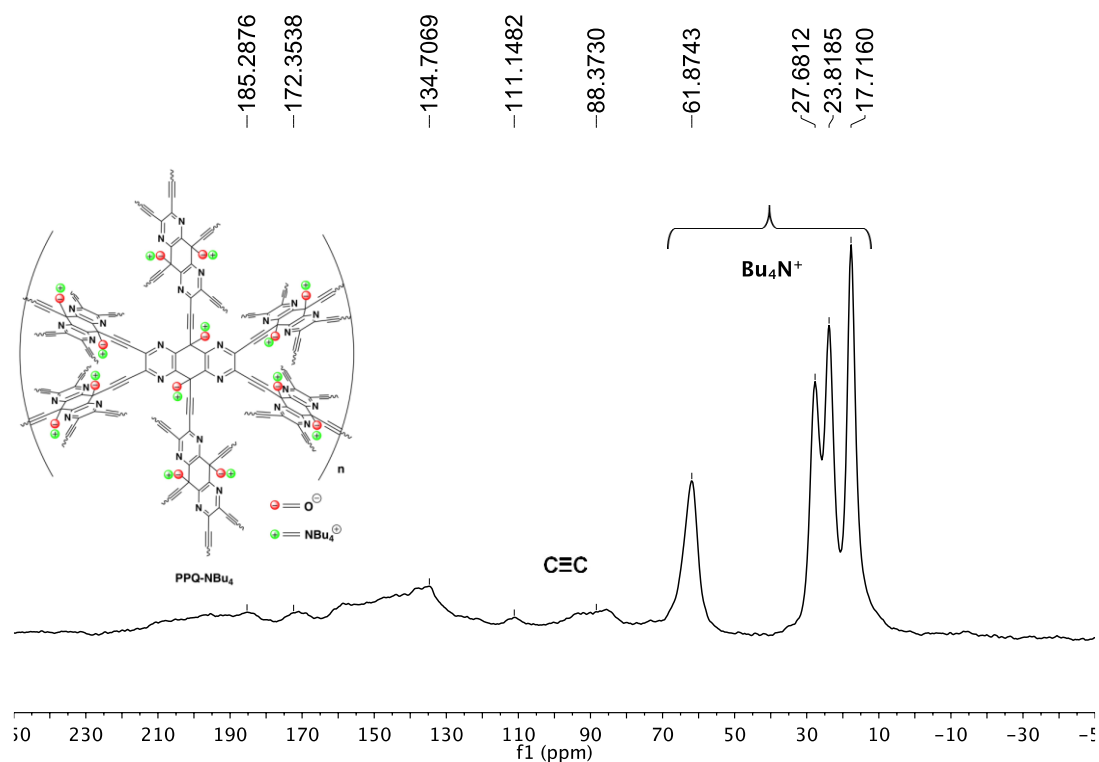
Fig. 3.3 | Solid-State ^{13}C NMR spectrum of PPQ-NBu$_4$ (101 MHz).

3.2.3 Synthesis of free standing PPQ-NBu$_4$ film

2,3,7,8-tetrakis((trimethylsilyl)ethynyl)pyrazino[2,3-g]quinoxaline-5,10-dione (80 mg) was dissolved in 50 mL of dichloromethane in a 250 mL beaker. 30 mL of distilled water was added slowly on top of the organic solvent. After cooling down to 0 ºC, 1.5 mL of TBAF (1 M in THF) was added carefully to the solution. A clear two-solvent interface was well preserved and the system was kept at room temperature (25 ºC) for 36 h. A black film formed at this interface was collected after removal of all volatiles. This membrane material was used for SEM and TEM characterizations (**Fig. 3.4**).
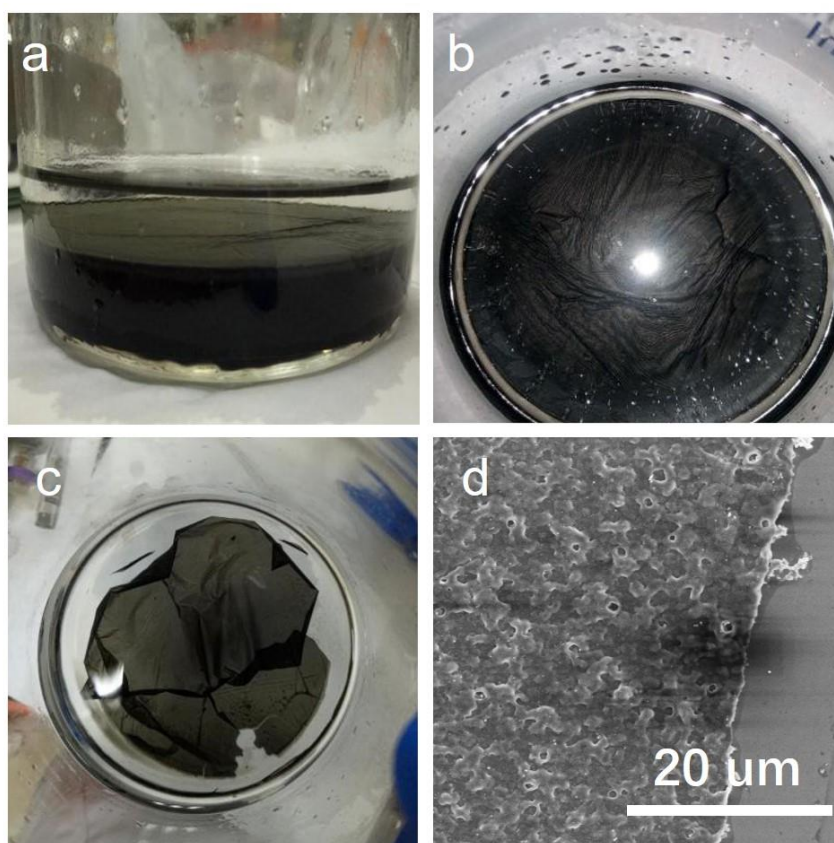
Fig. 3.4 | a-c, Photographs of synthesis of free standing PPQ-NBu4 film. **d**, SEM image of free standing PPQ-NBu4 film.

3.2.4 Synthesis of poly(pyrazinoquinoxaline) powder exchanged with lithium ion (PPQ-Li)

150 mg of PPQ-NBu4 powder was added to 500 mL of lithium chloride solution (1 M in H_2O). After sonication for 6 h, the solids were collected by filtration with PVDF membrane filter (0.2 μm), washed with distilled water (50 mL * 3), and dried at 60 ºC in a vacuum oven to yield 118 mg of PPQ-Li (**Fig. 3.5**). Solid-state ^{13}C NMR (101 MHz): δ (ppm) 177.37, 144.89, 141.53, 107.94, 102.39, 18.85, 11.56 (**Fig. 3.6**).
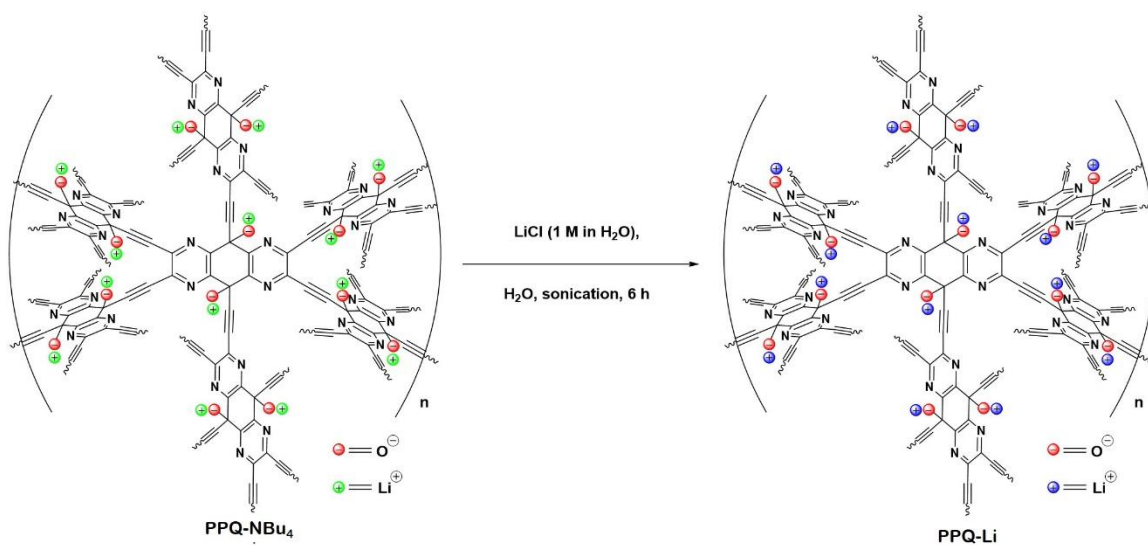
Fig. 3.5 | Synthetic route of the poly(pyrazinoquinoxaline) powder exchanged with lithium ion (PPQ-Li).
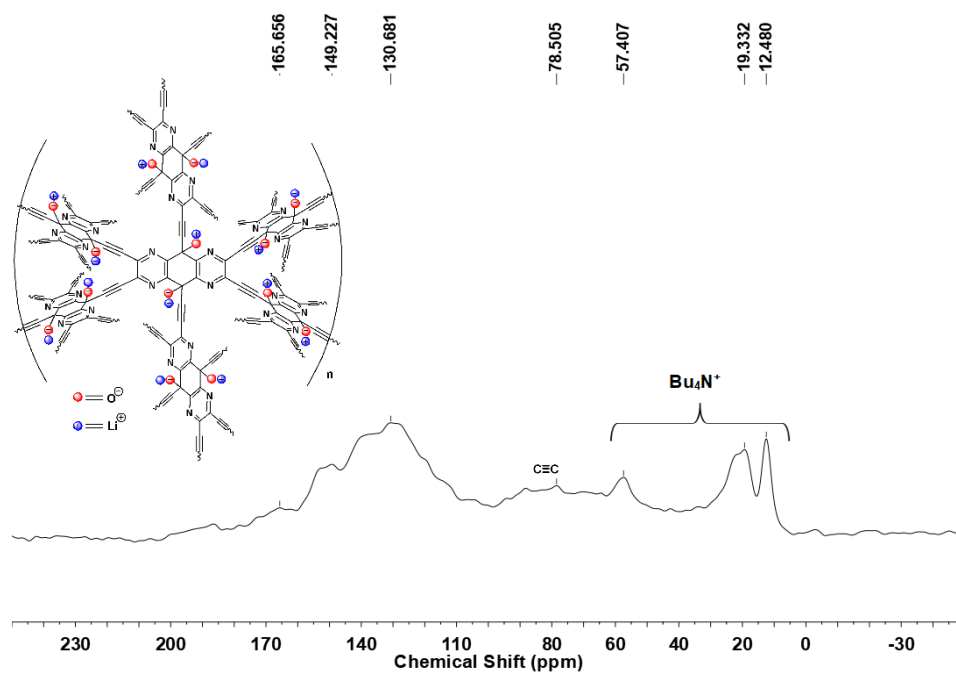
Fig. 3.6 | The Solid-State ^{13}C NMR spectrum of PQ-Li (101 MHz).
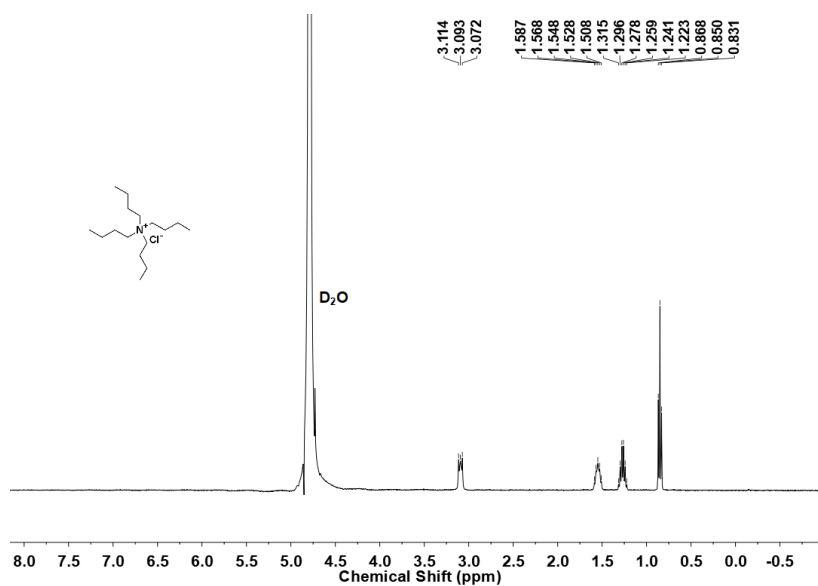
Fig. 3.7 | The ^{13}H NMR spectrum of filtrate from the cation-exchange of PQ-Li (400 MHz, D₂O).

3.2.5 Synthesis of poly(pyrazinoquinoxaline) artificial SEI film stabilized Li metal anode (PPQ-stabilized Li)

The *in-situ* self-assembled PPQ SEI layer was fabricated on a lithium chip by using a simple spin-coating method. And all the following procedures were conducted in an argon-filled glovebox with water and oxygen contents less than 0.1 ppm. First, 2,3,7,8-tetrakis((trimethylsilyl) ethynyl) pyrazino [2,3-g] quinoxaline-5,10-dione powder (1 mg, 0.00107 mmol) was dissolved in anhydrous 1,3-dioxolane (DOL) (1 mL) and a yellowish solution was acquired. Then, 30 μL of the solution was transferred on a lithium chip. The lithium foil was spun on a spin coater model KW-4A (CHETMAT Technology) (spin speed of 1000 rpm at 5 s) to let it form a self-assembly monolayer on the lithium surface. Afterward, a 20 μL of 1 M TBAF dilution (1M in THF diluted in DOL, 5%, v/v) was added to help to build the cross-linked network (spin speed of

93

1000 rpm at 30 s). The solvent on Li-surface was evaporated slowly while polymerization and self-assembly of the monomer happened on this surface. Eventually, the lithium chip was dried in the glovebox overnight at the room temperature overnight, and a conformal polymer membrane was formed.

3.2.6 Material characterization

The crystal structure was characterized by X-ray diffraction (XRD, Rigaku Dmax-3C Cu-Ka). The morphology was observed by field scanning electron microscopy (FESEM, HITACHI, S-4800) with energy dispersive x-ray spectroscopy (EDS), and transmission electron microscopy (TEM, JEOL-2010 F, 200 KV). The Fourier transformation infra-red spectrum (FTIR) were obtained on an AVATAR 370 FT-IR spectrometer. X-ray photoelectron spectroscopy (XPS) was done on a PerkinElmer PHI 5000CESCA system to analyze electronic states. es. Allthe binding energies were calibrated by using the contaminant carbon (C1s = 284.8 eV) as a reference. Thermal gravimetric analysis (TGA) profiles were obtained on a TA-Q500 thermogravimetric analyzer with a heating rate of 10 °C min-1 from room temperature to 800 °C in Ar atmosphere. AFM micrographs of the LMA surface were obtained with the SPM-9700HT Scanning Probe Microscope (Shimadzu, Kyoto, Japan) using a silicon tip (resonance frequency = 320 kHz, force constant = 42 N·m^{-1}). The Raman spectroscopy was recorded on a Spex 1403 instrument with an excitation laser wavelength of 514.5 nm.^{1}H NMR, solution and solid-state ^{13}C NMR spectra were obtained from a Bruker Avance（III）(400 MHz) spectrometer at Shanghai Normal University.

3.2.7 Cell assemble and electrochemical test

Electrochemical studies were all performed using CR2032 coin cells (MTI Corporation) and assembled in an Ar-filled glove box (O_2/H_2O < 1 ppm). Polypropylene membrane was used as separator for all the cells, and the electrolyte used was 1 M $LiPF_6$ in Fluoroethylene carbonate:dimethyl carbonate (FEC/DMC) (Merck, Germany) in volume ratio of 1:4. The amount of electrolyte for each cell was 40 µL. All the electrochemical measurements were performed at constant temperature (25 °C) using a battery test systems (CT2001A, LAND). To measure the Coulombic efficiency (CE) of Li deposition/dissolution, the asymmetric cell was assembled by applying PYA coated thin lithium metal foils (50 µm) as working electrode and lithium metal as counter electrode. All the lithium on the working electrodes was stripped initially at current density of 0.5 mAh g^{-1}. Cyclic voltammetry was conducted using a potentiostatic/galvanostatic electrochemical workstation (Bio-Logic SAS, MPG-2 or VSP-300, Claix, France) with a scan rate of 1 mV s^{-1} from 0 to 5 V. The control cells with bare thin lithium metal foil as working electrode were measured under the same condition. All the symmetric cells were assembled with two lithium metal foils and they were tested at the current density of 0.5 and 1 mA cm^{-2} with an areal capacity of 1.0 mAh cm^{-2}.

The $LiNi_{0.8}Co_{0.1}Mn_{0.1}O_2$ sheets were prepared as the cathode for full cells test by mixing $LiNi_{0.8}Co_{0.1}Mn_{0.1}O_2$ (Li-FUN technology), super P, and polyvinylidene fluoride (PVDF) with a weight ratio of 8:1:1 in N-methyl-2-pyrrolidone (NMP). The cycling of

the NCM|PPQ-stabilized Li and NCM|bare-Li cells was tested between 2.8 to 4.3 V at various C rates (1C = 140 mA g^{-1}).

3.2.8 Computational calculations
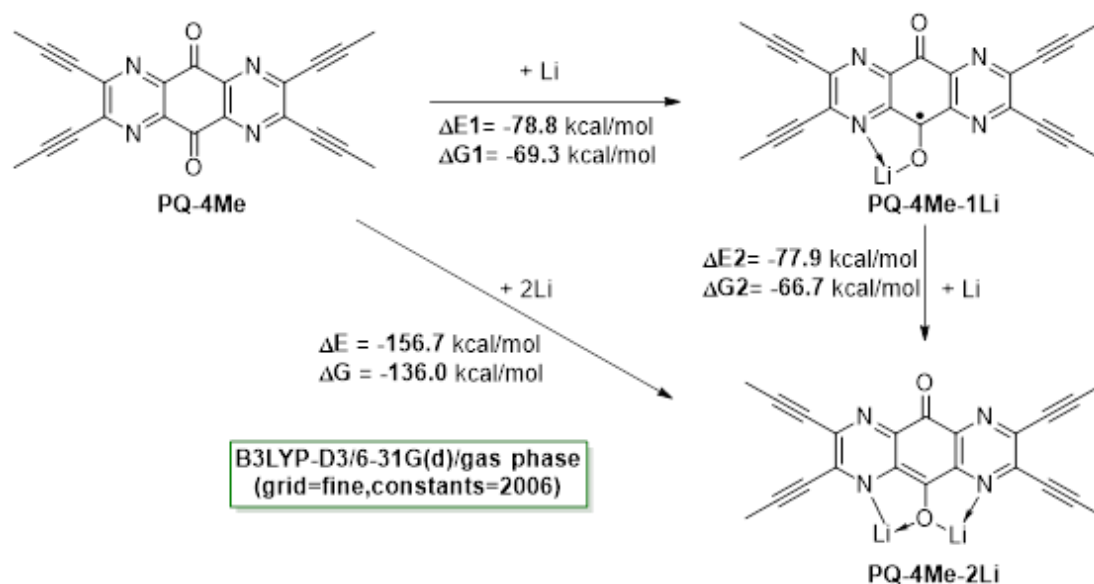
Fig. 3.8 | Computational result on the reaction of lithium with **PQ-4Me** (simplified PQ monomer, with trimethylsilyl group being simplified as methyl group) suggesting that self-assembly of PQ on lithium metal anode is thermodynamically feasible.

Preliminary Density Functional Theory (DFT) study with Gaussian 16[166] at B3LYP-D3[167-171]/6-31G(d) (in vacuum) level (grid = fine, constants = 2006 was utilized to save computational costs) on the simplified model compound (trimethylsilyl group was simplified as methyl group, **Fig. 3.8**) suggests that, both 1e and 2e reduction of the PQ monomer carbonyl group are thermodynamically favorable. This computational result indicates high reactivity of PQ monomer with lithium, supporting the formation of a

PQ monolayer on lithium metal.

Table 3.1. Absolute energies for structures shown in **Fig. 3.8**. Calculated at B3LYP-D3/6-31G(d) (in vacuum) level (grid = fine, constants = 2006).

Entry	Electronic Energy (Hartree)	Gibbs Free Energy (Hartree)
PQ-4Me	-1214.76831418	-1214.55586100
Li	-7.49090229	-7.50430500
PQ-4Me-1Li	-1222.38480218	-1222.17060300
PQ-4Me-2Li	-1229.99988104	-1229.78119600

Cartesian coordinates of all the optimized structures shown in Fig. 3.8.

PQ-4Me

Charge=0 Multiplicity=1

C,-2.8358788262,1.1027447913,0.7006127096

C,-2.5431420861,2.3895217543,0.1288221883

N,-1.2949830164,2.7213887084,-0.2111509779

C,-0.334249019,1.8124096856,0.0010267059

C,-0.6205071127,0.5541251174,0.5600732455

N,-1.8670471726,0.2067790787,0.9061411252

C,1.0642141386,2.2099110321,-0.3903358623

C,2.1386857207,1.183214164,-0.1489338038

C,1.852417842,-0.075119722,0.409993965

C,0.4539588297,-0.4725996514,0.8014154506

N,3.3852417001,1.5306203238,-0.494872745

C,4.3540714912,0.634636781,-0.289416786

C,4.0613057315,-0.6522468888,0.2821099614

N,2.8131380101,-0.9841390575,0.6220507549

O,0.2067811253,-1.5591499695,1.2841771584

O,1.3113886748,3.2964525125,-0.8731181879

C,-4.1687930295,0.756322798,1.0606028026

C,-3.5811492513,3.3392961111,-0.0873930846

97

C,5.0992892319,-1.6020926613,0.4981151172

C,5.6869918665,0.9812573959,-0.6492151241

C,5.9921706431,-2.4009959604,0.676863903

C,6.825713227,1.2632963052,-0.9512123476

C,-4.4739947427,4.1382165581,-0.2662440426

C,-5.3076295405,0.4746871,1.3625436164

C,-6.6733609794,0.1250037463,1.7295268827

H,-7.364439435,0.9514219993,1.525583627

H,-7.0167526406,-0.7516157333,1.166619627

H,-6.7408576922,-0.1188117346,2.7968509769

C,-5.5393601945,5.1072983362,-0.4854640139

H,-5.5323221635,5.468881974,-1.5209248726

H,-6.5240072257,4.668755087,-0.2847324638

H,-5.4160246166,5.9776581405,0.1708201315

C,8.1913476644,1.6138000076,-1.3177829235

H,8.5767555872,2.410733064,-0.6698346571

H,8.8616077902,0.7507545938,-1.2280647779

H,8.2382710674,1.9753778565,-2.3521921098

C,7.0576479336,-3.3699840538,0.8959616667

H,6.9392845231,-4.2362768782,0.2333956009

H,8.042770671,-2.9287704945,0.7035808573

H,7.0452810254,-3.7382237071,1.9290151566

Li

Charge=0 Multiplicity=2

Li,0.98326358,-0.2301058,-0.00301224

PQ-4Me-1Li

Charge=0 Multiplicity=2

C,-2.8186762191,1.0869776725,0.6713649129

C,-2.536234622,2.3881946821,0.1264725525

N,-1.2914984746,2.7331737073,-0.2059663914

C,-0.3179572327,1.834406775,-0.0175023113

C,-0.5969395503,0.5446469882,0.5221671835

N,-1.8563341983,0.1912791775,0.8603250893

C,1.0643908347,2.2599110275,-0.402746419

C,2.1290759721,1.2307695228,-0.1792314253

C,1.7954520495,-0.0454164174,0.3639085938

C,0.4568160251,-0.4378177009,0.7296355747

N,3.3794224127,1.5462614432,-0.5012627801

C,4.3442030021,0.630333114,-0.3051277185

C,4.0324180993,-0.656076161,0.2383067704

N,2.7779561703,-0.9766049368,0.5629704886

O,0.2360743265,-1.6057148539,1.2131697845

O,1.312712052,3.3628236143,-0.8657249535

C,-4.1549020118,0.7237546527,1.0258941142

C,-3.579264956,3.3408148803,-0.0716147306

C,5.0403608231,-1.6431541986,0.4546271609

C,5.6840989177,0.966174019,-0.6493801757

C,5.878983466,-2.4936621701,0.6457435155

C,6.8261690053,1.2407179599,-0.9382667894

C,-4.4725481196,4.1392485645,-0.2346117919

C,-5.2893222801,0.4298650109,1.3214417046

H,7.8288830471,1.4961377215,-1.1970074424

H,6.6422716207,-3.2230053593,0.8018599345

H,-6.2888770526,0.1659831817,1.5838235826

H,-5.2538009238,4.8500634387,-0.3822732617

Li,1.7763350465,-2.5161429454,1.3141631682

PQ-4Me-2Li

Charge=0 Multiplicity=1

C,-2.8011650527,1.0978512415,0.7157460221

C,-2.5363128438,2.3761597055,0.1495347542

N,-1.277437086,2.7237038541,-0.1978500394

C,-0.2925189356,1.8617734269,-0.005709423

C,-0.5336283041,0.5576356465,0.5672081637

N,-1.819317751,0.2088775801,0.9194616765

C,1.09011204,2.2780975307,-0.401421432

C,2.1448067453,1.2454302153,-0.1508005529

C,1.8014529988,-0.0328550381,0.4281950432

C,0.48827644,-0.381093811,0.7847393336

N,3.3921185548,1.5428866056,-0.4758210721

C,4.3658984058,0.6307515804,-0.2613453018

C,4.0547711486,-0.6358632078,0.3076061372

N,2.7986202047,-0.9589020035,0.6445411044

O,0.2098327997,-1.6114451256,1.3335428445

O,1.3379400649,3.3731131824,-0.8898691241

C,-4.1242327316,0.7131479345,1.0887984927

C,-3.5878541557,3.313171969,-0.0624843128

C,5.0698888822,-1.6118382394,0.5414496051

C,5.7047646066,0.9632910535,-0.6156574715

C,5.9386961318,-2.4348134652,0.7365419196

C,6.8458384596,1.241348623,-0.9154430485

C,-4.4863517871,4.1069739196,-0.2408600362

C,-5.2513267043,0.3949016184,1.4027317965

Li,1.8083828482,-2.4208696919,1.4041185848

C,-6.6238011255,0.058020832,1.7642514663

H,-7.3006064526,0.8896287375,1.5343107433

H,-6.9767299203,-0.8233248975,1.2144165459

H,-6.7124707897,-0.1599458716,2.8358239758

C,-5.5548064029,5.0743971836,-0.4626042137

H,-6.3217167666,4.6773286762,-1.1403625272

H,-6.0518741377,5.3462714753,0.4777094157

H,-5.1618454509,5.9959598528,-0.9091091841

C,8.2128062648,1.5929143605,-1.2821492817

H,8.8809151414,1.5691123188,-0.4113772016

H,8.6186516576,0.8998493026,-2.0305621777

H,8.2565220664,2.6032625265,-1.7068253763

C,7.0183549698,-3.3917638081,0.9520793552

H,6.8477662371,-4.3192339755,0.3914155375

H,7.9779196103,-2.9739517205,0.6247001739

H,7.1120822767,-3.6558323349,2.0127987616

Li,-1.5622034772,-1.568489802,1.6048358832

3.3 Results and Discussions
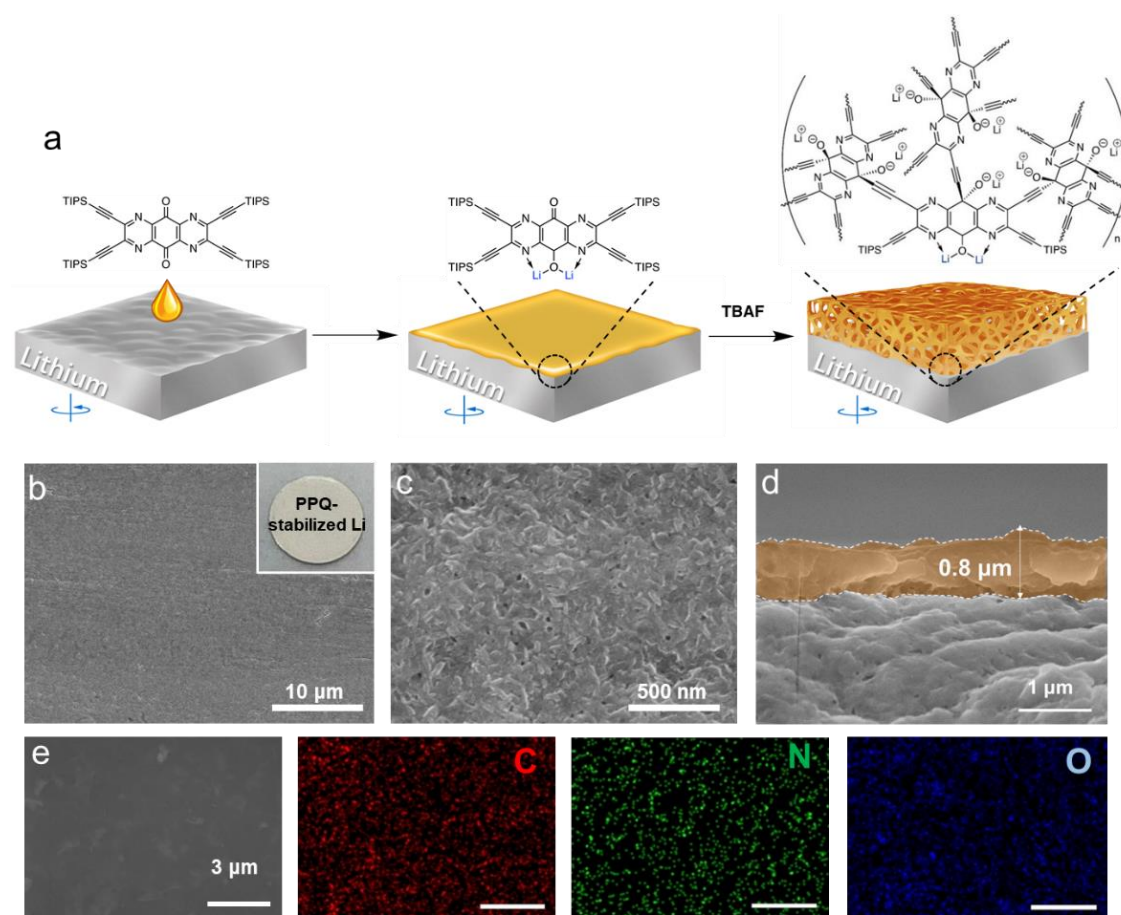
Fig. 3.9 | a, Schematic illustration of the *in-situ* process of PPQ coated modified lithium metal anode (PPQ-stabilized Li). **b** and **c**, Top-view SEM images and optical image (inset) of PPQ -Li anode. **d**, Cross-sectional SEM image of PPQ-stabilized Li. **e**, SEM image of the PPQ-stabilized Li anode and corresponding elemental mapping images of carbon, nitrogen and oxygen.

The synthesis of PPQ protected LMA is illustrated in **Fig. 3.9a**. Firstly, PQ monomer is uniformly spread on the surface of fresh lithium metal by spin coating. As illustrated in **Fig. 3.8**, the strong bonding between the N and O in PQ with lithium has an entropy

gain of over 136 kcal/mol, which induces the spontaneous self-assemble by the chemical reaction between N, O and Li generating a dense passive layer. Subsequently, *in-situ* polymerization between ketone groups in PQ and active terminal alkyne generated by deprotected of TIPS groups by TBAF takes place to form cross-linked polymer network.

This *in-situ* polymerization process was also confirmed by parallel experiments to obtain PPQ-NBu4 powder in solution synthesis (**Fig. 3.1**) and high-quality free-standing PPQ-NBu4 films by interfacial synthesis at dichloromethane/H2O interface (**Fig.3.4**). The successful addition of the terminal alkyne to the ketone of PPQ-NBu4 powder was confirmed by solid state ^{13}C NMR (, Fourier transformation infra-red spectrum (FTIR) and Raman spectroscopy (**Fig. 3.2**), which showed significantly decreased C=O carbon signal around 177.4 ppm on ^{13}C NMR spectrum and the disappearance of the C=O stretching signal at 1710 cm-1 on FTIR spectrum, respectively. It should be noted that the NBu4$^+$ ion in PPQ-NBu4 could be exchanged by lithium ion due to the porous structure of PPQ-NBu4 polymer, which can facilitate the lithium ions transfer through the cross-linked PPQ layer during charging-discharging process. After ion exchange (**Fig.3.5**), a PPQ-Li species (**Fig.3.6**) could be obtained and most of the NBu4$^+$ ions were exchanged out by lithium ion as indicated by the ^{1}H NMR spectrum of the filtrate (**Fig.3.7**).

There is almost no obvious optical change on the coated lithium metal surface (inset of **Fig. 3.9b**) due to the ultra-thin PPQ layer. However, as shown by scanning electron

microscopy (SEM) images of PPQ coated Li metal anode (PPQ-stabilized Li) (**Fig. 3.9c**), a uniformly distributed dense polymeric artificial SEI with a thickness of approximately 0.8 μm can be observed on the surface of lithium metal according to the cross-sectional SEM image (**Fig. 3.9d**). Elemental analysis of carbon, nitrogen and oxygen are carried out and exhibited in **Fig. 3.9e**, conforming homogenous distribution of the as-prepared PPQ film.
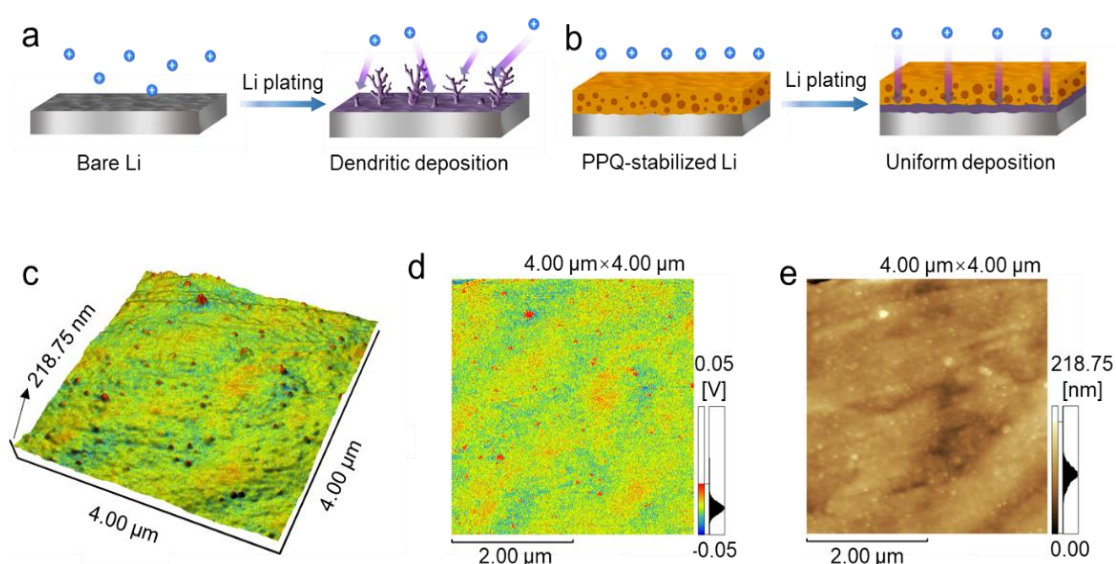
Fig. 3.10 | Schematic illustration of **a**, lithium plating on bare Li and (**b**) PPQ-stabilized Li electrode. **c-e**, 3D and 2D AFM images of the surface height and surface potential distribution.

As shown in **Fig. 3.10a**, the bare Li anode suffers serious lithium dendrites during Li plating process due to the delicate electrolyte-derived SEI and uneven lithium-ion flux. In contrast, the designed PPQ SEI containing a passive monomer layer grafted on

lithium metal surface and integrated cross-linked polymers, is dense and robust enough to block the electrolyte access to lithium surface and suppress growth of lithium dendrites (**Fig. 3.10b**). Since the surface uniformity including thickness and potential distribution of SEI significantly influence the deposition of lithium, we detected the surface roughness and surface potential of PPQ-stabilized Li by Atomic force microscopy (AFM). Notably, the 3D (**Fig. 3.10c**) and 2D (**Fig. 3.10d**) surface potential distribution demonstrates a homogenous negative-charged surface potential on the surface of PPQ-stabilized Li, which can fundamentally prevent the generation of lithium dendrites by regulating uniform lithium flux and repelling anions. In addition, it presents a smoother surface with surface roughness less than about 219 nm (**Fig. 3.10e**), verifying its homogenous distribution.
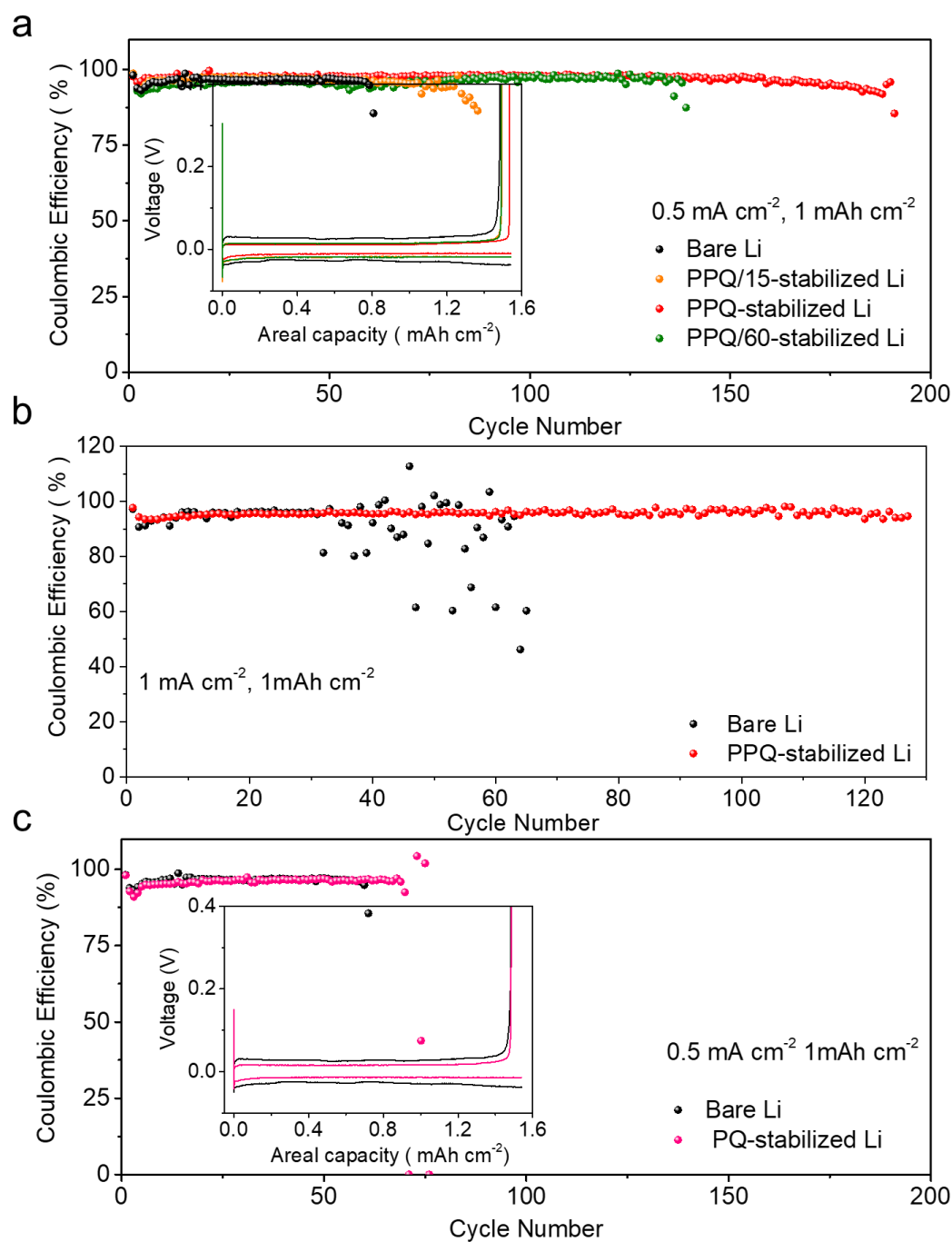
Fig. 3.11 | Cycling Coulombic efficiencies of (a) Li|bare Li, Li|PPQ/15-stabilized Li Li|

PPQ-stabilized Li and Li|PPQ/60-stabilized Li as-symmetric cells at 0.5 mA cm^{-2}, 1

mAh cm^{-2}. **b**, Coulombic efficiencies of Li|bare Li and Li|PPQ-stabilized Li as-

symmetric cells at 0.5 mA cm^{-2}, 1 mAh cm^{-2} and 1 mA cm^{-2}, 1 mAh cm^{-2}, respectively.

c, Li|bare Li and Li|PQ-stabilized Li as-symmetric cells at 0.5 mA cm^{-2}, 1 mAh cm^{-2}.

Insets are the corresponding galvanostatic lithium striping/plating curves.

In order to evaluate the electrochemical performance of artificial SEI protected LMA, ultra-thin lithium foil with a thickness of 50 μm was used to fabricate PPQ coated LMA (PPQ-stabilized Li). Before the galvanostatic charge-discharge process, all the lithium on PPQ-stabilized Li was initially stripped to the counter electrode forming a PPQ protected Cu electrode. Bare Li anode was measured under the same condition for comparison. Figure X(a) exhibits the galvanostatic voltage profiles of Li stripping/plating on bare Li and PPQ-stabilized Li electrode at current density of 0.5 mA cm^{-2}. It is apparent that PPQ-stabilized Li electrode shows a higher Coulombic efficiency of 99.7% due to the prevented electrolyte decomposition under the protection of dense PPQ layer. Moreover, PPQ-stabilized Li electrode presents both lower nucleation and plateau potential of 31 mV and 11 mV, respectively, implying regulated lithium deposition and enhanced lithium ion transfer. **Fig. 3.11a** exhibits the CEs of Bare Li and PPQ-stabilized Li electrodes at a current density of 0.5 mA cm^{-2} and capacity of 1 mAh cm^{-2}. Even experiencing large volume shrinkage of initial lithium stripping, the protected PPQ-stabilized Li electrode prolongs the cycle life up to 180 cycles with a higher average CE of ~98%, which demonstrates that the *in-situ* generated polymer membrane can effectively regulate the lithium deposition without lithium dendrites growth and also be robust enough to withstand large volume fluctuation. When the current density is increased to 1 mAh cm^{-2}, prolonged cycling life over 120 cycles could be obtained with an average CE of ~96% (**Fig. 3.11b**). On the contrary,

the bare Li anode shows apparent collapse within 50 cycles and 30 cycles at current densities of 0.5 mA cm^{-2} and 1 mA cm^{-2} attributing to the unstable electrolyte-derived SEI layer. Besides, we also optimized the thickness of PPQ layer by adapting the amount of added monomer solution. Besids, the cell with a PPQ/15-Li (15 μL monomer solution used) as working electrode shows a fast degradation after around 80 cycles which is more stable than the cell with a bare Li electrode, though still worse than the cell with PPQ-stabilized Li electrode. This improved cycling performance is associated with the modification of PPQ layer, however, this thinner PPQ layer is not stable enough to accommodate repeatedly volume fluctuation. Moreover, the LMA coated with a thin monomer layer coating also presents shorted cycling life (**Fig. 3.11c**) due to the fragile structure, implying the significance of the cross-linked polymer film which provide robust structure to suppress the generation of lithium dendrites and buffering the volume expansion. With a thicker PPQ film, PPQ/60-Li anode (60 μL monomer solution used) shows lower CE and limited lifespan compared with PPQ-stabilized Li anode which may be ascribed to the increased interfacial resistance and decreased flexibility caused by thickened polymer layer. The insets show the galvanostatic voltage profiles of bare Li, PPQ coated Li and monomer coated Li which demonstrates that all the modified electrodes have lower resistance due to the stabilized SEI layer.
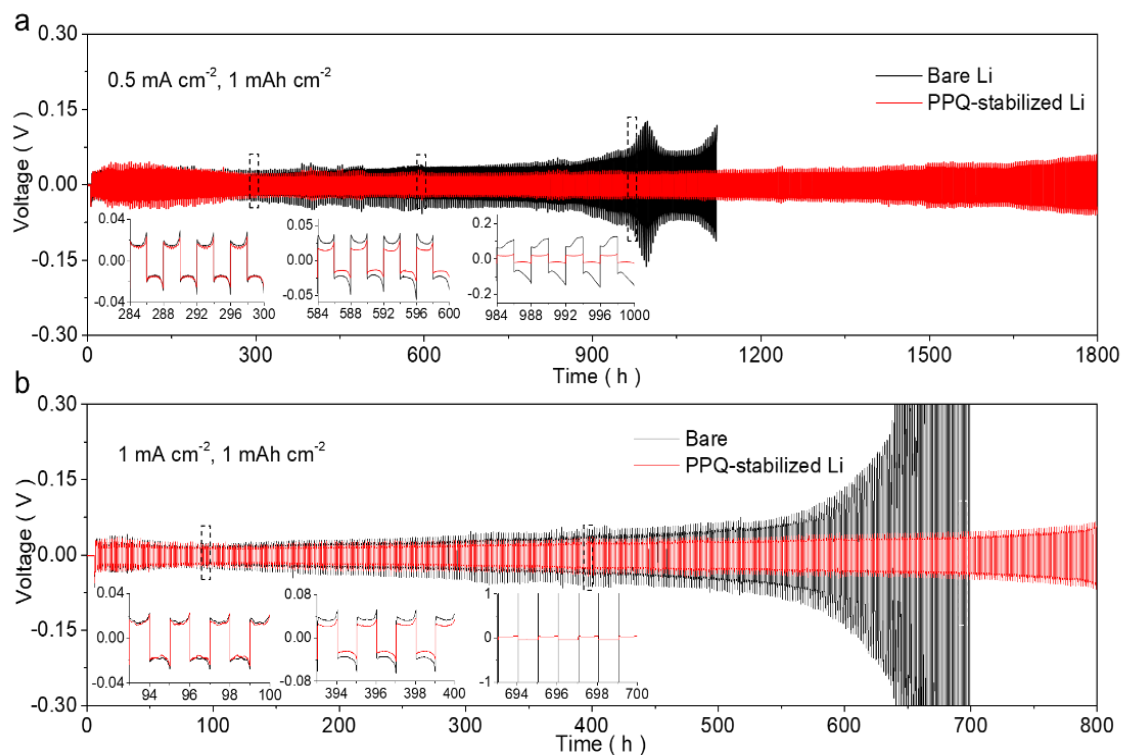
Fig. 3.12 | Galvanostatic cycling performance of **a**, bare Li|Li and PPQ-stabilized Li|PPQ-stabilized Li symmetric cells at 0.5 mA cm^{-2}, 1 mAh cm^{-2} and **b**, 1 mA cm^{-2}, 1 mAh cm^{-2}, respectively. Insets are the magnified views at selected cycle numbers.

The effect of the as-prepared artificial SEI layer on the behavior of lithium plating/stripping is further investigated by testing the bare Li|Li and PPQ-stabilized Li|PPQ-stabilized Li symmetric configurations. **Fig. 3.12a** compares the voltage vs. time profiles at current density of 0.5 mA cm^{-2} and capacity of 1 mAh cm^{-2} for each cell. Bare Li|Li symmetric cell presents decreased overpotential at the initial 200 h owing to the inevitable generation of lithium dendrites causing local short-circuit.[172] The fluctuated overpotential over 100 mV is obtained in the following cycles which can be ascribed to the accumulation and collapse of the fragile SEI layer. In contrast, PPQ-

stabilized Li|PPQ-stabilized Li cell shows much lower overpotential under 60 mV and more stable cycling lifespan up to 1800 h with no obvious voltage fluctuation. Moreover, PPQ-stabilized Li|PPQ-stabilized Li cell presents more flat voltage with smaller hysteresis than that of Bare Li|Bare Li cell according to the details in enlarged insets, which confirms that the PPQ layer effectively regulated uniform deposition of lithium metal. Similar phenomenon could be observed when the current density was increased to 1 mA cm^{-2} (**Fig. 3.12b**). The overpotential of bare Li|Li cell reaches over 200 mV within 700 h at a current density of 1 mA cm^{-2} owing to the increased interfacial resistance, while the PPQ-stabilized Li|PPQ-stabilized Li cell still displays prolonged cycling life over 800 h with smaller hysteresis voltage. This superior electrochemical performance of PPQ-stabilized Li electrode is attributed to the elaborately designed PPQ SEI layer which provides stable interface between lithium metal and liquid electrolyte.
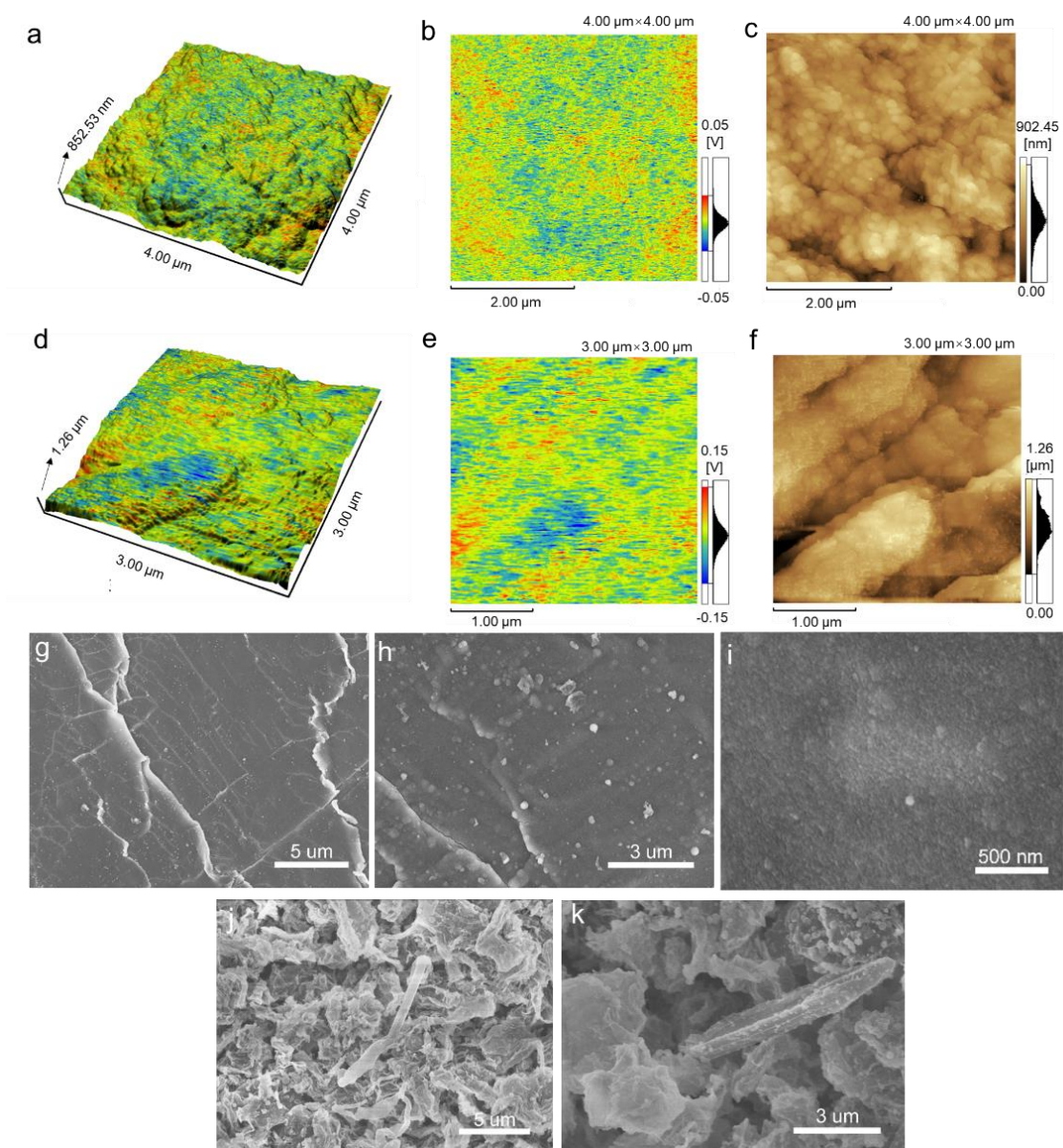
Fig. 3.13 | Surface roughness and surface potential distribution detected by AFM of **a-c**, PPQ-stabilized Li and (**d-f**) are bare Li electrodes after 100 cycles at 0.5 mA cm^{-2}, 1 mAh cm^{-2}. Top-view SEM images of **g-k**, PPQ-stabilized Li and (**k-l**) are Bare Li electrodes after 100 cycles at 0.5 mA cm^{-2}, 1 mAh cm^{-2}.

The surface potential distribution and roughness of PPQ-stabilized Li and Bare Li

electrode were investigated by AFM after cycling in symmetric cells at current density of 0.5 mA cm^{-2} and capacity of 1 mAh cm^{-2}. PPQ-stabilized Li exhibits a relatively more uniform potential distribution in a range of -0.05-0.05 V even after 100 cycles (**Figs. 3.13 a-b**), implying that a homogenous lithium flux was induced during cycling, which is favorable for free dendrites lithium deposition. Meanwhile, it possesses less rough surface (**Fig. 3.13c**) according to controllable lithium stripping/plating with smaller local volume expansion. As comparison, bare Li electrode displays quite different local surface potential due to the collapse of SEI and growth of lithium dendrites (**Figs. 3.13d-e**). The rough surface can be ascribed to the continuously break and aggregation of SEI layer. The micromorphologies of the PPQ-stabilized Li and Bare Li anodes are further studied by SEM. Notably, PPQ-stabilized Li anode remains a quite smooth surface (**Figs. 3.13g -i**) suggesting that the PPQ layer is uniformly distributed on the surface of lithium metal anode even after repeatedly lithium plating/stripping, demonstrating even lithium deposition without dendrites. However, Bare Li anode exhibits severely damaged surface and the accumulated lithium dendrites can be clearly observed (**Figs. 3.13j-k**), which is in accordance with the AFM result. This is because the electrolyte-derived SEI layer is too brittle to accommodate the large volume fluctuations during cycling which leads to the collapse of SEI and subsequent growth of lithium dendrites.
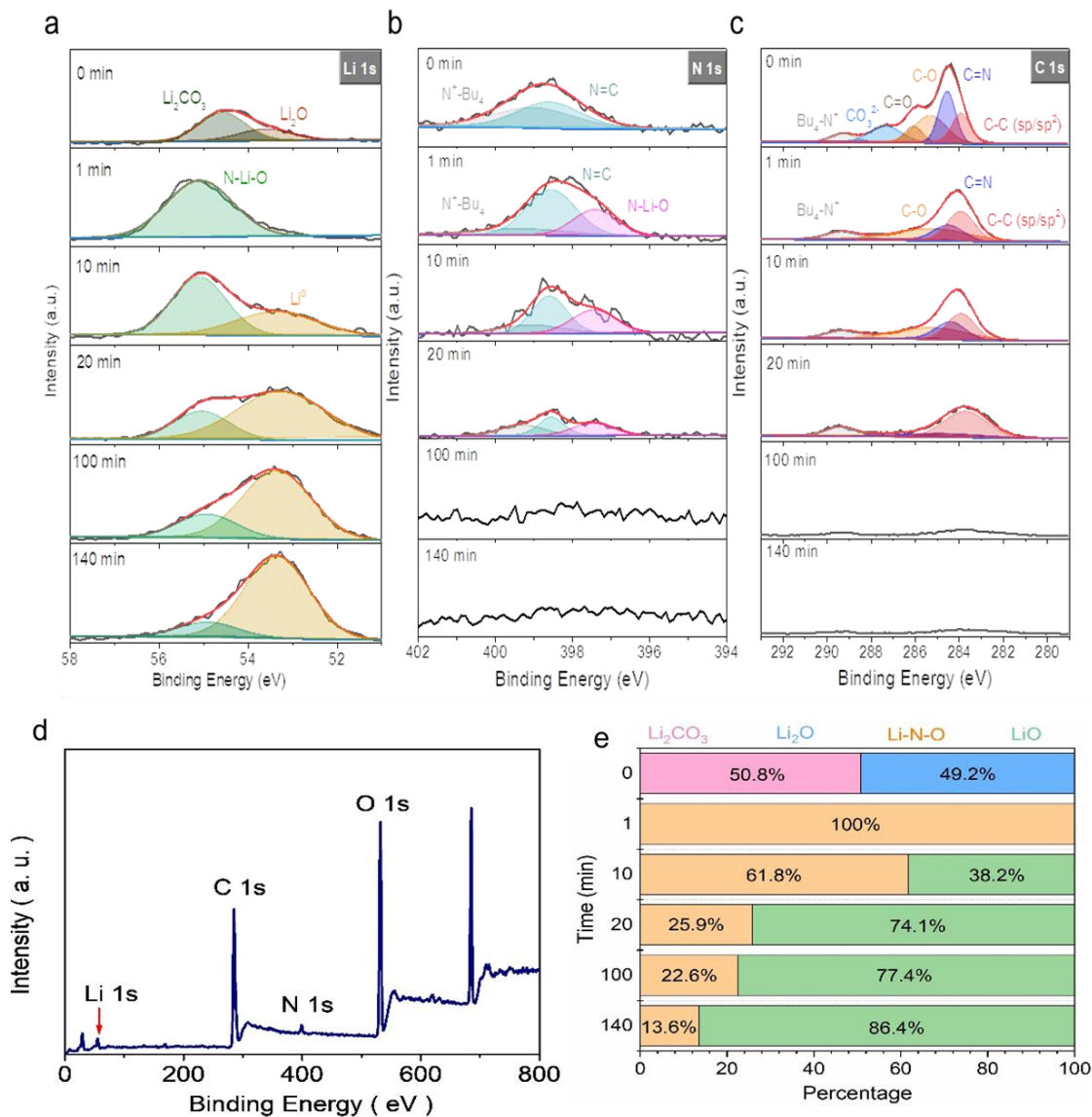
Fig. 3.14 | XPS depth profiles of **a**, Li 1s, **b**, C 1s and **c**, N 1s spectra of PPQ-stabilized Li anode. **d**, Top surface XPS survey spectra of PPQ-stabilized Li anode. **e**, The composition of Li-related species based on Li 1s spectra.

To further investigate chemical structure of the as-prepared artificial SEI layer, X-ray photoelectron spectroscopy (XPS) depth profiling is performed from the top surface of PPQ-stabilized Li to the Li metal surface underneath (**Figure 3.14**). As

shown in **Fig. 3.14a**, in Li 1s spectra, there are small amounts of Li_2CO_3 (~55.6 eV) and Li_2O (~54.6) on the top surface of PPQ-stabilized Li anode (0 min sputtering) due to the inevitable exposure to ambient atmosphere during sample transferring.[157, 173] One peak at ~54.3 eV is observed after 1 min sputtering which can be attributed to the N-Li-O according to the spontaneous chemical reaction of Li metal and PQ monomer, which illustrates the integrated structure of the designed artificial SEI layer and Li metal.[164] Such signal becomes weaker upon sputtering and meanwhile, the Li^0 (~53.6 eV) appears owing to the continuous etching of grafted PPQ layer.[174] The compositional evolution is calculated and exhibited in **Fig. 3.14c**. In N 1s spectra (**Fig. 3.14b**), PPQ-stabilized Li presents the common species of N^+-Bu_4 and N=C at ~399.0 and ~398.5 eV, respectively. After sputtering, the N-Li-O at ~397.4 eV appears which agrees well with the Li 1s results.[173] It is noticed that the N 1s signal almost disappears after 100 min sputtering suggests that the grafted PPQ layer was completely etched. The peaks of Bu_4-N^+ (~290.2 eV), CO_3^{2-} (~288.2 eV), C=O (~287.0 eV), C-O (~286.2 eV), C=N (~285.4 eV) and C-C (sp/sp^2, ~284.8 eV) are observed in C 1s spectra without etching attributing to the redundant PQ, Li_2CO_3 and PPQ (**Fig 3.14c**).[163, 175, 176] The peaks of CO_3^{2-} and C=O disappears after 1 min sputtering. It also exhibits inconspicuous signals after 100 min sputtering according to the consume of PPQ layer.
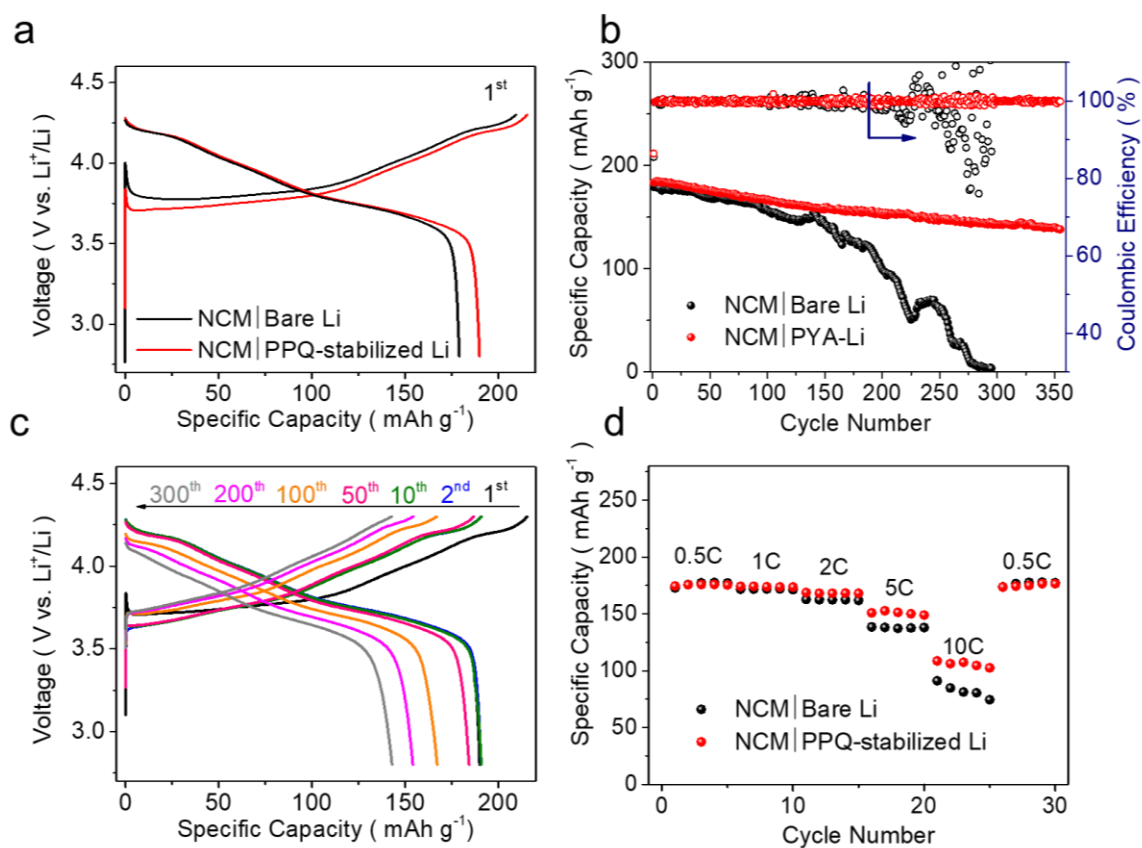
Fig. 3.15 | a, Initial charge-discharge curves of NCM|Bare Li and NCM|PPQ-stabilized Li full cells. **b**, Cycling performance at 0.5 C of NCM|bare Li and NCM|PPQ-stabilized Li full cells. **c**, Charge-discharge curves of NCM|PPQ-stabilized Li full cell at 0.5 C. **d**, Rate performance of NCM|PPQ-stabilized Li full cells at 0.5/1/2/5/10C.

To further demonstrate the merit of the designed artificial SEI layer, full cells with commercial NCM (~2.4 mAh cm^{-2}) as cathode and PPQ protected ultra-thin lithium metal (50 μm) as anode were assembled and tested. **Fig. 3.15a** displays the initial charge-discharge curves of NCM|PPQ-stabilized Li and the control cell NCM|bare Li at 0.5 C (**Fig. 3.15b**). Remarkably, NCM|PPQ-stabilized Li delivers a higher initial capacity of 189.9 mAh g^{-1} than that of NCM|bare Li (179.1 mAh g^{-1}). Meanwhile, the

voltage polarization of NCM|PPQ-stabilized Li is much lower attributing to the improved kinetics. After 300 cycles, there is still 143.0 mAh g^{-1} remained with slightly increased voltage hysteresis, revealing enhanced stability of this full cell. Rate capabilities of NCM|bare Li and NCM|PPQ-stabilized Li were estimated at various current densities. The full cell with bare ultra-thin Li metal as anode shows a rapid degradation within 150 cycles and the capacity drops to almost zero after 270 cycles at 0.5 C (**Fig. 3.15b**). Nevertheless, the protected NCM|PPQ-stabilized Li cell exhibits higher initial specific capacity of 183.6 mAh g^{-1} (2.1 mAh cm^{-2}) and still remains 140.0 mAh g^{-1} (1.6 mAh cm^{-2}) after 350 cycles, implying more stable cycling life. As displayed in **Fig. 3.15d**, NCM|PPQ-stabilized Li exhibits reversible capacities of 177.5, 171.9, 162.4, 138.1 and 82.4 mAh g^{-1} at the C-rate of 0.5, 1, 2, 5 and 10 C, respectively. Moreover, it recovers to 177.4 mAh g^{-1} when the current density is set back to 0.5 C which demonstrates the enhanced kinetics with stable interfacial layer. However, NCM|bare Li presents lower capacities especially at high C rates attributing to the accumulated resistance caused by uneven lithium deposition and non-homogenous SEI layer.

3.4 Conclusions

In summary, we have demonstrated a novel artificial SEI layer uniformly grafted on the lithium metal surface due to the spontaneous reaction between monomer and lithium as well as the subsequent polymerization, forming an integrated PPQ-stabilized Li anode. This protected LMA anode exhibits excellent passivation, homogenous

surface potential distribution and enhanced mechanical strength which effectively prevents the electrolyte decomposition nd suppresses generation of lithium dendrites. The PPQ-stabilized Li|PPQ-stabilized Li symmetric cell presents lower voltage hysteresis and stabilized cycling life up to 1800 h at 0.5 mA cm^{-2}, capacity of 1 mAh cm^{-2}. Moreover, the modified LMA enables an excellent cycling performance of NCM|PPQ-stabilized Li full cells with a high initial areal capacity of 2.1 mAh cm^{-2} and stable cycling life with retention of ~76% after 350 cycles. This *in-situ* polymerized polymer with uniform surface potential provide a new design strategy to stabilize LMA which is also applicable for other alkaline metal anode such as Na and Zn anodes.

Chapter 4. Electrolyte Interphase Built from Anionic Covalent Organic Frameworks for Lithium Dendrite Suppression

4.1 Introduction

The burgeoning markets of electric vehicles and portable electronics call for lithium-ion battery (LIB) to be much safer and energy denser.[177] As the state-of-the-art LIB approaches its theoretical maximum, reviving lithium-metal (Li) battery becomes an inevitable necessity owing to the high capacity (3861 mAh g^{-1}) and low potential (-3.04 V versus standard hydrogen electrode) of metallic Li anode.[178] Despite these promises, the practical exploitation of Li anode confronts formidable challenges, the greatest of which are safety and poor cyclability that stem from the uncontrollable dendritic Li growth and unstable solid electrolyte interphase (SEI) formation at Li-electrolyte interface.[179]

To suppress the proliferation of dendritic Li, interfacial engineering approaches towards constructing stable SEI have been extensively explored.[149, 180, 181] For examples, fluorinated compounds, such as fluoroethylene carbonate (FEC), serve as effective electrolyte additives for passivating Li metal with robust LiF-rich SEI.[144] By virtue of its reactive nature, chemical pretreatments of Li generate artificial SEI that allow permeation of Li-ions and possess high mechanical strength.[182] With reduced solvent contents, high-concentration electrolytes (e.g., 4M LiFSI) form more affinitive SEI than that in routine electrolyte (1 M) owing to the uniquely solvated Li-ions.[183] These

attempts aim to regulate the compositions, structures and mechanical properties of SEI that passivate the highly reactive Li anode.

The above strategies focus on stabilizing interface between reacting Li and electrolyte. Nevertheless, the Li deposition is a coupled reaction-diffusion process and the diffusion limitation is less researched. According to Sand's theory, the cation depletion during electrodeposition breaks electrical neutrality and builds up space charge at the plated electrode surface, thereby triggering parasitic reactions and ramified metal deposition. [184, 185] The occurrence of Li-ion deficiency is largely attributable to the poor transport efficiency (Li-ion transference number, t_{Li}^+) of liquid electrolyte, that is, a low portion of total ion-conduction carried by the effective Li-ions.[85] To circumvent this issue, coating Li anode with electrolyte-based interphases that uniformly and exclusively conduct Li-ions, such as single-ion solid polymer electrolytes (e.g., lithiated Nafion[186]) and inorganic solid electrolytes (e.g., Li_3PS_4[187-193]), were demonstrated with dendrite-free Li deposition. Despite that single-ion conduction is achieved, conductivities of those solid electrolyte interphases ($< 10^{-3}$ S cm^{-1}) are typically inferior than liquid electrolytes, thereby leading to insufficient Li^+ conductance given thick interphase and/or high drain current.
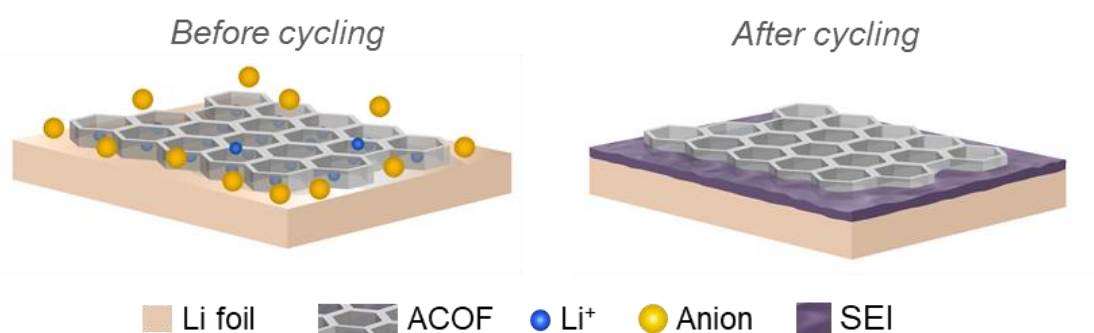
Fig. 4.1 | Schematic illustration showing uniform Li^+/Li electrodeposition on ACOF-coated Li electrode.

In this work, an anionic electrolyte interphase was built on Li anode by a thin layer of anionic covalent organic frameworks (COF) (denoted as ACOF), where the ACOF crystalline as microporous 2D nanosheets that composed of anionic building units and charge-balancing cations (Li^+). Infusing liquid electrolyte into ACOF simultaneously confers superior ionic conduction ($> 10^{-3}$ S cm^{-1}) and near-unity t_{Li^+} (0.82) at the interphase, which stem from multiple ion-modulations by the anionic frameworks. First, the Li^+-affinitive moieties in ACOF facilitate enrichment of Li salt from the electrolyte (**Fig. 4.1**); Second, the layered anionic frameworks favor rapid translocation of Li^+ and thereby eliminate electrolyte depletion in vicinity of Li anode. Third, the adsorption of Li^+ by ACOF leads to localization and decomposition of associated anions, forming native beneficial SEI and dendrite-free morphology. Overall, we introduce a new category of electrolyte interphase for coating Li anode and inhibiting dendrite formation. Such interphase is built by microporous anionic COF that offers preferential adsorption and permeation of Li-ions, which endow high conductivity comparable to parent liquid electrolyte, as well as high selectivity rivalling solid-state electrolytes.

4.2 Experiment Methods

4.2.1 Synthesis of ACOF

Scheme 4.1 Synthesis of 2,3,6,7-tetramethoxy-9,10-dimethylanthracene (TMDMA).

A mixture of 1,2-dimethoxybenzene (32.6 ml, 0.218 mol) in sulfuric acid (70% v/v in H_2O) below -10 °C, acetaldehyde (24 ml, 0.428 mol) was slowly added dropwise for 2.5 h. After stirred for 2h at room temperature, the mixture was poured into 300 ml mixed solvent of ethanol/water (1:1, v/v). The precipitate was filtered and washed with ethanol (100 ml), water (100 mL) and acetone (200 ml). The obtained solid was dissolved in acetone (300 mL) and refluxed for 30 min, then filtered and dried for 2 h in vacuum at 120 °C, ultimately giving a grey solid 25.0 g (yield : 70%) (**Scheme 4.1**).
^{1}H NMR (400 MHz, Chloroform-*d*) δ 7.40 (s, 4H), 4.08 (s, 12H), 2.94 (s, 6H) (**Fig.4.2**).
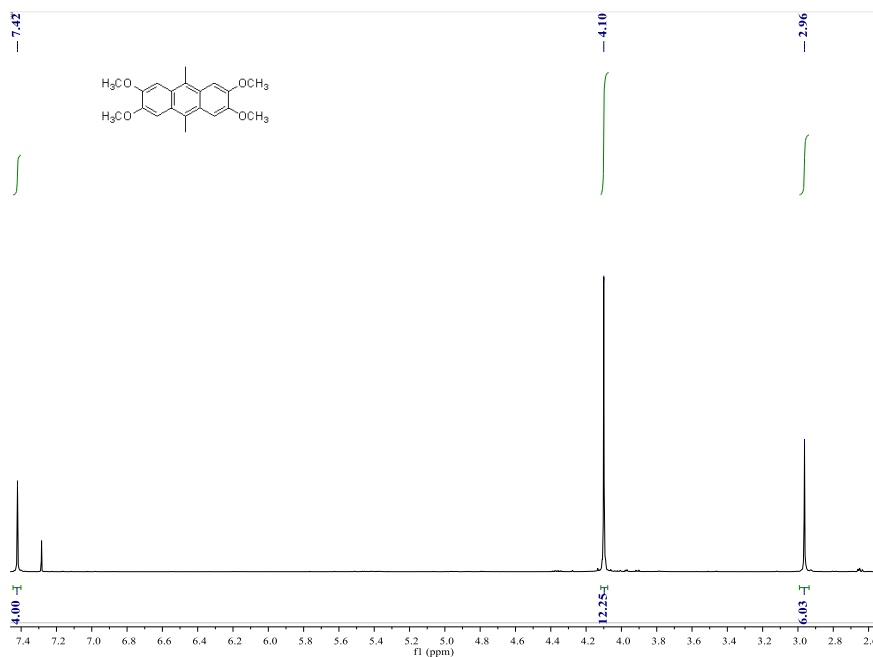
Figure 4.2 | ^{1}H NMR spectrum of THDMA (400 MHz, DMSO-*d6*, 300 K).

9,10-dimethylanthracene-2,3,6,7-tetraol（THDMA）[195]
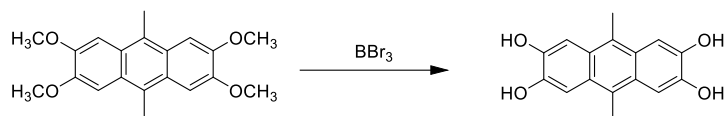
Scheme 4.2 Synthesis of 9,10-dimethylanthracene-2,3,6,7-tetraol (TMDMA).

To a mixture of TMDMA (8 g, 24.5 mmol) in anhydrous dichloromethane (350 mL) at room temperature under inert atmosphere, BBr$_3$ (7.0 ml, 73.5 mmol, 3.0 eq) was added dropwise. The mixture was stirred for 2 h and yellow solid appeared. The reaction solution was filtered, and solid was washed with ice/water, giving a yellow powder. The powder in methanol/dichloromethane (100 ml, 1:1, v/v) was refluxed for 1h, then filtered and washed with methanol (100 ml), and dried at 60 °C overnight, ultimately resulting a yellow powder 5.6 g (yield: 84%) (**Scheme 4.2**).

^{1}H NMR (400 MHz, DMSO-d_6) δ 9.33 (s, 4H), 7.25 (s, 4H), 2.61 (s, 6H); ^{13}C NMR (151 MHz, DMSO-d_6) δ 145.91, 125.26, 120.99, 105.59, 14.19; HRMS(APCI+): calculated m/z for [M]+ 270.0892, found: 270.0930 (**Fig.4.3**).

a

—9.235

—7.145

—2.500

4.02

4.00

5.98

Chemical Shift (ppm)

b

—145.906

—125.257
—120.990

—105.587

—14.188

Chemical Shift (ppm)

c

270.09302

269.08498

271.09609

272.09862   273.14018

122
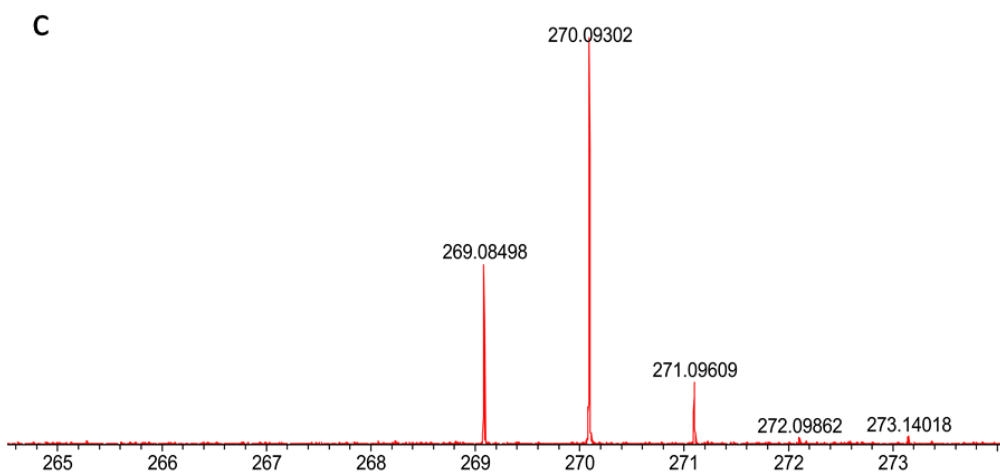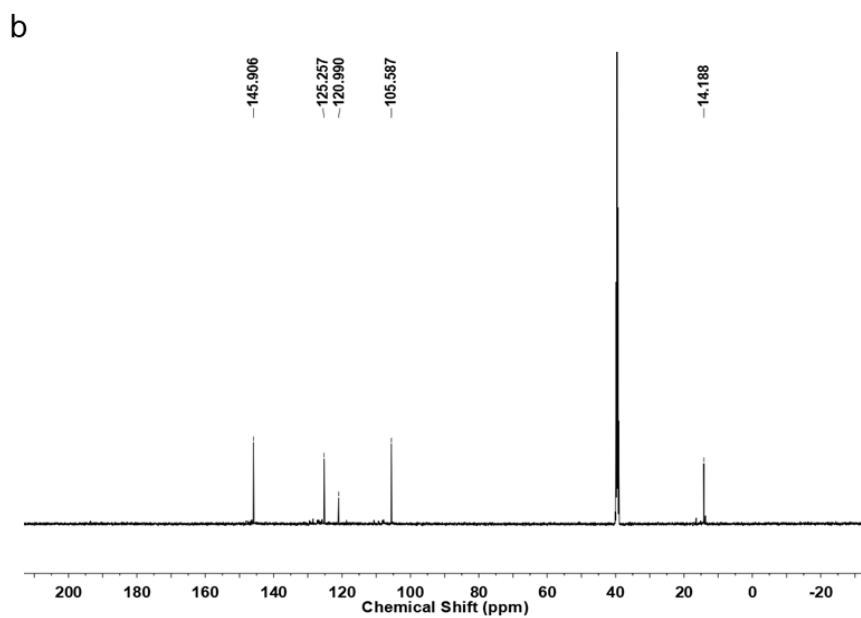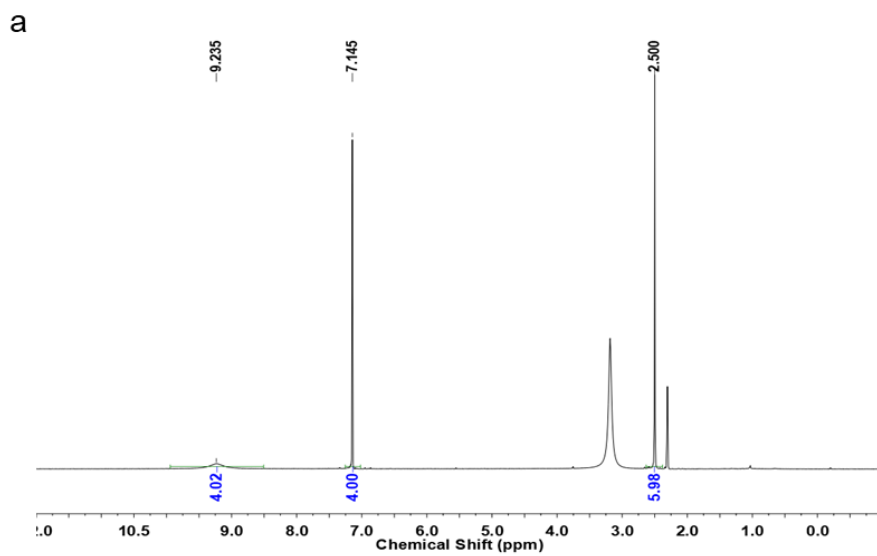
Figure 4.3 | a, ¹H NMR spectrum of THDMA (400 MHz, DMSO-d_6, 300 K). **b**, ¹³C NMR spectrum of THDMA (151 MHz, DMSO-d_6, 300 K).**c**, HRMS(APCI+) of THDMA.

Synthesis of ACOF.
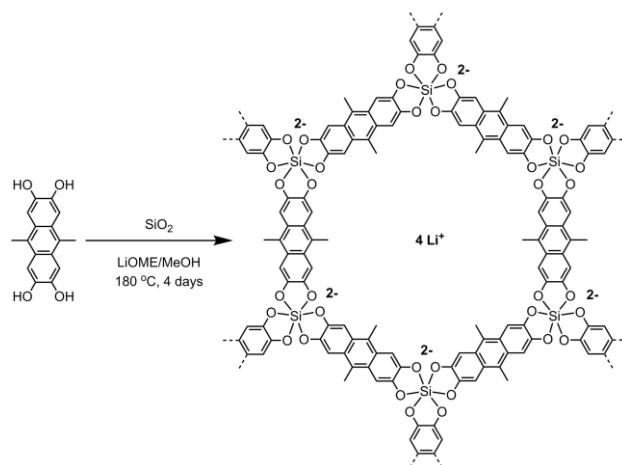
Scheme 4.3 Synthesis route of ACOF.

ACOF nanoparticles were solvothermally synthesized according to the previous reported method (**Scheme 4.3**). A mixture of 200mg 9,10-Dimethyl-2,3,6,7-Tetrahydroxyanthracene (0.74 mmol), 1.1 mL of a 1.0 M lithium methoxide solution in anhydrous methanol (1.1 mmol) and 2 mL of a 0.25 M tetramethyl orthosilicate solution in anhydrous methanol (0.5 mmol) were dissolved in 19 mL of anhydrous methanol in a Teflon liner and stir for 5 min. The Teflon liner was sealed in an autoclave and heated in an oven at 180 ℃ for 4 days. Brownish powder which was collected by were isolated by centrifugation, washed with anhydrous methanol and anhydrous acetone for three times and dried in a vacuum oven at 60 ℃ overnight.

4.2.2 *Material characterization*

The crystal structure was characterized by X-ray diffraction (Rigaku powder X-ray diffractometer (XRD) using Kα radiation (λ = 1.54 Å). The morphology was observed by field scanning electron microscopy (FESEM, HITACHI, S-4800) with energy dispersive x-ray spectroscopy (EDS) and transmission electron microscopy (FEI T12 Quick CryoEM and CryoET TEM). Solution-state ^{1}H NMR, ^{13}C NMR spectra were obtained from a Bruker Avance (III) (400 MHz) spectrometer at Shanghai Normal University. Solid-state NMR experiments were conducted on Bruker Avance III HD 400 (9.4 T) spectrometers using a 3.2 mm magic-angle spinning probes. The lithium diffusion coefficient D_{Li}^+ was measured by pulsed-field-gradient nuclear magnetic resonance (PFG NMR) method, which was recorded on the Bruker Avance 600 MHz spectrometer with a Z-gradient direct detection broad-band probe. The diffusion constant was estimated from the echo attenuation plot by varying gradient strengths with a fixed value of diffusion delays (Δ = 20 ms) and gradient duration (δ = 1 ms). The surface topographies of the exfoliated nanosheets deposited on Si wafers were characterized employing a Hitachi AFM5200S scanning probe microscope. X-ray photoelectron spectroscopy (XPS) measurements were performed on an AXIS Ultra DLD instrument. The samples were prepared in glovebox before quickly being transferred to a high-vacuum chamber. Infrared spectra experiments were performed in a transmission mode on a Jasco 420 Fourier transform infrared (FT-IR) spectrophotometer. N_2 adsorption/desorption measurements were conducted using a

Micromeritics ASAP 2020 system at 77 K. Prior to the measurement, the ACOF sample was degassed at 180 °C for 12 h. The Brunauer-Emmett-Teller (BET) method was employed to determine the specific surface area (SBET) and the Barrett-Joyner-Halenda (BJH) model was applied to calculate the pore volume (VP) and pore diameter (DP). The zeta potential was measured using a Malvern Zetasizer ZS.

4.2.3 Computational details

The structure of $(SiLi_3C_{32}O_8H_{20})_4$ was constructed based on ACOF, whose stable configuration was determined by geometry optimization using a $1 \times 1 \times 2$ supercell model with 196 atoms. The calculations of Li adsorption and diffusion were performed by Dmol^3 program.[196, 197] The exchange-correlation energy was calculated by combining generalized gradient approximation with Perdew-Burke-Ernzerhof functional (GGA-PBE) and the double numerical polarization basis set.[198] Meanwhile, to correctly describe the interaction between Li and ACOF, the dispersion correction was considered based on the semi-empirical Tkatchenko-Scheffler (TS) scheme.[199] The core-electron of the model was treated using DFT semi-core pseudopotential. Brillouin zone was sampled by Monkhorst-Pack grid as Γ-point for all systems.[200] As to Li adsorption process in ACOF, the adsorption energy E_{ads} was calculated by the following equation:

$$E_{ads} = E_{ACOF+Li} - E_{ACOF} - E_{Li}$$

where $E_{ACOF+Li}$, E_{ACOF} and E_{Li} represent the energy of the adsorption complex, ACOF model and Li ion, respectively.

For the diffusion process of Li ion, the diffusion pathways were analyzed by linear and quadratic synchronous transit (LST/QST) methods in combination with the conjugated gradient (CG) refinement.[201]

To further reveal the origin of the adsorption interaction, electron difference density for Li^+ adsorption by means of the reduced density gradient was carried out using Multiwfn 3.7.[202] Corresponding wave function of the selected structural unit was obtained at M06-2X/6-31+G(d,p)[203] using Gaussian 09 D0.[204]

4.2.4 Electrochemical characterizations

The measurement of ionic conductivity was carried out in a home-made electrolyte cell, where two identical Titanium plates (1×1 cm^{-2}) served as blocking electrodes. The ionic resistance was estimated by the extrapolated interception of the Nyquist plots with the real axis. The determination of t_{Li}^+ was performed through the combination of EIS technique and potentiostatic polarization. The symmetric Li|Li cells were polarized by a constant voltage bias of 20 mV (ΔV) for 1 hour, during which the initial current (I_0) was monitored until reaching the steady-state current (I_{ss}), and the interfacial resistance t_{Li}^+ thereby could be calculated with the following expression: $t_{Li}^+ = I_{ss}(\Delta V/I_0 R_0)/(I_0(\Delta V/I_{ss} R_{ss}))$. The CV tests (Biologic VMP3) were conducted in SS|Li cells at scan rate of 1 mV s^{-1} between -0.2 V and 5 V (vs. Li/Li^+).

4.2.5 Battery tests

LiCoO2 cathode (LCO, LC95A from Hunan Shanshan) with a areal capacity of ~ 1.7 and ~ 4 mAh cm^{-2} was cut into 10-mm-diameter disks and used to assemble protype

Li|LCO full cells. Thin Li foils with thickness of 50 μm were used with 25 μm separator (Celgard 2500). The voltage window for the full cells with LCO cathodes was set to 3.0 - 4.5 V. All electrochemical tests were conducted at ambient temperature (25 °C) and minor temperature fluctuation may have occurred due to facility management.

4.3 Results and discussions
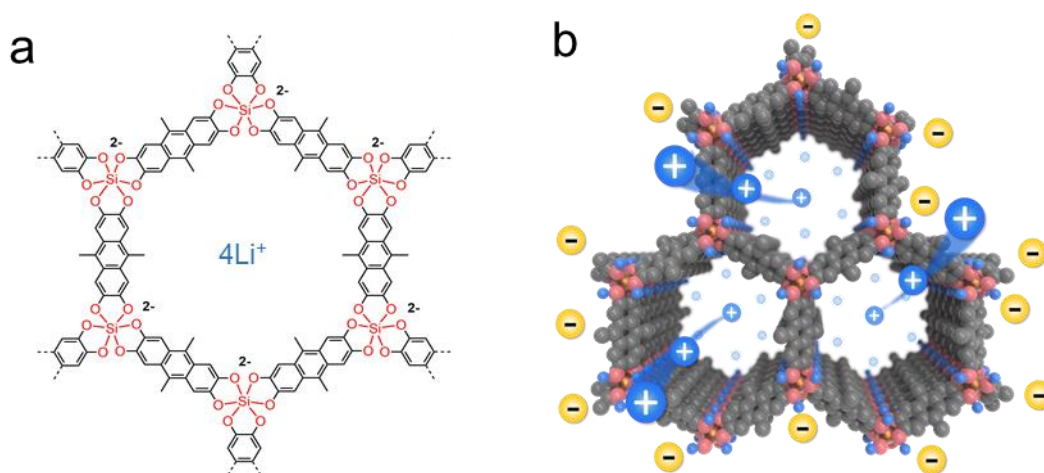
Fig. 4.4 | (a) Structural representation of ACOF. (b) A drawing depicting the selective ion transport of electrolyte in ACOF (blue: Li, red: Si, grey: C, gold: O, yellow: anion).

As illustrated in **Fig. 4.4a**, the ACOF employ well-defined silicate COF, which is constructed by hexacoordinate silicon centres (SiO_6) and anthracene linkers (9,10-dimethyl-2,3,6,7-tetrahydroxyanthracene, DMTHA).[205] Their covalent connections infinitely augment to a 2D hexagonal network with large microporosity, where the octahedral bianionic SiO_6 nodes are balanced with extra-framework cations and uniformly distributed over the honeycomb sublattice. In such design, the populated negative charges surrounding microporous frameworks enable exclusive Li-ion

conduction and screen the passage of anions from liquid electrolyte (**Fig. 4.4b**). Additioanlly, the layered structure could provide shortened distance that eases translocation of Li-ions.
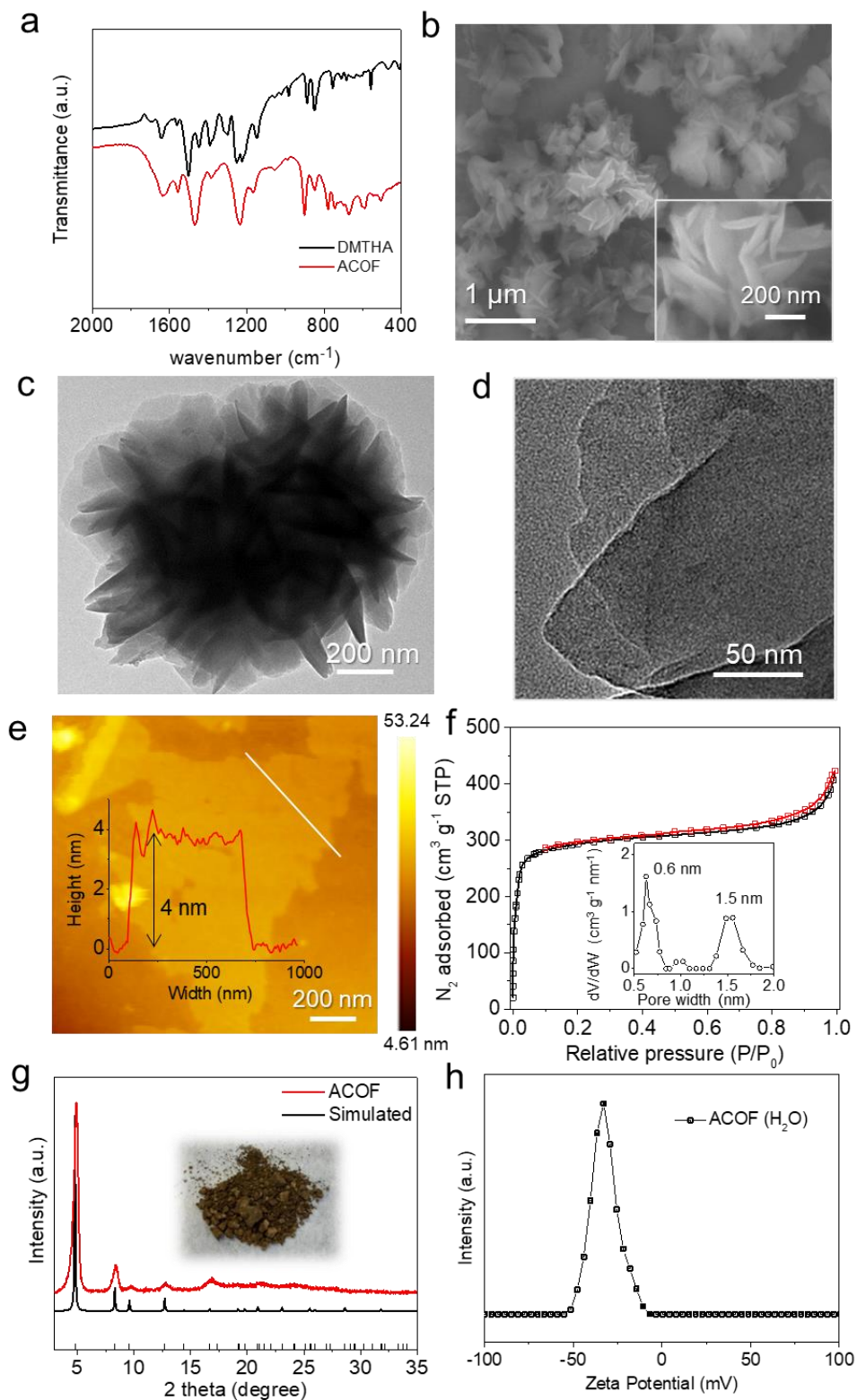
Fig. 4.5 | Imaging and characterization of ACOF particles: **a**, SEM images, **b-c** TEM

images, **d**, AFM micrograph and height distribution measured along the white line. **e,**

N$_2$ adsorption/desorption isotherms of ACOF particles (inset: micropore size distribution). **f**, FT-IR spectrum of ACOF (bottom) and 9,10-dimethyl-2,3,6,7-tetrahydroxyanthracene (DMTHA) (top). A new band at 665 cm^{-1} (dashed line) assigned to the Si-O stretching mode implies the building blocks are linked to a hexacoordinate silicate compound. **g**, XRD patterns of ACOF and a simulated ACOF pattern is plotted at the bottom, and inset is a photograph of as-synthesized ACOF powder. **h**, Zeta potential of ACOF in aqueous solution.

The ACOF were synthesized according to the well-reported literature. The infrared (IR) spectra of as-synthesized ACOF suggests formation of connecting networks by a detected Si–O bond (**Fig. 4.5a**).[206] As imaged by SEM (**Fig. 4.5b**),TEM (**Figs. 4.5c-d**) and AFM (**Fig. 4.5e**), the ACOF particles show morphology of spherical assemblies, which are composed by nanoplatelets with approximate thickness of 4 nm. The micropore structure was verified by N$_2$ adsorption isotherms (**Fig. 4.5f**), where the ACOF exhibit a high Brunauer–Emmett–Teller (BET) surface area of 957 m^2 g^{-1}, and a huge adsorption at low relative pressure indicative of prevailing microporosity. The corresponding non-local density functional theory (NLDFT) model (inset of **Fig. 4.5f**) reveals well-defined pore sizes centred at 0.6 and 1.5 nm, which originate from the hexagonal pore apertures. The crystallinity of the frameworks was determined by powder x-ray diffraction (PXRD) (**Fig. 4.5g**). The diffraction pattern displays intense characteristic peaks, which are in accordance with reported crystallographic data of the silicate organic frameworks. The negative charges carried by ACOF particles were

confirmed by zeta potentials of –32 mV in aqueous medium (**Fig. 4.5h**).
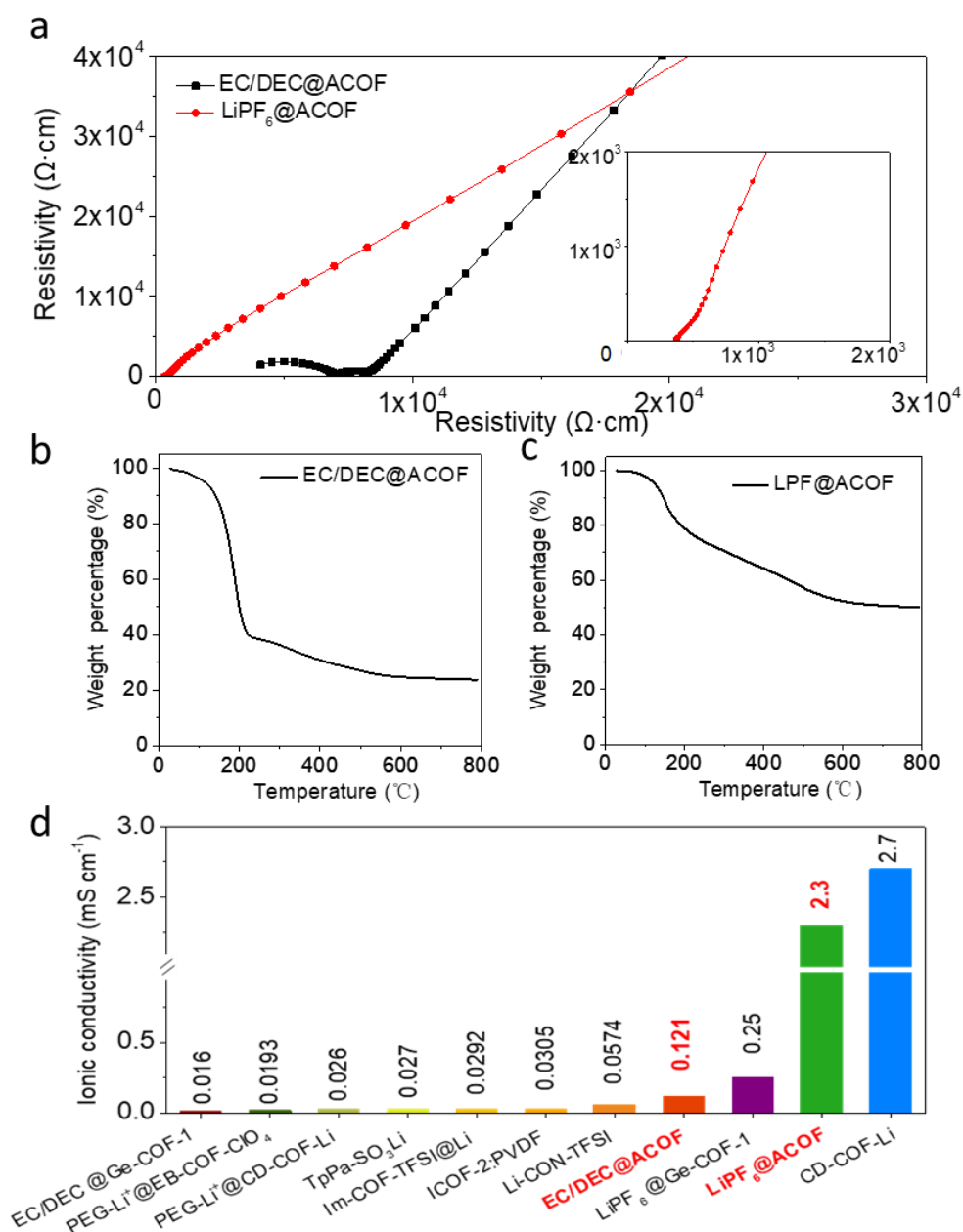
Fig. 4.6 | a, Nyquist plots of resistivity of EC/DEC@ACOF and LiPF$_6$@ACOF. TGA curves for measuring the solvent content of (**b**) EC/DEC@ACOF and (**c**) LiPF$_6$@ACOF. **d**, Comparison of ionic conductivity between ACOF-based electrolyte and other COF-based electrolytes.

Table 4.1 Comparison of ionic conductivity in ACOF-based electrolytes with literature-reported COF-based materials.

Materials	Skeletal charge	Pore size (nm)	Foreign salt	Plastizer	Ambient conductivity (S cm^{-1})	t_{Li^+}	Reference/ Note
Im-COF-TFSI@Li	Cationic (imidazolium)	5.57	LiTFSI	-	2.92×10^{-5} (30 °C)	0.62	[207]
Li-CON-TFSI	Cationic	-	LiTFSI	-	5.74×10^{-5} (30 °C)	0.61	[208]
EC/DEC@Ge-COF-1	Anionic (GeO$_6^{2-}$)	1.5	-	20 wt-% EC/DEC (v/v = 1:1)	1.6×10^{-5}	-	[209]
LiPF$_6$@ Ge-COF-1				1 M LiPF$_6$ in EC/DEC (v/v = 1:1)	2.5×10^{-4}	0.67	
PEG-Li$^+$@EB-COF-ClO$_4$	Cationic	2	LiClO$_4$	PEG	1.93×10^{-5}	0.6	[210]
PEG-Li$^+$@CD-	Anionic	0.8	LiClO$_4$	PEG	2.60×10^{-5}	0.2	

COF-Li						
ICOF-2:PVDF	Anionic (spiroborate)	2.2	-	55 wt-% PC	3.05×10^{-5}	0.8	[211]
TpPa-SO$_3$Li	Anionic (sulfonate)	1.2	-	-	2.7×10^{-5}	0.9	[212]
CD-COF-Li	Anionic (spiroborate)	0.6	1 M LiPF$_6$ in EC/DMC (v/v = 1:1)	2.7×10^{-3}	-	[213]
EC/DEC@ACOF	Anionic (SiO$_6$)	0.6/1.5	-	EC/DEC (v/v = 1:1)	1.2×10^{-4}	0.82	**This work**
LiPF$_6$@ACOF				1 M LiPF$_6$ in EC/DEC (v/v = 1:1)	2.3×10^{-3}		

In light of the anionic nature, ACOF balanced by extra-framework Li$^+$ can offer intrinsic conductivity upon dissociation by organic solvents.[214] Meanwhile, analogous to other porous scaffolds, infiltrating electrolyte in ACOF produces solid-like electrolyte that inherits conductivity from the guest ions.[111, 215, 216] To validate these two points, the ACOF particles were soaked in pure solvents or electrolyte, and subsequently densified to electrolyte pellets, where the solvents are mixed ethylene

carbonate (EC)/diethyl carbonate (DEC) (1:1 by volume) and electrolyte is 1 M LiPF$_6$ in the EC/DEC mixture. The ionic conductivity of the pellets was measured using electrochemical impedance spectroscopy (EIS). The resulting Nyquist plots display semicircles and inclined lines, of which the interceptions are approximated for ionic resistance (**Fig. 4.5a**). The corresponding conductivities of the pellets soaked with solvents (denoted as EC/DEC@ACOF) and electrolyte (denoted as LiPF$_6$@ACOF) are calculated to be 0.12 and 2.3 mS cm^{-1}, respectively. And the residual solvent in the frameworks were measured by TGA. As shown in **Figs. 5.5b-c**, the solvent content for EC/DEC@ACOF and LiPF$_6$@ACOF) was approximately 60% and 50%, respectively. To the best of our knowledge, the ionic conductivities of ACOF-based electrolytes surpass majority of reported COF-based electrolytes, as summarized in **Table 5.1**and **Fig. 4.5d**.[207-213] Notably, the conductivity of LiPF$_6$@ACOF (2.3 mS cm^{-1}) is of the same magnitude as parent liquid electrolyte (8.5 mS cm^{-1}), hinting highly mobile ions enriched in ACOF.
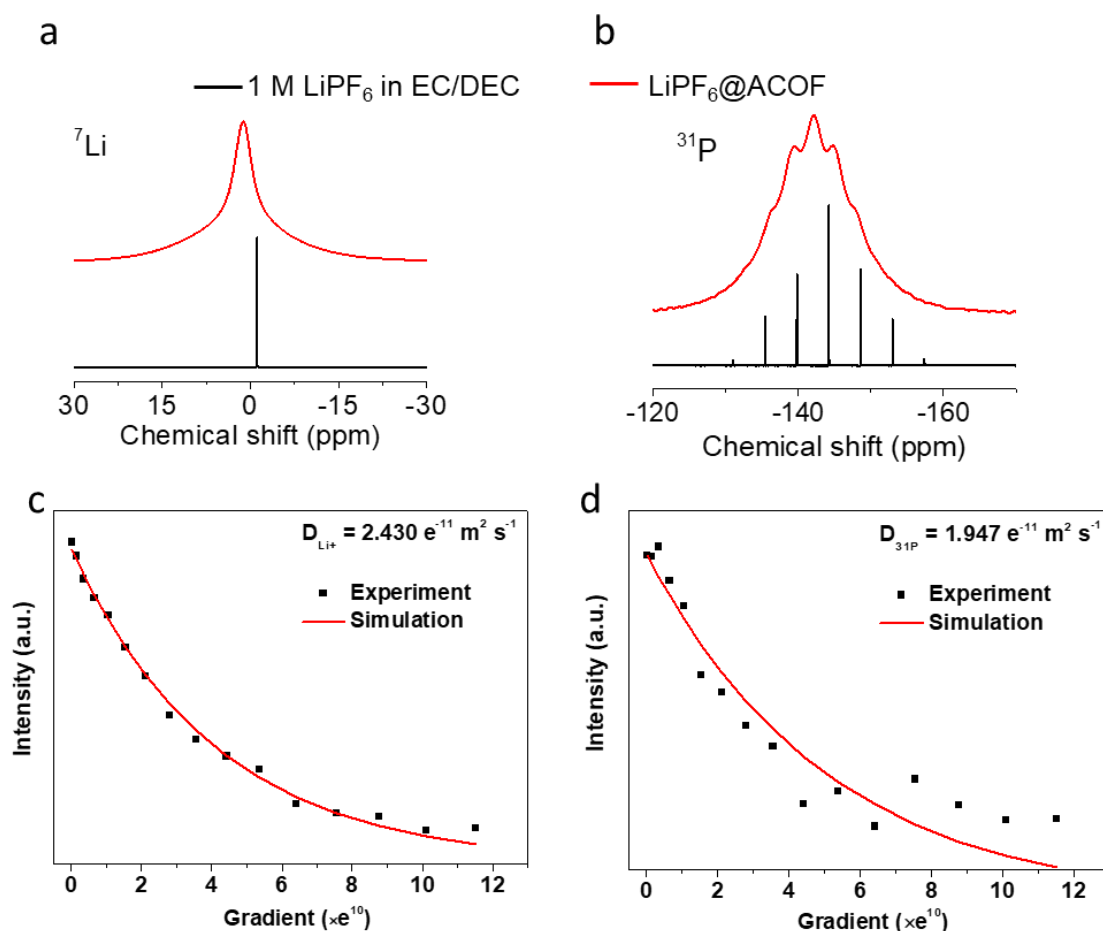
Fig. 4.7 | a, ^{7}Li and **b,** ^{31}P MAS NMR spectra of LiPF$_6$@ACOF respectively compared with ^{7}Li and ^{31}P NMR of liquid electrolyte (1 M LiPF$_6$ in EC/DEC).**c,** ^{7}Li diffusion and **d,** ^{31}Pcoefficient of LiPF$_6$@ACOF obtained from PFG-NMR.

To probe the influence of ACOF on ion transport, the LiPF$_6$@ACOF was examined by magic-angle spinning (MAS) solid-state nuclear magnetic resonance (SSNMR) spectroscopy. In comparison with their liquid counterparts, both ^{7}Li and ^{31}P spectra of LiPF$_6$@ACOF manifest downfield shift and line-broadening, which originate from the strong electron-withdrawing effect and local nanoconfinement by ACOF, respectively (**Figs. 4.7a-b**).[217] The Li$^+$ diffusion kinetic obtained by pulsed-field-gradient nuclear

magnetic resonance (PFG-NMR) reveals a diffusion coefficient (D_{Li}^+) of 2.43×10^{-11} $m^2 \, s^{-1}$ (**Fig. 4.7c**), which is markedly faster than the best-known solid electrolytes and even comparable to EC-based liquid electrolytes.[218] And the diffusion coefficient for P is $1.95 \times 10^{-11} \, m^2 \, s^{-1}$ (**Fig. 4.7d**)The finding proves extremely high mobility of Li-ions in the matrix of ACOF.
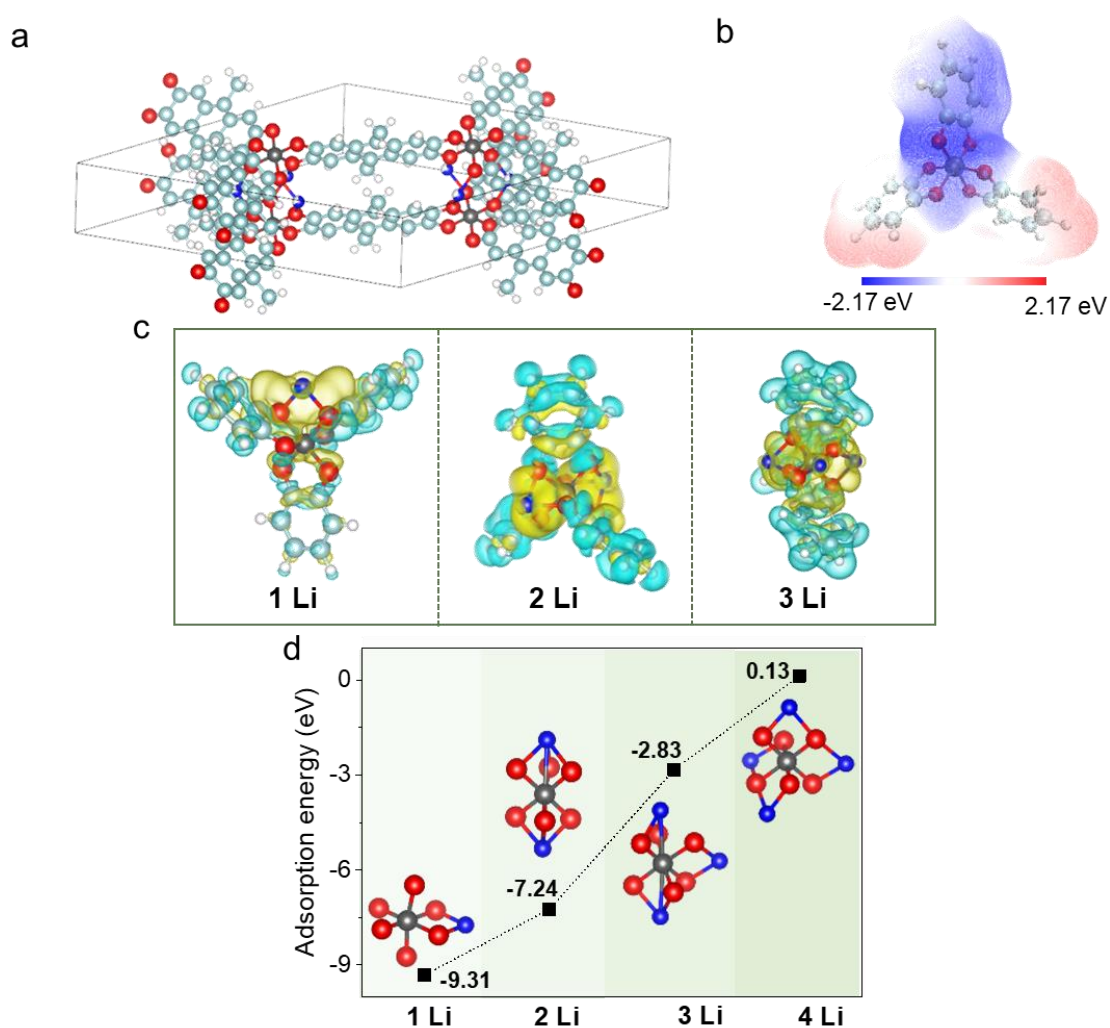
Figure 4.8 | Analyses of Li-ion adsorption and diffusion in ACOF. a, The structure of $(SiLi_3C_{32}O_8H_{20})_4$ was constructed based on ACOF (grey: Si, red: O, turquoise blue: C, white: H). **b**, Electrostatic potential mapping of truncated ACOF. **c**, Electron

difference density isosurface map for Li-ion adsorption over aromatic surface. The yellow and cyan isosurfaces ($\Delta\rho$ of +0.01 to -0.01 a.u., respectively) represent the region in which electron density increases and decreases after Li-ion adsorption, respectively. $\Delta\rho$ is the differences of electron density before and after adsorption; (royal blue: Li) **d**, Optimized configurations and corresponding adsorption energies of one to four Li ions in ACOF.

Density functional theory (DFT) calculations were performed to further understand Li$^+$ adsorption and diffusion behaviors in ACOF. The structure of $(SiLi_3C_{32}O_8H_{20})_4$ was constructed based on ACOF is shown in **Fig. 4.8a**. **Fig. 4.8b** illustrates the electrostatic potential mapping of the selected structural unit from which the oxygen atoms (SiO_6) exhibit the most negative electrostatic potential, indicating that the region owns strong affinity for positively charged Li-ion. The structural configurations for adsorbing Li ions were further calculated and optimized. The electron difference density isosurface map (**Fig. 4.8c**) and adsorption energy (**Fig. 4.8d**) collectively verify that the oxygen atoms around a Si atom can chemisorb three Li ions. In this regard, besides those two Li ions associated with framework, one additional Li$^+$ from electrolyte can be adsorbed by octahedral SiO_6 nodes, leading up to three Li ions per structural unit.
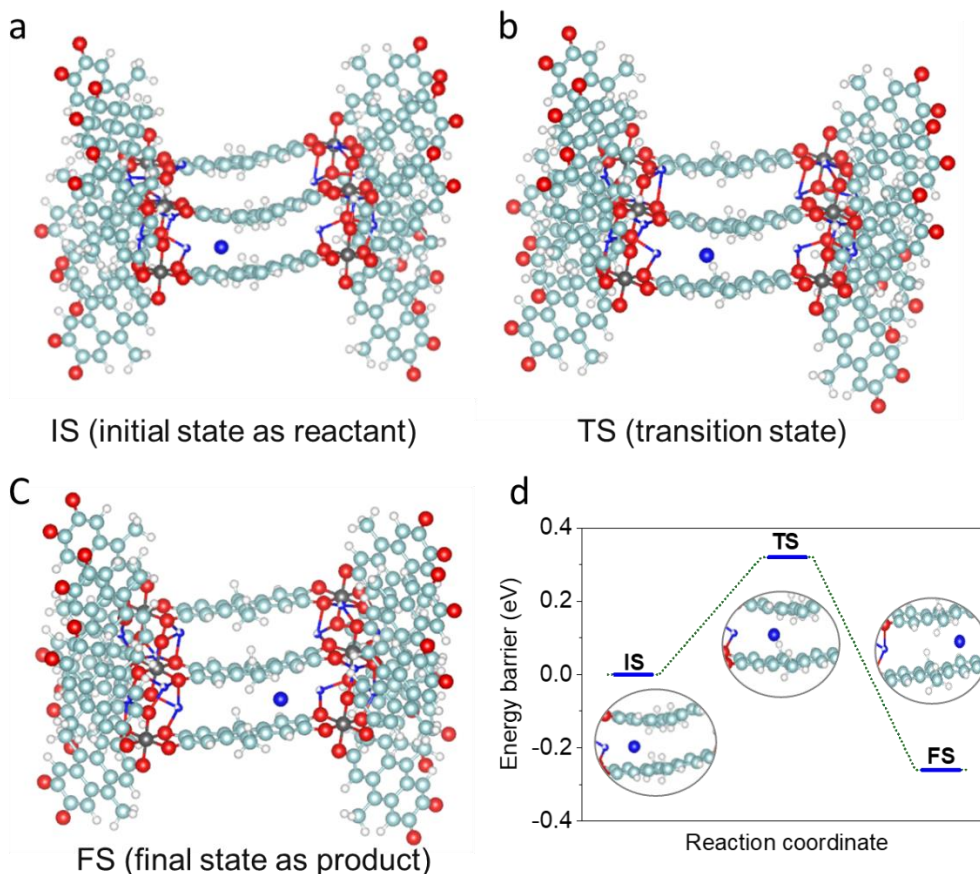
Fig. 4.9 | Potential energy files for Li$^+$ diffusion in ACOF. Circle parts are the structures of **a**, IS: initial state as reactant; **b**, TS: transition state; **c**, FS: final state as product for Li diffusion in ACOF.

During Li$^+$ deposition on Li metal, the distribution of adsorbed Li-ions was governed by diffusion property in ACOF (**Figs. 4.9a-c**). By virtue of the layered structure, the migration barrier along planar aromatic rings in ACOF (0.32 eV) is lower than that on Li crystal plane, suggesting that the adsorbed Li ions prefer uniform distribution in ACOF rather than accumulating at Li surface (**Fig. 4.9d**).[219] Taken together with experimental results, the computational studies suggest that the high conductivity of LiPF$_6$@ACOF could be interpreted by the enriched and mobile Li ions

in ACOF. Considering the lower migration barrier relative to Li anode, the rapid Li^+

translocation in ACOF can also suppress buildup of Li^+ aggregates and potential

dendrite formation.
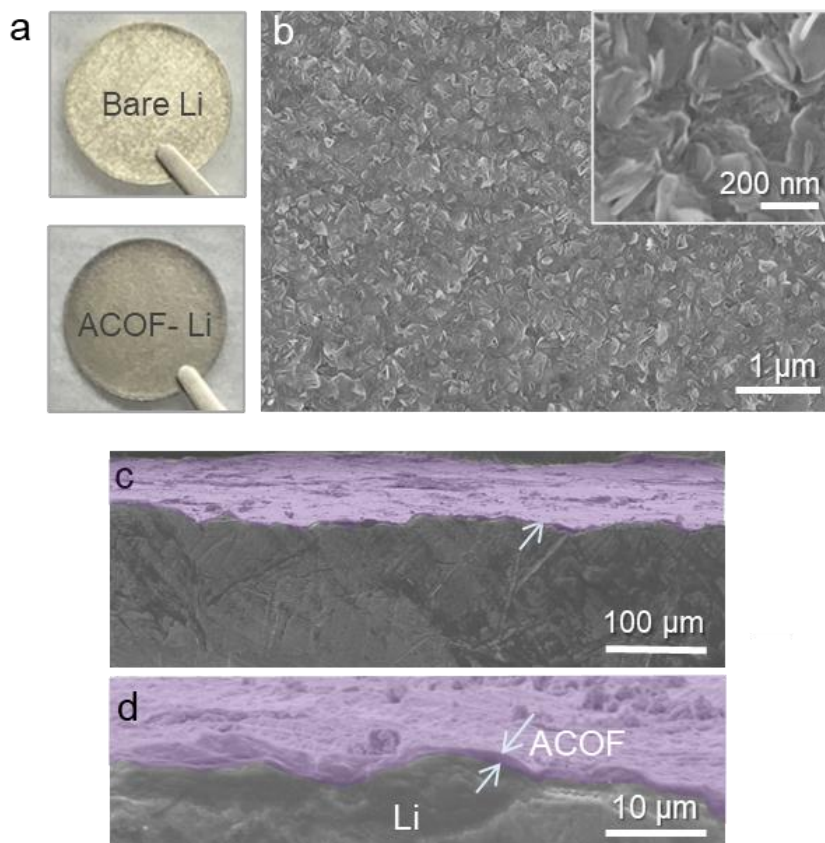
Fig. 4.10 | a, Photographs showing bare Li and ACOF-coated Li disks. SEM images of

ACOF-coated Li in **b**, top-down, and (**c-d**) side views (coating layer is colored on basis

of imaging contrast).

The ACOF layer was integrated on Li anode by a facile drop-coating approach. As

shown in **Fig. 4.10a**, bare Li was coated with suspension droplets containing ACOF

particles, yielding ACOF-coated Li after evaporation of dispersion solvent. As

evidenced by SEM images (**Figs. 4.10b-d**), the fabricated coating layer that tightly

adheres to the Li surface displays uniform flake-like morphology and thin thickness of

1 μm.
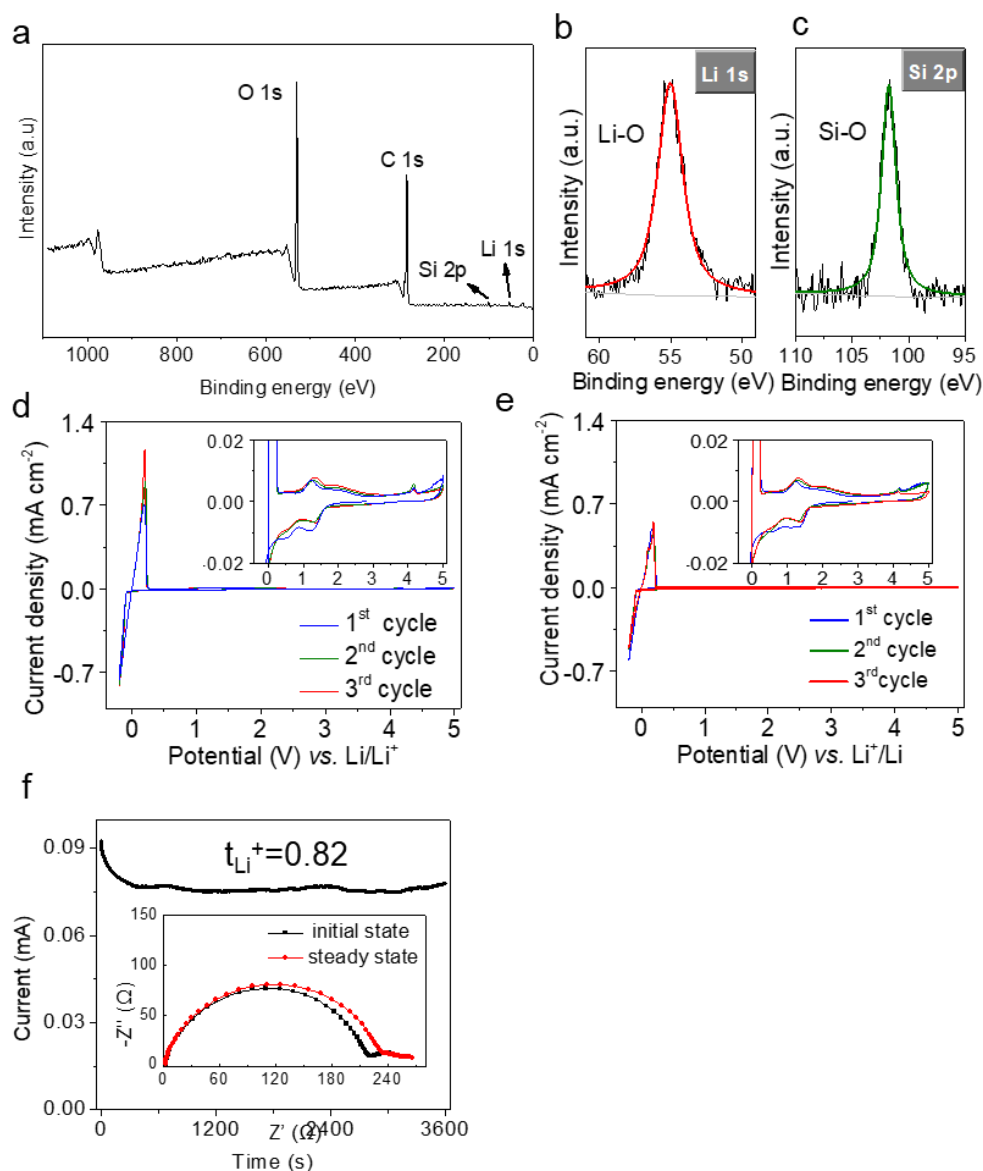
Fig. 4.11 | a, XPS survey scan of ACOF-Li. **b,** XPS analysis of for **b,** Li 1s and **c,** Si 2p

species on ACOF- Li. CV curves of the first 3 cycles of **d,** ACOF-Li and **e,** bare Li

using stainless steel as working electrode (–0.2 to 5 V, 1 mV s^{-1}). **f,** Measurement of

t_{Li^+} using potentiostatic polarization of ACOF-coated Li symmetric cell (inset: Nyquist

plots of impedance before and after polarization).

The X-ray photoelectron spectroscopy (XPS) of ACOF-Li was conducted for surface chemical states. The survey scanning detects signals of C 1s, O 1s, Si 2p and Li 1s, where the atomic ratio between Li and Si (2.5) is in line with stoichiometric composition ($Li_2[Si(C_{16}H_{10}O_4)_{1.5}]$) (**Fig. 4.11a**). Consistently, binding energy at 55.6 eV (Li 1s, **Fig. 4.11b**) and 102.5 eV (Si 2p, **Fig. 4.11c**) is ascribable to skeletal Li–O and Si–O bond, respectively.[220, 221] In addition, absence of metallic Li peak (~ 53.4 eV) and Si–Li bond (~ 54.4 eV, 98 - 98.4 eV) implies the compact coverage and structural integrity of ACOF on Li.[222, 223]

As discussed above, the ACOF layer could turn into electrolyte interphase in presence of liquid electrolyte. Such ion-modulating interphase necessitates ACOF being electrochemically stable, which was assessed by cyclic voltammetry (CV). The test cells employ stainless steel plate, Li metal and 1 M $LiPF_6$ (in EC/DEC) as working electrode, reference/counter electrode, and electrolyte, respectively. The first three CV curves of ACOF-coated Li in range from –0.2 to 5 V (*vs.* Li$^+$/Li) are shown in (**Fig. 4.11d**, in which sharp redox peaks near 0 V were observed for Li$^+$/Li deposition-stripping on steel plate. Relative to the CV curves of bare Li (**Fig. 4.11e**), no appreciable redox activity and decomposition peaks could be attributable to ACOF, signifying excellent electrochemical stability. The selective ion transport in ACOF was validated using an electrochemical technique, which polarizes Li symmetric cell till a steady-state current is established.[224] As shown in **Fig. 4.11f**, the response currents corrected by

resistance (inset of **Fig. 4.11f**) determines a near-unity t_{Li}^+ of 0.82, supporting that the ACOF coating preferentially transports Li-ions in electrolyte.
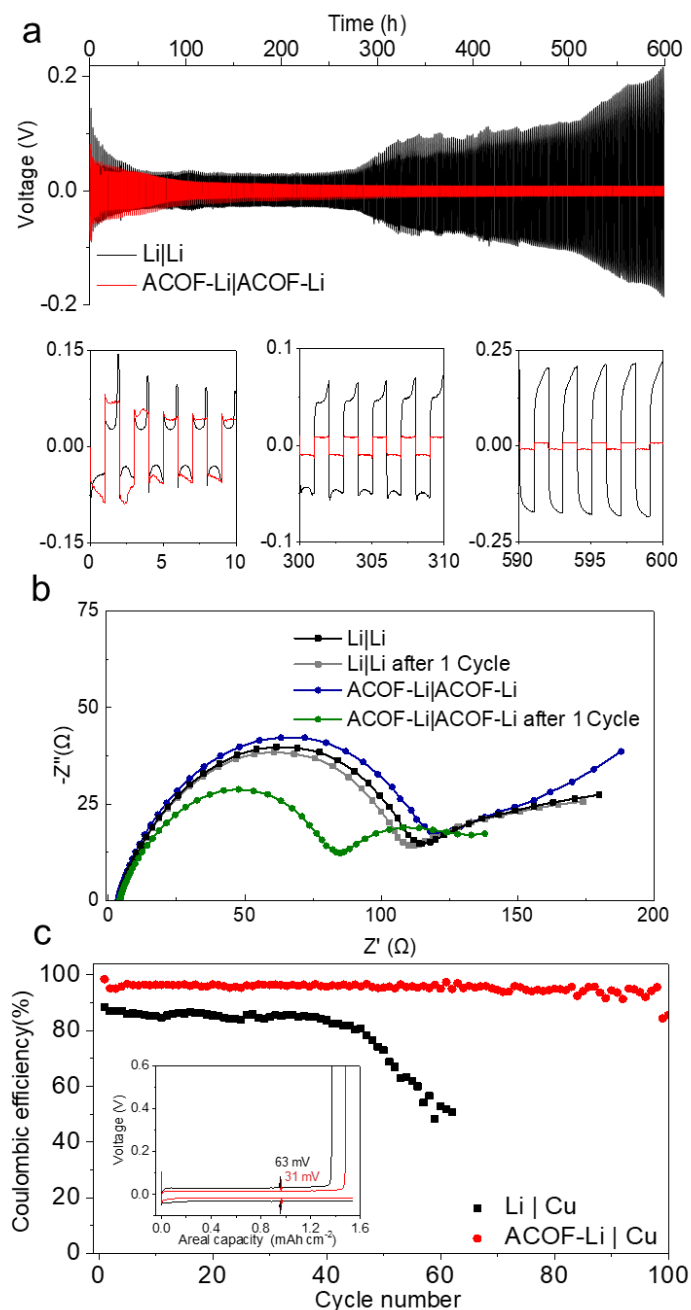
Fig. 4.12 | a, Galvanostatic cycling of Li symmetric cells at areal capacity of 1 mAh cm^{-2} and current density of 1 mA cm^{-2}. **b,** Nyquist plot of impedance spectra of Li|Li and ACOF-Li|ACOF-Li cells after the 1st cycle at a current density of 1 mA cm^{-2}. **c,**

Coulombic efficiencies of Li|bare Li and Li|ACOF-Li as-symmetric cells at 1 mA cm^{-2}, 1 mAh cm^{-2}.

To examine the effect of electrolyte interphase on dendrite suppression, long-term galvanostatic cycling of Li symmetric cells was carried out at 1 mA cm^{-2} for periodic 1 h. As compared in **Fig. 4.11a**, the reference cell without ACOF coating (denoted as Li|Li cell) initially exhibits more drastic fluctuation of overpotential than the cell with ACOF coating (denoted as ACOF-Li|ACOF-Li cell), indicating that the ACOF favors stable Li$^+$/Li deposition. Consequently, reduced cell impedance was observed for ACOF-Li|ACOF-Li cell after cycling (**Fig. 4.11b**). In the long-term, the Li|Li cell shows escalating overpotential from 66 mV at 300 h to 215 mV at 600 h. In contrast, the ACOF-Li|ACOF-Li cell well maintains overpotential below 10 mV at the same time frame. Coulombic efficiency (CE) of thin LMA is critically important for the cell lifespan since the total amount of Li is limited. CEs of Li deposition/dissolution were measured using ACOF coated ultra-thin LMA with a thickness of 50 μm and li chip were measured at 1 mA cm^{-2} with a capacity of 1 mAh cm^{-2}. Before the galvanostatic charge-discharge process, all the lithium on ACOF-Li was initially stripped to the counter electrode forming an ACOF protected Cu electrode. Bare Li anode was measured under the same condition for comparison. A higher average CE is obtained with ACOF protected layer than the control group (**Fig. 4.11c**).
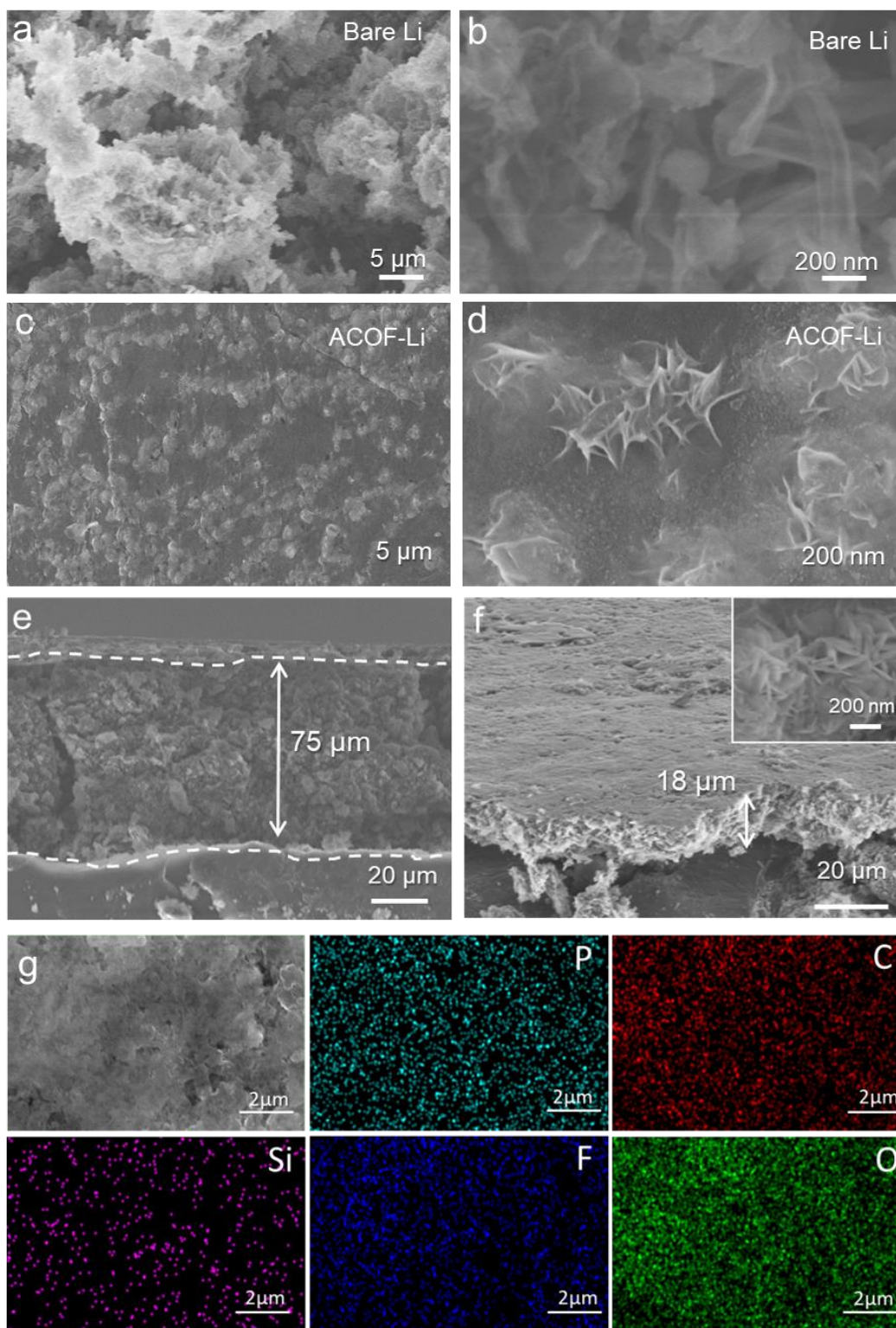
Fig. 4.12 | SEM images of the post-cycle Li electrodes (100 cycles) harvested from a-b, Li|Li and **(c-d)**, ACOF-Li|ACOF-Li cell. SEM images of the cross-ectional Li of the symmetric cells **e**, bare Li; **f**, ACOF-Li (inset is the enlarged view). **g**, SEM elemental

mapping images of the ACOF-Li surface after cycling (cyan: P; red:C; fuchsia: Si; blue:F; green:O).

As shown by SEM images, the Li harvested from Li|Li cell exhibits rough and porous surface with filamentous Li growth (**Figs. 4.12a-b, Fig. 4.12e**), whereas the ACOF-coated Li remains consistently flat and dense (**Figs. 4.12c-d, Fig. 4.12f**). Elemental analysis of carbon, nitrogen and oxygen are carried out and exhibited in **Fig. 4.12g**, conforming homogenous distribution of the ACOF coating film.In particular, the flake-like ACOF particles could be readily distinguished with native SEI components, proving that the ACOF contribute to stable, dendrite-free, and minorly polarized stripping-plating processes.
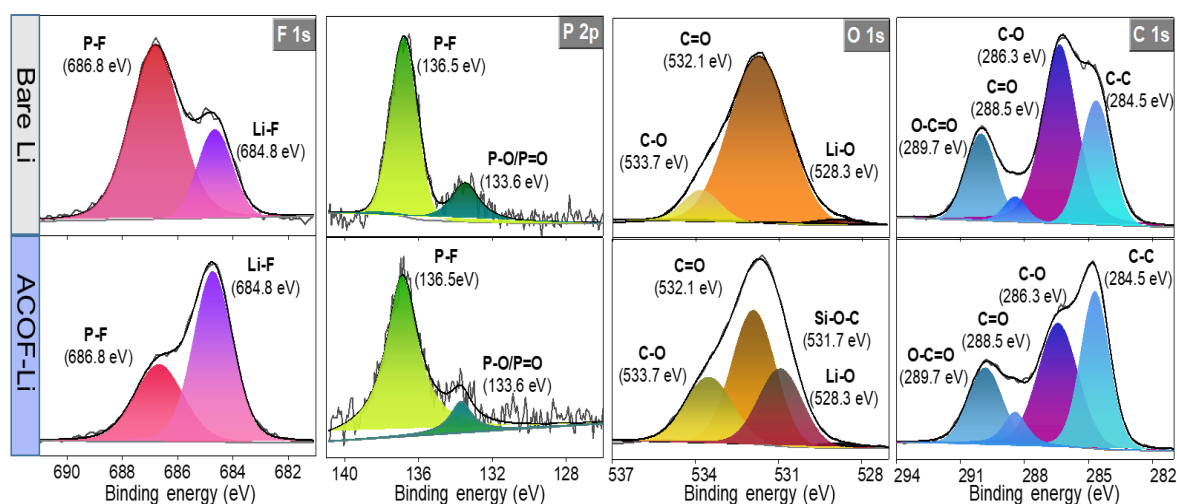
Fig. 4.13 | Deconvoluted XPS spectra (F 1s, P 2p, O 1s and C1s) from cycled Li electrodes of Li|Li and ACOF-Li|ACOF-Li cell, respectively.

The elemental compositions of the surface layer were analyzed by XPS (**Fig. 4.13**). In comparison with the deconvoluted spectra of bare Li, the ACOF-coated Li is noticeably rich with Li–F (684.8 eV), Si–O–C (531.7 eV)/C–O (286.3 eV), which derive from decomposition of anions and backbones of ACOF, respectively.[225, 226] Such abundance of LiF could be explained by SEI-forming decomposition of the localized anions in ACOF.[227]
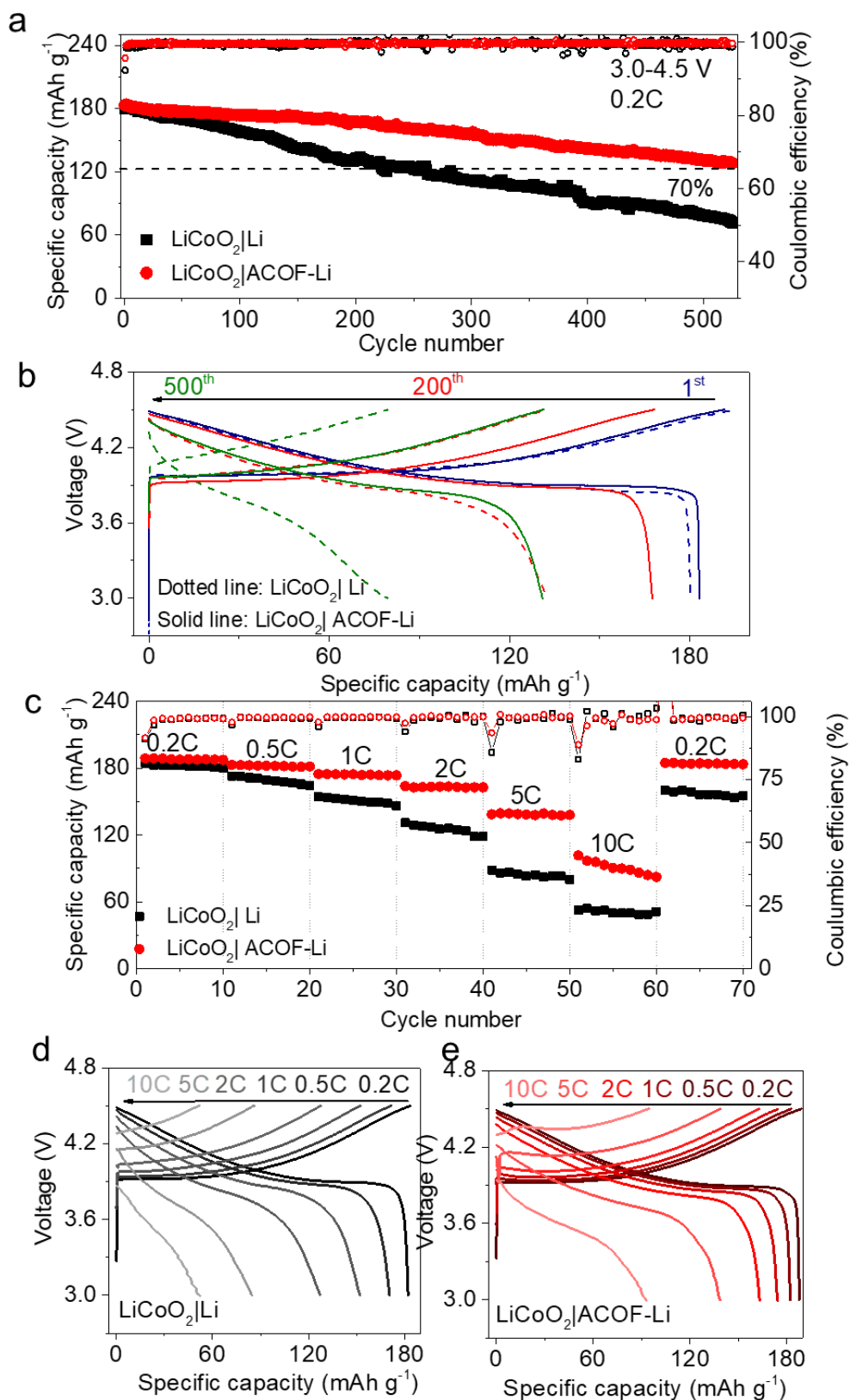
Fig. 4.14 | Electrochemical performances of LiCoO₂|Li and LiCoO₂|ACOF-Li cells. **a**,

Long-term cycling stability at 0.2C, and **b**, corresponding voltage profiles at

$1^{st}/200^{th}/500^{th}$ cycle. **c**, Rate performance, and (**d-e**) representative voltage profiles at C rate of 0.2/0.5/1/2/5/10.

The electrolyte interphase was further assessed in Li metal full cells made by Li foil anodes (50 μm, 10 mAh cm^{-2}) and commercial $LiCoO_2$ cathodes (1 mAh cm^{-2}), which were subject to high-voltage operation at 4.5 V (1C = 180 mA g^{-1}). **Fig. 4.14a** compares the cycle performance of the cells with and without ACOF coating (0.2C), where the reference cell using bare Li foil ($LiCoO_2$|Li) benchmarks a 70% capacity retention at the 210th cycle. In stark contrast, the cell with ACOF-coated Li ($LiCoO_2$|ACOF-Li) robustly retains capacity above the benchmark for over 500 cycles. In comparison with $LiCoO_2$|Li cell, the $LiCoO_2$|ACOF-Li cell displays smaller voltage hysteresis between charge and discharge (**Fig. 4.14b**) curves, which is in accordance with the mitigated overpotential of Li|ACOF-Li during polarization test. The cell rate performance was evaluated by stepwise applying C-rate from 0.2C, 0.5C, 1C, 2C, 5C to 10C (**Fig. 4.14c**). The $LiCoO_2$|ACOF-Li cell shows enhanced attainable capacity as well as reduced overpotential when the C-rate was increased to 0.5C and beyond (**Figs. 4.14d-e**). As exemplified by the rate at 10C, the $LiCoO_2$|ACOF-Li cell could still afford higher capacity of 89 mAh g^{-1}, which is considerably higher than 50 mAh g^{-1} delivered by the $LiCoO_2$|Li cell. The above poor-performing Li anode without ACOF coating roots from degrading Li-electrolyte interface, which is exacerbated by dendrite propagation and high-rate operation.[81] Benefit from the rapid and exclusive pathways for Li$^+$ ions, the ACOF coating effectively suppresses dendrite formation, enabling safe and durable Li

anode for energy-dense Li-metal battery.

4.4 Conclusions

In summary, a facile coating Li anode with anionic COF (ACOF) have been successfully demonstrated with Li dendrite suppression, where the ACOF possess layered structure, as well as densely populated negative charges lined up along microporous frameworks. As an electrolyte interphase for Li anode, ACOF offer strong affinity and fast translocation pathways for Li ions, thereby conferring ionically selective penetration (t_{Li^+} = 0.82) to liquid electrolyte and high conductivity at least of 2.3 mS cm^{-1}. Consequently, prototype Li metal cells show suppressed dendrite, reduced polarization, superb durability and enhanced rate capability. Overall, this work demonstrates that ionic covalent organic frameworks can be potent electrolyte interphase for dendrite-free Li anode, thereby creating new opportunities for other crystalline porous solids.

Chapter 5. Summary and Outlook

To cater to future energy needs, next generation lithium-ion batteries must be energy denser, safer, and cheaper. We conclude that there are three main properties to evaluate a battery, namely power, energy and lifespan. Power is related to electron-ion transport. To achieve high power, it is necessary to minimize polarization, particularly, electrolyte polarization. Energy is about electrode capacity and cell voltage. However, state-of-art lithium-ion batteries usually have poor electrochemical and thermal stability, which exclude the utilization of high energy electrodes like Lithium metal and other high-voltage cathodes. Besides, enhancing the durability of ion-electron transport networks as well as the ion host, and improving the electrolyte interface can prolong batteries lifespan.

In this dissertation, we focus on improving the ion transport of electrolyte and consequent electrode-electrolyte interphase. Three types of porous coordination solids (MOF, COF and polymer) that can selectively modulate ion transport are found to boost battery performances significantly. Manipulation of electronic conductivity has been demonstrated to significantly improve the power density by rational architecture design and incorporating more electronic conductive agents. Tuning ion transport, however, is more challenging, as it will not only govern the mobility of ions in the bulk electrolyte but also impact the electrolyte-electrode interfaces. In summary, the MOF-based electrolyte modulators in Chapter Two exclusively optimizes ion-transport in the electrolyte, which addresses a long-standing issue regarding the dynamic operations of lithium-ion batteries, such as fast-charging or instant braking charging.   In Chapter

Three, we first demonstrated that ionic COF can be potent electrolyte interphase for dendrite-free Li anode. Furthermore, we demonstrated another way for the lithium metal protection in Chapter Four. We create a novel artificial polymeric SEI layer which was uniformly grafted on the lithium metal surface forming an integrated PPQ-stabilized Li anode.

These studies introduce new class of materials for high-energy and high-power-density batteries. Meanwhile, the methodology we proposed is envisioned to be extended to other alkali metal or proton conductors, and helps to explore more efficient architecture design for charge carriers.

While numerous efforts have been made to achieve better batteries, we believe that the most significant advancements still await discovery and understanding, which could accelerate the transition to high energy battery chemistries beyond Lithium-ion.

APPENDIX

Appendix I List of symbols in equations for the LiFePO4|Li cell.

Symbols	Unit	Description
x	[m]	Spatial direction
t	[s]	Time
ϵ_i	–	Porosity
$c_e(x, t)$	[mol m^{-3}]	Electrolyte concentration
r	[m]	Radial direction along which the ions intercalate within the active particles
$D_{\mathbf{eff},i}$	[m^2 s]	Effective electrolyte diffusion coefficient
a_i	[m^2 m^{-3}]	Particle surface area to volume
L_i	[m]	Thickness
$D_{s,i}$	[m^2 s]	Solid-phase diffusivity
$k_{\mathbf{eff},i}$	[m$^{2.5}$ mol$^{-0.5}$ s^{-1})]	Reaction rate constant
$I_{\mathrm{app}}(t)$	[A m^{-2}]	Applied current density
F	96485 [C mol^{-1}]	Faraday's constant
$j(x,t)$	[mol m^{-2} s^{-1})]	Ionic flux
$T(x, t)$	[K]	Temperature
h	[W m^{-2} K^{-1})]	Heat exchange coefficient
c_s^*	[mol m^{-3}]	Average concentration in the solid particles
$\sigma_{\mathbf{eff},i}$	[S m^{-1}]	Effective solid-phase conductivity

$\Phi_s(x,t)$	[V]	Solid potential
$\Phi_e(x,t)$	[V]	Electrolyte potential
$\mathbf{U}_i$	[V]	Open circuit voltage
$\mathbf{\kappa}_{\mathbf{eff},i}$	[S m^{-1}]	Effective electrolyte conductivity
R	8.314472 [J mol^{-1} K^{-1}]	Universal gas constant
t_+	–	Transference number
$\eta_i(x,t)$	[m s^{-1}]	velocity

Appendix II List of symbols in equations for the DST simulation.

Symbols	Unit	Description
$i_{loc,SEI}$	[A m^{-2}]	Local current density
$i_{loc,1C,ref}$	[A m^{-2}]	Local current density with respect to 1C discharge
HK	–	Dimensionless graphite expansion factor function
J	–	Dimensionless exchanging current density for the parasitic reaction
f	[s^{-1}]	Lumped nondimensional parameter
α	–	Transfer coefficient of the parasitic reaction
η_{SEI}	[V]	Overpotential for the parasitic reaction
c_{SEI}	[mol m^{-3}]	Local SEI concentration
υ_{SEI}	–	Stoichiometric coefficient of the SEI species in the

		parasitic reaction
A_υ	[m^{-1}]	Surface area of the negative electrode
δ_{film}	[m]	Thickness of the SEI layer
$\delta_{film,0}$	[m]	Initial thickness of the SEI layer
M_P	[kg mol^{-1}]	molar weight of the product of the parasitic reaction
ρ_P	[kg m^{-3}]	density of the product of the parasitic reaction
R_{film}	[Ω m^2]	Resistance of the SEI layer
κ	[S m^{-1}]	Conductivity of the SEI layer

Load cycles:

o   Charge: 2C constant rate (cutover voltage: 4.4 V);

o   Discharge: DST with a period of 360 seconds (cutoff voltage: 2.5 V).

References

1.   Dunn, B.;   Kamath, H.; Tarascon, J.-M. J. S., Electrical energy storage for the grid: a battery of choices. **2011,** *334* (6058), 928-935.

2.   Goodenough, J. B.; Park, K.-S. J. J. o. t. A. C. S., The Li-ion rechargeable battery: a perspective. **2013,** *135* (4), 1167-1176.

3.   Goodenough, J. B.; Park, K.-S., The Li-Ion Rechargeable Battery: A Perspective. *Journal of the American Chemical Society* **2013,** *135* (4), 1167-1176.

4.   Tarascon, J. M.; Armand, M., Issues and challenges facing rechargeable lithium batteries. *Nature* **2001,** *414*, 359.

5.   Xu, W.;   Wang, J.;   Ding, F.;   Chen, X.;   Nasybulin, E.;   Zhang, Y.; Zhang, J.-G., Lithium metal anodes for rechargeable batteries. *Energy & Environmental Science* **2014,** *7* (2), 513-537.

6.   Bruce, P. G.;   Freunberger, S. A.;   Hardwick, L. J.; Tarascon, J.-M., Li–O2 and Li–S batteries with high energy storage. *Nature Materials* **2011,** *11*, 19.

7.   Brandt, K., Historical development of secondary lithium batteries. *Solid State Ionics* **1994,** *69* (3), 173-183.

8.   Whittingham, M. S., Lithium Batteries and Cathode Materials. *Chemical Reviews* **2004,** *104* (10), 4271-4302.

9.   Dunn, B.;   Kamath, H.; Tarascon, J.-M., Electrical Energy Storage for the Grid: A Battery of Choices. *Science* **2011,** *334* (6058), 928-935.

10. Lundgren, C. A.;   Xu, K.;   Jow, T. R.;   Allen, J.; Zhang, S. S., Lithium-ion batteries and materials. In *Springer Handbook of Electrochemical Energy*, Springer: 2017; pp 449-494.

11. Xu, K., Nonaqueous Liquid Electrolytes for Lithium-Based Rechargeable Batteries. *Chemical*

Reviews **2004,** *104* (10), 4303-4418.

12. Tarascon, J. M.; Armand, M., Issues and challenges facing rechargeable lithium batteries. *Nature* **2001,** *414* (6861), 359-367.

13. Padhi, A. K.; Nanjundaswamy, K. S.; Goodenough, J. B., Phospho-olivines as Positive-Electrode Materials for Rechargeable Lithium Batteries. *J. Electrochem. Soc.* **1997,** *144* (4), 1188-1194.

14. Julien, C.; Mauger, A.; Vijh, A.; Zaghib, K., *Lithium Batteries* Springer International Publishing: 2016.

15. Lin, D.; Liu, Y.; Cui, Y. J. N. n., Reviving the lithium metal anode for high-energy batteries. **2017,** *12* (3), 194.

16. Xiao, J. J. S., How lithium dendrites form in liquid batteries. **2019,** *366* (6464), 426-427.

17. Zachman, M. J.; Tu, Z.; Choudhury, S.; Archer, L. A.; Kourkoutis, L. F. J. N., Cryo-STEM mapping of solid–liquid interfaces and dendrites in lithium-metal batteries. **2018,** *560* (7718), 345-349.

18. Despić, A.; Popov, K. I., Transport-controlled deposition and dissolution of metals. In *Modern Aspects of Electrochemistry No. 7*, Springer: 1972; pp 199-313.

19. Chazalviel, J., J.-N. Chazalviel, Phys. Rev. A 42, 7355 (1990). *Phys. Rev. A* **1990,** *42*, 7355.

20. Brissot, C.; Rosso, M.; Chazalviel, J.-N.; Lascaud, S., Dendritic growth mechanisms in lithium/polymer cells. *Journal of power sources* **1999,** *81*, 925-929.

21. Rosso, M.; Gobron, T.; Brissot, C.; Chazalviel, J.-N.; Lascaud, S., Onset of dendritic growth in lithium/polymer cells. *Journal of power sources* **2001,** *97*, 804-806.

22. Ding, F.; Xu, W.; Graff, G. L.; Zhang, J.; Sushko, M. L.; Chen, X.; Shao, Y.; Engelhard,

M. H.; Nie, Z.; Xiao, J.; Liu, X.; Sushko, P. V.; Liu, J.; Zhang, J.-G., Dendrite-Free Lithium Deposition via Self-Healing Electrostatic Shield Mechanism. *Journal of the American Chemical Society* **2013,** *135* (11), 4450-4456.

23. Monroe, C.; Newman, J., Dendrite growth in lithium/polymer systems a propagation model for liquid electrolytes under galvanostatic conditions. *Journal of The Electrochemical Society* **2003,** *150* (10), A1377-A1384.

24. Qi, Y.; Guo, H.; Hector, L. G.; Timmons, A., Threefold increase in the Young's modulus of graphite negative electrode during lithium intercalation. *Journal of The Electrochemical Society* **2010,** *157* (5), A558-A566.

25. Chan, C. K.; Peng, H.; Liu, G.; McIlwrath, K.; Zhang, X. F.; Huggins, R. A.; Cui, Y., High-performance lithium battery anodes using silicon nanowires. In *Materials for Sustainable Energy: A Collection of Peer-Reviewed Research and Review Articles from Nature Publishing Group*, World Scientific: 2011; pp 187-191.

26. Peled, E., The Electrochemical Behavior of Alkali and Alkaline Earth Metals in Nonaqueous Battery Systems—The Solid Electrolyte Interphase Model. *Journal of The Electrochemical Society* **1979,** *126* (12), 2047-2051.

27. Peled, E.; Golodnitsky, D.; Ardel, G., Advanced Model for Solid Electrolyte Interphase Electrodes in Liquid and Polymer Electrolytes. *Journal of The Electrochemical Society* **1997,** *144* (8), L208-L210.

28. Peled, E.; Menkin, S., Review—SEI: Past, Present and Future. *Journal of The Electrochemical Society* **2017,** *164* (7), A1703-A1719.

29. Aurbach, D.; Daroux, M. L.; Faguy, P. W.; Yeager, E., Identification of Surface Films Formed

on Lithium in Propylene Carbonate Solutions. *Journal of The Electrochemical Society* **1987,** *134* (7), 1611-1620.

30. Aurbach, D., Review of selected electrode–solution interactions which determine the performance of Li and Li ion batteries. *Journal of Power Sources* **2000,** *89* (2), 206-218.

31. Fong, R.; von Sacken, U.; Dahn, J. R., Studies of Lithium Intercalation into Carbons Using Nonaqueous Electrochemical Cells. *Journal of The Electrochemical Society* **1990,** *137* (7), 2009-2013.

32. Lin, D.; Liu, Y.; Cui, Y., Reviving the lithium metal anode for high-energy batteries. *Nature Nanotechnology* **2017,** *12*, 194.

33. Cohen, Y. S.; Cohen, Y.; Aurbach, D., Micromorphological Studies of Lithium Electrodes in Alkyl Carbonate Solutions Using in Situ Atomic Force Microscopy. *The Journal of Physical Chemistry B* **2000,** *104* (51), 12282-12291.

34. Wang, A.; Kadam, S.; Li, H.; Shi, S.; Qi, Y. J. n. C. M., Review on modeling of the anode solid electrolyte interphase (SEI) for lithium-ion batteries. **2018,** *4* (1), 1-26.

35. Aurbach, D.; Ein-Ely, Y.; Zaban, A., The Surface Chemistry of Lithium Electrodes in Alkyl Carbonate Solutions. *Journal of The Electrochemical Society* **1994,** *141* (1), L1-L3.

36. Li, Y.; Li, Y.; Pei, A.; Yan, K.; Sun, Y.; Wu, C.-L.; Joubert, L.-M.; Chin, R.; Koh, A. L.; Yu, Y.; Perrino, J.; Butz, B.; Chu, S.; Cui, Y., Atomic structure of sensitive battery materials and interfaces revealed by cryo–electron microscopy. *Science* **2017,** *358* (6362), 506-510.

37. Aurbach, D.; Ein-Eli, Y.; Markovsky, B.; Zaban, A.; Luski, S.; Carmeli, Y.; Yamin, H., The study of electrolyte solutions based on ethylene and diethyl carbonates for rechargeable Li batteries II. Graphite electrodes. *Journal of The Electrochemical Society* **1995,** *142* (9), 2882-2890.

38. Huff, L. A.; Tavassol, H.; Esbenshade, J. L.; Xing, W.; Chiang, Y.-M.; Gewirth, A. A., Identification of Li-Ion Battery SEI Compounds through 7Li and 13C Solid-State MAS NMR Spectroscopy and MALDI-TOF Mass Spectrometry. *ACS Applied Materials & Interfaces* **2016,** *8* (1), 371-380.

39. Gofer, Y.; Ben-Zion, M.; Aurbach, D., Solutions of LiAsF6 in 1,3-dioxolane for secondary lithium batteries. *Journal of Power Sources* **1992,** *39* (2), 163-178.

40. Li, Y.; Huang, W.; Li, Y.; Chiu, W.; Cui, Y. J. A. n., Opportunities for Cryogenic Electron Microscopy in Materials Science and Nanoscience. **2020,** *14* (8), 9263-9276.

41. Li, Y.; Li, Y.; Pei, A.; Yan, K.; Sun, Y.; Wu, C.-L.; Joubert, L.-M.; Chin, R.; Koh, A. L.; Yu, Y. J. S., Atomic structure of sensitive battery materials and interfaces revealed by cryo–electron microscopy. **2017,** *358* (6362), 506-510.

42. Bachman, J. C.; Muy, S.; Grimaud, A.; Chang, H.-H.; Pour, N.; Lux, S. F.; Paschos, O.; Maglia, F.; Lupart, S.; Lamp, P., Inorganic solid-state electrolytes for lithium batteries: mechanisms and properties governing ion conduction. *Chemical reviews* **2015,** *116* (1), 140-162.

43. Goodenough, J. B., Oxide-Ion Electrolytes. *Annual Review of Materials Research* **2003,** *33* (1), 91-128.

44. Linford, R.; Hackwood, S., Physical techniques for the study of solid electrolytes. *Chemical Reviews* **1981,** *81* (4), 327-364.

45. Evans, J.; Vincent, C. A.; Bruce, P. G., Electrochemical measurement of transference numbers in polymer electrolytes. *Polymer* **1987,** *28* (13), 2324-2328.

46. Yang, C.; Fu, K.; Zhang, Y.; Hitz, E.; Hu, L., Protected Lithium-Metal Anodes in Batteries: From Liquid to Solid. *Advanced Materials* **2017,** *29* (36), 1701169.

47. Zhang, K.; Lee, G. H.; Park, M.; Li, W.; Kang, Y. M., Recent developments of the lithium metal anode for rechargeable non-aqueous batteries. *Advanced Energy Materials* **2016,** *6* (20), 1600811.

48. Aurbach, D.; Zinigrad, E.; Cohen, Y.; Teller, H., A short review of failure mechanisms of lithium metal and lithiated graphite anodes in liquid electrolyte solutions. *Solid state ionics* **2002,** *148* (3-4), 405-416.

49. Manthiram, A.; Yu, X.; Wang, S., Lithium battery chemistries enabled by solid-state electrolytes. *Nature Reviews Materials* **2017,** *2* (4), 16103.

50. Park, J.; Jeong, J.; Lee, Y.; Oh, M.; Ryou, M. H.; Lee, Y. M., Micro-Patterned Lithium Metal Anodes with Suppressed Dendrite Formation for Post Lithium-Ion Batteries. *Advanced Materials Interfaces* **2016,** *3* (11), 1600140.

51. Zhang, R.; Li, N. W.; Cheng, X. B.; Yin, Y. X.; Zhang, Q.; Guo, Y. G., Advanced micro/nanostructures for lithium metal anodes. *Advanced Science* **2017,** *4* (3), 1600445.

52. Ramaswamy, P.; Wong, N. E.; Shimizu, G. K. H., MOFs as proton conductors - challenges and opportunities. *Chemical Society Reviews* **2014,** *43* (16), 5913-5932.

53. Lu, Y.; Das, S. K.; Moganty, S. S.; Archer, L. A., Ionic Liquid-Nanoparticle Hybrid Electrolytes and their Application in Secondary Lithium-Metal Batteries. *Advanced Materials* **2012,** *24* (32), 4430-4435.

54. Tu, Z.; Kambe, Y.; Lu, Y.; Archer, L. A., Nanoporous polymer - ceramic composite electrolytes for lithium metal batteries. *Advanced Energy Materials* **2014,** *4* (2).

55. Park, K.; Cho, J. H.; Shanmuganathan, K.; Song, J.; Peng, J.; Gobet, M.; Greenbaum, S.; Ellison, C. J.; Goodenough, J. B., New battery strategies with a polymer/Al 2 O 3 separator.

Journal of Power Sources **2014,** *263*, 52-58.

56. Ansari, Y.; Guo, B.; Cho, J. H.; Park, K.; Song, J.; Ellison, C. J.; Goodenough, J. B., Low-Cost, Dendrite-Blocking Polymer-Sb2O3 Separators for Lithium and Sodium Batteries. *Journal of The Electrochemical Society* **2014,** *161* (10), A1655-A1661.

57. Zhang, J.; Bai, Y.; Sun, X.-G.; Li, Y.; Guo, B.; Chen, J.; Veith, G. M.; Hensley, D. K.; Paranthaman, M. P.; Goodenough, J. B., Superior conductive solid-like electrolytes: nanoconfining liquids within the hollow structures. *Nano letters* **2015,** *15* (5), 3398-3402.

58. Ameloot, R.; Aubrey, M.; Wiers, B. M.; Gómora-Figueroa, A. P.; Patel, S. N.; Balsara, N. P.; Long, J. R., Ionic Conductivity in the Metal–Organic Framework UiO-66 by Dehydration and Insertion of Lithium tert-Butoxide. *Chemistry-A European Journal* **2013,** *19* (18), 5533-5536.

59. Song, J. Y.; Ahmed, I.; Seo, P. W.; Jhung, S. H., UiO-66-Type Metal–Organic Framework with Free Carboxylic Acid: Versatile Adsorbents via H-bond for Both Aqueous and Nonaqueous Phases. *ACS Applied Materials & Interfaces* **2016,** *8* (40), 27394-27402.

60. Zhang, J.-P.; Zhang, Y.-B.; Lin, J.-B.; Chen, X.-M., Metal azolate frameworks: from crystal engineering to functional materials. *Chemical reviews* **2011,** *112* (2), 1001-1033.

61. Mason, J. A.; Veenstra, M.; Long, J. R., Evaluating metal–organic frameworks for natural gas storage. *Chemical Science* **2014,** *5* (1), 32-51.

62. Kalmutzki, M. J.; Hanikel, N.; Yaghi, O. M. J. S. a., Secondary building units as the turning point in the development of the reticular chemistry of MOFs. **2018,** *4* (10), eaat9180.

63. Yamada, T.; Sadakiyo, M.; Kitagawa, H., High proton conductivity of one-dimensional ferrous oxalate dihydrate. *Journal of the American Chemical Society* **2009,** *131* (9), 3144-3145.

64. Yoon, M.; Suh, K.; Natarajan, S.; Kim, K., Proton conduction in metal–organic frameworks

and related modularly built porous solids. *Angewandte Chemie International Edition* **2013,** *52* (10), 2688-2700.

65. Shen, L.; Wu, H. B.; Liu, F.; Brosmer, J. L.; Shen, G.; Wang, X.; Zink, J. I.; Xiao, Q.; Cai, M.; Wang, G. J. A. M., Creating Lithium-Ion Electrolytes with Biomimetic Ionic Channels in Metal–Organic Frameworks. **2018,** *30* (23), 1707476.

66. Feng, X.; Ding, X.; Jiang, D., Covalent organic frameworks. *Chemical Society Reviews* **2012,** *41* (18), 6010-6022.

67. Ding, S.-Y.; Wang, W., Covalent organic frameworks (COFs): from design to applications. *Chemical Society Reviews* **2013,** *42* (2), 548-568.

68. Diercks, C. S.; Yaghi, O. M. J. S., The atom, the molecule, and the covalent organic framework. **2017,** *355* (6328).

69. Han, S. S.; Furukawa, H.; Yaghi, O. M.; Goddard Iii, W. A., Covalent organic frameworks as exceptional hydrogen storage materials. *Journal of the American Chemical Society* **2008,** *130* (35), 11580-11581.

70. Wan, S.; Guo, J.; Kim, J.; Ihee, H.; Jiang, D., A photoconductive covalent organic framework: self-condensed arene cubes composed of eclipsed 2D polypyrene sheets for photocurrent generation. *Angewandte Chemie* **2009,** *121* (30), 5547-5550.

71. Patwardhan, S.; Kocherzhenko, A. A.; Grozema, F. C.; Siebbeles, L. D., Delocalization and mobility of charge carriers in covalent organic frameworks. *The Journal of Physical Chemistry C* **2011,** *115* (23), 11768-11772.

72. Cote, A. P.; El-Kaderi, H. M.; Furukawa, H.; Hunt, J. R.; Yaghi, O. M., Reticular synthesis of microporous and mesoporous 2D covalent organic frameworks. *Journal of the American Chemical*

Society **2007,** *129* (43), 12914-12915.

73. Uribe-Romo, F. J.; Doonan, C. J.; Furukawa, H.; Oisaki, K.; Yaghi, O. M., Crystalline covalent organic frameworks with hydrazone linkages. *Journal of the American Chemical Society* **2011,** *133* (30), 11478-11481.

74. Cote, A. P.; Benin, A. I.; Ockwig, N. W.; O'keeffe, M.; Matzger, A. J.; Yaghi, O. M., Porous, crystalline, covalent organic frameworks. *science* **2005,** *310* (5751), 1166-1170.

75. Grill, L.; Dyer, M.; Lafferentz, L.; Persson, M.; Peters, M. V.; Hecht, S., Nano-architectures by covalent assembly of molecular building blocks. *Nature nanotechnology* **2007,** *2* (11), 687.

76. Liu, Y.; Zhu, Y.; Cui, Y., Challenges and opportunities towards fast-charging battery materials. *Nature Energy* **2019,** *4* (7), 540-550.

77. Arora, P.; Doyle, M.; Gozdz, A. S.; White, R. E.; Newman, J., Comparison between computer simulations and experimental data for high-rate discharges of plastic lithium-ion batteries. *Journal of Power Sources* **2000,** *88* (2), 219-231.

78. Doyle, M.; Fuller, T. F.; Newman, J., Modeling of Galvanostatic Charge and Discharge of the Lithium/Polymer/Insertion Cell. *Journal of The Electrochemical Society* **1993,** *140* (6), 1526-1533.

79. Cano, Z. P.; Banham, D.; Ye, S.; Hintennach, A.; Lu, J.; Fowler, M.; Chen, Z. J. N. E., Batteries and fuel cells for emerging electric vehicle markets. **2018,** *3* (4), 279-289.

80. Keil, P.; Jossen, A., Impact of Dynamic Driving Loads and Regenerative Braking on the Aging of Lithium-Ion Batteries in Electric Vehicles. *Journal of The Electrochemical Society* **2017,** *164* (13), A3081-A3092.

81. Logan, E. R.; Dahn, J. R., Electrolyte Design for Fast-Charging Li-Ion Batteries. *Trends in*

Chemistry **2020,** *2* (4), 354-366.

82. Nyman, A.; Zavalis, T. G.; Elger, R.; Behm, M. r.; Lindbergh, G. r., Analysis of the Polarization in a Li-Ion Battery Cell by Numerical Simulations. *Journal of The Electrochemical Society* **2010,** *157* (11), A1236.

83. Cho, Y.-G.; Kim, Y.-S.; Sung, D.-G.; Seo, M.-S.; Song, H.-K., Nitrile-assistant eutectic electrolytes for cryogenic operation of lithium ion batteries at fast charges and discharges. *Energy & Environmental Science* **2014,** *7* (5), 1737-1743.

84. Hilbig, P.; Ibing, L.; Winter, M.; Cekic-Laskovic, I., Butyronitrile-Based Electrolytes for Fast Charging of Lithium-Ion Batteries. *Energies* **2019,** *12* (15).

85. Diederichsen, K. M.; McShane, E. J.; McCloskey, B. D., Promising Routes to a High Li+ Transference Number Electrolyte for Lithium Ion Batteries. *ACS Energy Letters* **2017,** *2* (11), 2563-2575.

86. Lagadec, M. F.; Zahn, R.; Wood, V., Characterization and performance evaluation of lithium-ion battery separators. *Nature Energy* **2019,** *4* (1), 16-25.

87. Popovic, J.; Höfler, D.; Melchior, J. P.; Münchinger, A.; List, B.; Maier, J., High Lithium Transference Number Electrolytes Containing Tetratriflylpropene's Lithium Salt. *The Journal of Physical Chemistry Letters* **2018,** *9* (17), 5116-5120.

88. Borodin, O.; Suo, L.; Gobet, M.; Ren, X.; Wang, F.; Faraone, A.; Peng, J.; Olguin, M.; Schroeder, M.; Ding, M. S.; Gobrogge, E.; von Wald Cresce, A.; Munoz, S.; Dura, J. A.; Greenbaum, S.; Wang, C.; Xu, K., Liquid Structure with Nano-Heterogeneity Promotes Cationic Transport in Concentrated Electrolytes. *ACS Nano* **2017,** *11* (10), 10462-10471.

89. Suo, L.; Hu, Y.-S.; Li, H.; Armand, M.; Chen, L., A new class of Solvent-in-Salt electrolyte

for high-energy rechargeable metallic lithium batteries. *Nature Communications* **2013,** *4* (1), 1481.

90. Song, J.; Lee, H.; Choo, M.-J.; Park, J.-K.; Kim, H.-T., Ionomer-Liquid Electrolyte Hybrid Ionic Conductor for High Cycling Stability of Lithium Metal Electrodes. *Scientific Reports* **2015,** *5* (1), 14458.

91. Liu, Q. Q.; Ma, L.; Du, C. Y.; Dahn, J. R., Effects of the LiPO2F2 additive on unwanted lithium plating in lithium-ion cells. *Electrochimica Acta* **2018,** *263*, 237-248.

92. Liu, Q. Q.; Xiong, D. J.; Petibon, R.; Du, C. Y.; Dahn, J. R., Gas Evolution during Unwanted Lithium Plating in Li-Ion Cells with EC-Based or EC-Free Electrolytes. *Journal of The Electrochemical Society* **2016,** *163* (14), A3010-A3015.

93. Wang, R.; Wang, Z.; Xu, Y.; Dai, F.; Zhang, L.; Sun, D., Porous Zirconium Metal–Organic Framework Constructed from 2D → 3D Interpenetration Based on a 3,6-Connected kgd Net. *Inorganic Chemistry* **2014,** *53* (14), 7086-7088.

94. Largeot, C.; Portet, C.; Chmiola, J.; Taberna, P.-L.; Gogotsi, Y.; Simon, P., Relation between the Ion Size and Pore Size for an Electric Double-Layer Capacitor. *Journal of the American Chemical Society* **2008,** *130* (9), 2730-2731.

95. Krachkovskiy, S. A.; Bazak, J. D.; Werhun, P.; Balcom, B. J.; Halalay, I. C.; Goward, G. R., Visualization of Steady-State Ionic Concentration Profiles Formed in Electrolytes during Li-Ion Battery Operation and Determination of Mass-Transport Properties by in Situ Magnetic Resonance Imaging. *Journal of the American Chemical Society* **2016,** *138* (25), 7992-7999.

96. Takamatsu, D.; Yoneyama, A.; Asari, Y.; Hirano, T., Quantitative Visualization of Salt Concentration Distributions in Lithium-Ion Battery Electrolytes during Battery Operation Using X-ray Phase Imaging. *Journal of the American Chemical Society* **2018,** *140* (5), 1608-1611.

97. Klett, M.; Giesecke, M.; Nyman, A.; Hallberg, F.; Lindström, R. W.; Lindbergh, G.; Furó, I., Quantifying Mass Transport during Polarization in a Li Ion Battery Electrolyte by in Situ 7Li NMR Imaging. *Journal of the American Chemical Society* **2012,** *134* (36), 14654-14657.

98. Ma, J.; Wong-Foy, A. G.; Matzger, A. J., The Role of Modulators in Controlling Layer Spacings in a Tritopic Linker Based Zirconium 2D Microporous Coordination Polymer. *Inorganic Chemistry* **2015,** *54* (10), 4591-4593.

99. Delley, B., An all-electron numerical method for solving the local density functional for polyatomic molecules. *The Journal of Chemical Physics* **1990,** *92* (1), 508-517.

100. Delley, B., From molecules to solids with the DMol3 approach. *The Journal of Chemical Physics* **2000,** *113* (18), 7756-7764.

101. Perdew, J. P.; Burke, K.; Ernzerhof, M., Generalized Gradient Approximation Made Simple. *Physical Review Letters* **1996,** *77* (18), 3865-3868.

102. Grimme, S., Semiempirical GGA-type density functional constructed with a long-range dispersion correction. *Journal of Computational Chemistry* **2006,** *27* (15), 1787-1799.

103. Delley, B., Hardness conserving semilocal pseudopotentials. *Physical Review B* **2002,** *66* (15), 155125.

104. Monkhorst, H. J.; Pack, J. D., Special points for Brillouin-zone integrations. *Physical Review B* **1976,** *13* (12), 5188-5192.

105. Cai, L.; White, R. E., Mathematical modeling of a lithium ion battery with thermal effects in COMSOL Inc. Multiphysics (MP) software. *Journal of Power Sources* **2011,** *196* (14), 5985-5989.

106. Zugmann, S.; Fleischmann, M.; Amereller, M.; Gschwind, R. M.; Wiemhöfer, H. D.; Gores, H. J., Measurement of transference numbers for lithium ion electrolytes via four different methods,

a comparative study. *Electrochimica Acta* **2011,** *56* (11), 3926-3933.

107. Xu, W.; Wang, J.; Ding, F.; Chen, X.; Nasybulin, E.; Zhang, Y.; Zhang, J.-G. J. E.; Science, E., Lithium metal anodes for rechargeable batteries. **2014,** *7* (2), 513-537.

108. Wang, R.; Wang, Z.; Xu, Y.; Dai, F.; Zhang, L.; Sun, D. J. I. c., Porous zirconium metal–organic framework constructed from 2D→ 3D interpenetration based on a 3, 6-connected kgd net. **2014,** *53* (14), 7086-7088.

109. Ma, J.; Wong-Foy, A. G.; Matzger, A. J. J. I. c., The role of modulators in controlling layer spacings in a tritopic linker based zirconium 2D microporous coordination polymer. **2015,** *54* (10), 4591-4593.

110. Ragon, F.; Campo, B.; Yang, Q.; Martineau, C.; Wiersum, A. D.; Lago, A.; Guillerm, V.; Hemsley, C.; Eubank, J. F.; Vishnuvarthan, M. J. J. o. M. C. A., Acid-functionalized UiO-66 (Zr) MOFs and their evolution after intra-framework cross-linking: structural features and sorption properties. **2015,** *3* (7), 3294-3309.

111. Shen, L.; Wu, H. B.; Liu, F.; Brosmer, J. L.; Shen, G.; Wang, X.; Zink, J. I.; Xiao, Q.; Cai, M.; Wang, G.; Lu, Y.; Dunn, B., Creating Lithium-Ion Electrolytes with Biomimetic Ionic Channels in Metal–Organic Frameworks. *Advanced Materials* **2018,** *30* (23), 1707476.

112. Suo, L.; Zheng, F.; Hu, Y.-S.; Chen, L. J. C. P. B., FT-Raman spectroscopy study of solvent-in-salt electrolytes. **2015,** *25* (1), 016101.

113. Zhang, J.-Y.; Zhang, N.; Zhang, L.; Fang, Y.; Deng, W.; Yu, M.; Wang, Z.; Li, L.; Liu, X.; Li, J. J. S. r., Adsorption of uranyl ions on amine-functionalization of MIL-101 (Cr) nanoparticles by a facile coordination-based post-synthetic strategy and X-ray absorption spectroscopy studies. **2015,** *5*, 13514.

114. Sang, X.; Zhang, J.; Xiang, J.; Cui, J.; Zheng, L.; Zhang, J.; Wu, Z.; Li, Z.; Mo, G.; Xu, Y. J. N. c., Ionic liquid accelerates the crystallization of Zr-based metal–organic frameworks. **2017,** *8* (1), 1-7.

115. Evans, J.; Vincent, C. A.; Bruce, P. G. J. P., Electrochemical measurement of transference numbers in polymer electrolytes. **1987,** *28* (13), 2324-2328.

116. Bai, S.; Sun, Y.; Yi, J.; He, Y.; Qiao, Y.; Zhou, H. J. J., High-power Li-metal anode enabled by metal-organic framework modified electrolyte. **2018,** *2* (10), 2117-2132.

117. Feng, G.; Qiao, R.; Huang, J.; Dai, S.; Sumpter, B. G.; Meunier, V. J. P. C. C. P., The importance of ion size and electrode curvature on electrical double layers in ionic liquids. **2011,** *13* (3), 1152-1161.

118. Lin, R.; Taberna, P.-L.; Chmiola, J.; Guay, D.; Gogotsi, Y.; Simon, P. J. J. o. t. E. S., Microelectrode study of pore size, ion size, and solvent effects on the charge/discharge behavior of microporous carbons for electrical double-layer capacitors. **2009,** *156* (1), A7-A12.

119. Granqvist, C. G., *Handbook of inorganic electrochromic materials*. Elsevier: 1995.

120. Diao, Y.; Xie, K.; Xiong, S.; Hong, X., Insights into Li-S Battery Cathode Capacity Fading Mechanisms: Irreversible Oxidation of Active Mass during Cycling. *Journal of The Electrochemical Society* **2012,** *159* (11), A1816-A1821.

121. Alvarado, J.; Schroeder, M. A.; Pollard, T. P.; Wang, X.; Lee, J. Z.; Zhang, M.; Wynn, T.; Ding, M.; Borodin, O.; Meng, Y. S.; Xu, K., Bisalt ether electrolytes: a pathway towards lithium metal batteries with Ni-rich cathodes. *Energy & Environmental Science* **2019,** *12* (2), 780-794.

122. Chen, W.; Hu, Y.; Lv, W.; Lei, T.; Wang, X.; Li, Z.; Zhang, M.; Huang, J.; Du, X.; Yan,

Y. J. N. c., Lithiophilic montmorillonite serves as lithium ion reservoir to facilitate uniform lithium deposition. **2019,** *10* (1), 1-9.

123. Bai, P.;   Li, J.;   Brushett, F. R.;   Bazant, M. Z. J. E.; Science, E., Transition of lithium growth mechanisms in liquid electrolytes. **2016,** *9* (10), 3221-3229.

124. Cai, L.; White, R. E. In *Mathematical Modeling of a Lithium Ion Battery*, Proceedings of the COMSOL Conference, 2009.

125. Torchio, M.;   Magni, L.;   Gopaluni, R. B.;   Braatz, R. D.; Raimondo, D. M. J. J. o. T. E. S., Lionsimba: a matlab framework based on a finite volume model suitable for li-ion battery design, simulation, and control. **2016,** *163* (7), A1192-A1205.

126. Armand, M.; Tarascon, J. M., Building better batteries. *Nature* **2008,** *451* (7179), 652-657.

127. Wang, M.;   Zhang, F.;   Lee, C.-S.; Tang, Y., Low-Cost Metallic Anode Materials for High Performance Rechargeable Batteries. *Adv. Energy Mater.*, 1700536-n/a.

128. Cheng, X.-B.;   Zhang, R.;   Zhao, C.-Z.; Zhang, Q., Toward Safe Lithium Metal Anode in Rechargeable Batteries: A Review. *Chem. Rev.* **2017,** *117* (15), 10403-10473.

129. Guo, Y.;   Li, H.; Zhai, T., Reviving Lithium-Metal Anodes for Next-Generation High-Energy Batteries. *Adv. Mater.* **2017,** *29* (29), 1700007.

130. Lin, D.;   Liu, Y.; Cui, Y., Reviving the lithium metal anode for high-energy batteries. *Nat Nano* **2017,** *12* (3), 194-206.

131. Liu, B.;   Zhang, J.-G.; Xu, W., Advancing Lithium Metal Batteries. *Joule* **2018,** *2* (5), 833-845.

132. Liu, D.-H.;   Bai, Z.;   Li, M.;   Yu, A.;   Luo, D.;   Liu, W.;   Yang, L.;   Lu, J.;   Amine, K.; Chen, Z., Developing high safety Li-metal anodes for future high-energy Li-metal batteries: strategies and perspectives. *Chem. Soc. Rev.* **2020,** *49* (15), 5407-5445.

169

133. Um, J. H.; Kim, K.; Park, J.; Sung, Y.-E.; Yu, S.-H., Revisiting the strategies for stabilizing lithium metal anodes. *J. Mater. Chem. A* **2020,** *8* (28), 13874-13895.

134. Sun, X.; Zhang, X.; Ma, Q.; Guan, X.; Wang, W.; Luo, J., Revisiting the Electroplating Process for Lithium-Metal Anodes for Lithium-Metal Batteries. *Angew. Chem. Int. Ed.* **2020,** *59* (17), 6665-6674.

135. Lee, B.; Paek, E.; Mitlin, D.; Lee, S. W., Sodium Metal Anodes: Emerging Solutions to Dendrite Growth. *Chem. Rev.* **2019,** *119* (8), 5416-5460.

136. Cui, C.; Yang, C.; Eidson, N.; Chen, J.; Han, F.; Chen, L.; Luo, C.; Wang, P.-F.; Fan, X.; Wang, C., A Highly Reversible, Dendrite-Free Lithium Metal Anode Enabled by a Lithium-Fluoride-Enriched Interphase. *Adv. Mater.* **2020,** *32* (12), 1906427.

137. Liu, J.; Bao, Z.; Cui, Y.; Dufek, E. J.; Goodenough, J. B.; Khalifah, P.; Li, Q.; Liaw, B. Y.; Liu, P.; Manthiram, A.; Meng, Y. S.; Subramanian, V. R.; Toney, M. F.; Viswanathan, V. V.; Whittingham, M. S.; Xiao, J.; Xu, W.; Yang, J.; Yang, X.-Q.; Zhang, J.-G., Pathways for practical high-energy long-cycling lithium metal batteries. *Nat. Energy* **2019,** *4* (3), 180-186.

138. Lu, Y.; Tu, Z.; Archer, L. A., Stable lithium electrodeposition in liquid and nanoporous solid electrolytes. *Nat. Mater.* **2014,** *13* (10), 961-969.

139. Zhao, C.-Z.; Cheng, X.-B.; Zhang, R.; Peng, H.-J.; Huang, J.-Q.; Ran, R.; Huang, Z.-H.; Wei, F.; Zhang, Q., Li2S5-based ternary-salt electrolyte for robust lithium metal anode. *Energy Storage Mater.* **2016,** *3*, 77-84.

140. Zhang, S. S., Role of LiNO3 in rechargeable lithium/sulfur battery. *Electrochim. Acta* **2012,** *70*, 344-348.

141. Li, W.; Yao, H.; Yan, K.; Zheng, G.; Liang, Z.; Chiang, Y.-M.; Cui, Y., The synergetic

170

effect of lithium polysulfide and lithium nitrate to prevent lithium dendrite growth. *Nature Communications* **2015,** *6* (1), 7436.

142. Li, S.;　Jiang, M.;　Xie, Y.;　Xu, H.;　Jia, J.; Li, J., Developing High-Performance Lithium Metal Anode in Liquid Electrolytes: Challenges and Progress. *Adv. Mater.* **2018,** *30* (17), 1706375.

143. Zhao, Y.;　Li, G.;　Gao, Y.;　Wang, D.;　Huang, Q.; Wang, D., Stable Li Metal Anode by a Hybrid Lithium Polysulfidophosphate/Polymer Cross-Linking Film. *ACS Energy Lett.* **2019,** *4* (6), 1271-1278.

144. Zhang, X.-Q.;　Cheng, X.-B.;　Chen, X.;　Yan, C.; Zhang, Q., Fluoroethylene Carbonate Additives to Render Uniform Li Deposits in Lithium Metal Batteries. *Advanced Functional Materials* **2017,** *27* (10), 1605989.

145. Zheng, J.;　Engelhard, M. H.;　Mei, D.;　Jiao, S.;　Polzin, B. J.;　Zhang, J.-G.; Xu, W., Electrolyte additive enabled fast charging and stable cycling lithium metal batteries. *Nat. Energy* **2017,** *2*, 17012.

146. Xu, Y.;　Wu, H.;　He, Y.;　Chen, Q.;　Zhang, J.-G.;　Xu, W.; Wang, C., Atomic to Nanoscale Origin of Vinylene Carbonate Enhanced Cycling Stability of Lithium Metal Anode Revealed by Cryo-Transmission Electron Microscopy. *Nano Lett.* **2020,** *20* (1), 418-425.

147. Xu, Y.;　Gao, L.;　Shen, L.;　Liu, Q.;　Zhu, Y.;　Liu, Q.;　Li, L.;　Kong, X.;　Lu, Y.; Wu, H. B., Ion-Transport-Rectifying Layer Enables Li-Metal Batteries with High Energy Density. *Matter* **2020**.

148. Li, N.-W.;　Yin, Y.-X.;　Yang, C.-P.; Guo, Y.-G., An Artificial Solid Electrolyte Interphase Layer for Stable Lithium Metal Anodes. *Adv. Mater.* **2016,** *28* (9), 1853-1858.

149. Yu, Z.;　Cui, Y.; Bao, Z., Design Principles of Artificial Solid Electrolyte Interphases for Lithium-Metal Anodes. *Cell Reports Physical Science* **2020,** *1* (7), 100119.

150. Liu, Y.; Lin, D.; Yuen, P. Y.; Liu, K.; Xie, J.; Dauskardt, R. H.; Cui, Y., An Artificial Solid Electrolyte Interphase with High Li-Ion Conductivity, Mechanical Strength, and Flexibility for Stable Lithium Metal Anodes. *Adv. Mater.* **2017,** *29* (10), 1605531.

151. Luo, L.; Manthiram, A., An Artificial Protective Coating toward Dendrite-Free Lithium-Metal Anodes for Lithium–Sulfur Batteries. *Energy Technology* **2020,** *8* (7), 2000348.

152. Liang, X.; Pang, Q.; Kochetkov, I. R.; Sempere, M. S.; Huang, H.; Sun, X.; Nazar, L. F., A facile surface chemistry route to a stabilized lithium metal anode. *Nat. Energy* **2017,** *2* (9), 17119.

153. Li, P.; Dong, X.; Li, C.; Liu, J.; Liu, Y.; Feng, W.; Wang, C.; Wang, Y.; Xia, Y., Anchoring an Artificial Solid–Electrolyte Interphase Layer on a 3D Current Collector for High-Performance Lithium Anodes. *Angew. Chem. Int. Ed.* **2019,** *58* (7), 2093-2097.

154. Xu, H.; Li, S.; Chen, X.; Zhang, C.; Tang, Z.; Fan, H.; Yu, Y.; Liu, W.; Liang, N.; Huang, Y.; Li, J., Surpassing lithium metal rechargeable batteries with self-supporting Li–Sn–Sb foil anode. *Nano Energy* **2020,** *74*, 104815.

155. Wang, H.; Liu, Y.; Li, Y.; Cui, Y., Lithium Metal Anode Materials Design: Interphase and Host. *Electrochem. Energy Rev.* **2019,** *2* (4), 509-517.

156. Lopez, J.; Mackanic, D. G.; Cui, Y.; Bao, Z., Designing polymers for advanced battery chemistries. *Nat. Rev. Mater.* **2019,** *4* (5), 312-330.

157. Li, N.-W.; Shi, Y.; Yin, Y.-X.; Zeng, X.-X.; Li, J.-Y.; Li, C.-J.; Wan, L.-J.; Wen, R.; Guo, Y.-G., A Flexible Solid Electrolyte Interphase Layer for Long-Life Lithium Metal Anodes. *Angew. Chem. Int. Ed.* **2018,** *57* (6), 1505-1509.

158. Zheng, G.; Wang, C.; Pei, A.; Lopez, J.; Shi, F.; Chen, Z.; Sendek, A. D.; Lee, H.-W.; Lu, Z.; Schneider, H.; Safont-Sempere, M. M.; Chu, S.; Bao, Z.; Cui, Y., High-Performance

Lithium Metal Negative Electrode with a Soft and Flowable Polymer Coating. *ACS Energy Lett.* **2016,** *1* (6), 1247-1255.

159. Luo, J.; Fang, C.-C.; Wu, N.-L., High Polarity Poly(vinylidene difluoride) Thin Coating for Dendrite-Free and High-Performance Lithium Metal Anodes. *Adv. Energy Mater.* **2018,** *8* (2), 1701482.

160. Aetukuri, N. B.; Kitajima, S.; Jung, E.; Thompson, L. E.; Virwani, K.; Reich, M.-L.; Kunze, M.; Schneider, M.; Schmidbauer, W.; Wilcke, W. W.; Bethune, D. S.; Scott, J. C.; Miller, R. D.; Kim, H.-C., Flexible Ion-Conducting Composite Membranes for Lithium Batteries. *Adv. Energy Mater.* **2015,** *5* (14), 1500265.

161. Shi, H.; Qin, J.; Huang, K.; Lu, P.; Zhang, C.; Dong, Y.; Ye, M.; Liu, Z.; Wu, Z.-S., A Two-Dimensional Mesoporous Polypyrrole–Graphene Oxide Heterostructure as a Dual-Functional Ion Redistributor for Dendrite-Free Lithium Metal Anodes. *Angew. Chem. Int. Ed.* **2020,** *59* (29), 12147-12153.

162. Wu, C.; Guo, F.; Zhuang, L.; Ai, X.; Zhong, F.; Yang, H.; Qian, J., Mesoporous Silica Reinforced Hybrid Polymer Artificial Layer for High-Energy and Long-Cycling Lithium Metal Batteries. *ACS Energy Lett.* **2020,** *5* (5), 1644-1652.

163. Gao, Y.; Zhao, Y.; Li, Y. C.; Huang, Q.; Mallouk, T. E.; Wang, D., Interfacial Chemistry Regulation via a Skin-Grafting Strategy Enables High-Performance Lithium-Metal Batteries. *J. Am. Chem. Soc.* **2017,** *139* (43), 15288-15291.

164. Gao, Y.; Yan, Z.; Gray, J. L.; He, X.; Wang, D.; Chen, T.; Huang, Q.; Li, Y. C.; Wang, H.; Kim, S. H.; Mallouk, T. E.; Wang, D., Polymer–inorganic solid–electrolyte interphase for stable lithium metal batteries under lean electrolyte conditions. *Nat. Mater.* **2019,** *18* (4), 384-389.

173

165. Wei, J.-Y.; Zhang, X.-Q.; Hou, L.-P.; Shi, P.; Li, B.-Q.; Xiao, Y.; Yan, C.; Yuan, H.; Huang, J.-Q., Shielding Polysulfide Intermediates by an Organosulfur-Containing Solid Electrolyte Interphase on the Lithium Anode in Lithium–Sulfur Batteries. *Adv. Mater.* **2020,** *n/a* (n/a), 2003012.

166. Frisch, M. J.; Trucks, G. W.; Schlegel, H. B.; Scuseria, G. E.; Robb, M. A.; Cheeseman, J. R.; Scalmani, G.; Barone, V.; Petersson, G. A.; Nakatsuji, H.; Li, X.; Caricato, M.; Marenich, A. V.; Bloino, J.; Janesko, B. G.; Gomperts, R.; Mennucci, B.; Hratchian, H. P.; Ortiz, J. V.; Izmaylov, A. F.; Sonnenberg, J. L.; Williams; Ding, F.; Lipparini, F.; Egidi, F.; Goings, J.; Peng, B.; Petrone, A.; Henderson, T.; Ranasinghe, D.; Zakrzewski, V. G.; Gao, J.; Rega, N.; Zheng, G.; Liang, W.; Hada, M.; Ehara, M.; Toyota, K.; Fukuda, R.; Hasegawa, J.; Ishida, M.; Nakajima, T.; Honda, Y.; Kitao, O.; Nakai, H.; Vreven, T.; Throssell, K.; Montgomery Jr., J. A.; Peralta, J. E.; Ogliaro, F.; Bearpark, M. J.; Heyd, J. J.; Brothers, E. N.; Kudin, K. N.; Staroverov, V. N.; Keith, T. A.; Kobayashi, R.; Normand, J.; Raghavachari, K.; Rendell, A. P.; Burant, J. C.; Iyengar, S. S.; Tomasi, J.; Cossi, M.; Millam, J. M.; Klene, M.; Adamo, C.; Cammi, R.; Ochterski, J. W.; Martin, R. L.; Morokuma, K.; Farkas, O.; Foresman, J. B.; Fox, D. J. *Gaussian 16 Rev. B.01*, Wallingford, CT, 2016.

167. Becke, A. D., Density-functional exchange-energy approximation with correct asymptotic behavior. *Phys. Rev. A* **1988,** *38* (6), 3098-3100.

168. Lee, C.; Yang, W.; Parr, R. G., *Phys. Rev. B* **1988,** *37*, 785.

169. Becke, A. D., A new mixing of Hartree–Fock and local density-functional theories. *J. Chem. Phys.* **1993,** *98* (2), 1372-1377.

170. Stephens, P. J.; Devlin, F. J.; Chabalowski, C. F.; Frisch, M. J., Ab Initio Calculation of Vibrational Absorption and Circular Dichroism Spectra Using Density Functional Force Fields. *J.*

Phys. Chem **1994,** *98* (45), 11623-11627.

171. Grimme, S.;   Antony, J.;   Ehrlich, S.; Krieg, H., A consistent and accurate ab initio parametrization of density functional dispersion correction (DFT-D) for the 94 elements H-Pu. *J. Chem. Phys.* **2010,** *132* (15), 154104.

172. Zhang, X.-P.;   Sun, Y.-Y.;   Sun, Z.;   Yang, C.-S.; Zhang, T., Anode interfacial layer formation via reductive ethyl detaching of organic iodide in lithium–oxygen batteries. *Nature Communications* **2019,** *10* (1), 3543.

173. Wang, Q.;   Yao, Z.;   Zhao, C.;   Verhallen, T.;   Tabor, D. P.;   Liu, M.;   Ooms, F.;   Kang, F.;   Aspuru-Guzik, A.;   Hu, Y.-S.;   Wagemaker, M.; Li, B., Interface chemistry of an amide electrolyte for highly reversible lithium metal batteries. *Nature Communications* **2020,** *11* (1), 4188.

174. Chen, H.;   Pei, A.;   Lin, D.;   Xie, J.;   Yang, A.;   Xu, J.;   Lin, K.;   Wang, J.;   Wang, H.;   Shi, F.;   Boyle, D.; Cui, Y., Uniform High Ionic Conducting Lithium Sulfide Protection Layer for Stable Lithium Metal Anode. *Adv. Energy Mater.* **2019,** *9* (22), 1900858.

175. Xu, H.;   Chien, P.-H.;   Shi, J.;   Li, Y.;   Wu, N.;   Liu, Y.;   Hu, Y.-Y.; Goodenough, J. B., High-performance all-solid-state batteries enabled by salt bonding to perovskite in poly(ethylene oxide). *Proc. Natl. Acad. Sci.* **2019,** *116* (38), 18815-18821.

176. Gao, L.;   Ge, X.;   Zuo, Z.;   Wang, F.;   Liu, X.;   Lv, M.;   Shi, S.;   Xu, L.;   Liu, T.;   Zhou, Q.;   Ye, X.; Xiao, S., High Quality Pyrazinoquinoxaline-Based Graphdiyne for Efficient Gradient Storage of Lithium Ions. *Nano Lett.* **2020,** *20* (10), 7333-7341.

177. Cano, Z. P.;   Banham, D.;   Ye, S.;   Hintennach, A.;   Lu, J.;   Fowler, M.; Chen, Z., Batteries and fuel cells for emerging electric vehicle markets. *Nature Energy* **2018,** *3* (4), 279-289.

178. Albertus, P.;   Babinec, S.;   Litzelman, S.; Newman, A., Status and challenges in enabling the

lithium metal electrode for high-energy and low-cost rechargeable batteries. *Nature Energy* **2018,** *3* (1), 16-21.

179. Lin, D.;　Liu, Y.; Cui, Y., Reviving the lithium metal anode for high-energy batteries. *Nature Nanotechnology* **2017,** *12* (3), 194-206.

180. Cheng, X.-B.;　Zhang, R.;　Zhao, C.-Z.;　Wei, F.;　Zhang, J.-G.; Zhang, Q., A Review of Solid Electrolyte Interphases on Lithium Metal Anode. *Advanced Science* **2016,** *3* (3), 1500213.

181. Xu, R.;　Cheng, X.-B.;　Yan, C.;　Zhang, X.-Q.;　Xiao, Y.;　Zhao, C.-Z.;　Huang, J.-Q.; Zhang, Q., Artificial Interphases for Highly Stable Lithium Metal Anode. *Matter* **2019,** *1* (2), 317-344.

182. Lin, D.;　Liu, Y.;　Chen, W.;　Zhou, G.;　Liu, K.;　Dunn, B.; Cui, Y., Conformal Lithium Fluoride Protection Layer on Three-Dimensional Lithium by Nonhazardous Gaseous Reagent Freon. *Nano Letters* **2017,** *17* (6), 3731-3737.

183. Qian, J.;　Henderson, W. A.;　Xu, W.;　Bhattacharya, P.;　Engelhard, M.;　Borodin, O.; Zhang, J.-G., High rate and stable cycling of lithium metal anode. *Nature Communications* **2015,** *6* (1), 6362.

184. Brissot, C.;　Rosso, M.;　Chazalviel, J. N.; Lascaud, S., Dendritic growth mechanisms in lithium/polymer cells. *Journal of Power Sources* **1999,** *81-82*, 925-929.

185. Sand, H. J. S., On the Concentration at the Electrodes in a Solution, with special reference to the Liberation of Hydrogen by Electrolysis of a Mixture of Copper Sulphate and Sulphuric Acid. *Proceedings of the Physical Society of London* **1899,** *17* (1), 496-534.

186. Tu, Z.;　Choudhury, S.;　Zachman, M. J.;　Wei, S.;　Zhang, K.;　Kourkoutis, L. F.; Archer, L. A., Designing Artificial Solid-Electrolyte Interphases for Single-Ion and High-Efficiency Transport

in Batteries. *Joule* **2017,** *1* (2), 394-406.

187. Li, Z.;   Liu, Z.-W.;   Mu, Z.-J.;   Cao, C.;   Li, Z.;   Wang, T.-X.;   Li, Y.;   Ding, X.;   Han, B.-H.; Feng, W. J. M. C. F., Cationic covalent organic framework based all-solid-state electrolytes. **2020,** *4* (4), 1164-1173.

188. Chen, H.;   Tu, H.;   Hu, C.;   Liu, Y.;   Dong, D.;   Sun, Y.;   Dai, Y.;   Wang, S.;   Qian, H.; Lin, Z. J. J. o. t. A. C. S., Cationic covalent organic framework nanosheets for fast Li-ion conduction. **2018,** *140* (3), 896-899.

189. Ashraf, S.;   Zuo, Y.;   Li, S.;   Liu, C.;   Wang, H.;   Feng, X.;   Li, P.; Wang, B. J. C. A. E. J., Crystalline anionic germanate covalent organic framework for high CO2 selectivity and fast Li ion conduction. **2019,** *25* (59), 13479-13483.

190. Guo, Z.;   Zhang, Y.;   Dong, Y.;   Li, J.;   Li, S.;   Shao, P.;   Feng, X.; Wang, B. J. J. o. t. A. C. S., Fast ion transport pathway provided by polyethylene glycol confined in covalent organic frameworks. **2019,** *141* (5), 1923-1927.

191. Du, Y.;   Yang, H.;   Whiteley, J. M.;   Wan, S.;   Jin, Y.;   Lee, S. H.; Zhang, W. J. A. C., Ionic covalent organic frameworks with spiroborate linkage. **2016,** *128* (5), 1769-1773.

192. Jeong, K.;   Park, S.;   Jung, G. Y.;   Kim, S. H.;   Lee, Y.-H.;   Kwak, S. K.; Lee, S.-Y. J. J. o. t. A. C. S., Solvent-free, single lithium-ion conducting covalent organic frameworks. **2019,** *141* (14), 5880-5885.

193. Zhang, Y.;   Duan, J.;   Ma, D.;   Li, P.;   Li, S.;   Li, H.;   Zhou, J.;   Ma, X.;   Feng, X.; Wang, B. J. A. C., Three-dimensional anionic cyclodextrin-based covalent organic frameworks. **2017,** *129* (51), 16531-16535.

194. Stewart, P.;   Renney, C. M.;   Mooibroek, T. J.;   Ferheen, S.; Davis, A. P., Maltodextrin

recognition by a macrocyclic synthetic lectin. *Chemical Communications* **2018,** *54* (62), 8649-8652.

195. Roeser, J.; Prill, D.; Bojdys, M. J.; Fayon, P.; Trewin, A.; Fitch, A. N.; Schmidt, M. U.; Thomas, A., Anionic silicate organic frameworks constructed from hexacoordinate silicon centres. *Nature Chemistry* **2017,** *9*, 977.

196. Delley, B. J. T. J. o. c. p., An all-electron numerical method for solving the local density functional for polyatomic molecules. **1990,** *92* (1), 508-517.

197. Delley, B. J. T. J. o. c. p., From molecules to solids with the DMol 3 approach. **2000,** *113* (18), 7756-7764.

198. Perdew, J. P.; Burke, K.; Ernzerhof, M. J. P. r. l., Generalized gradient approximation made simple. **1996,** *77* (18), 3865.

199. Tkatchenko, A.; Scheffler, M. J. P. r. l., Accurate molecular van der Waals interactions from ground-state electron density and free-atom reference data. **2009,** *102* (7), 073005.

200. Monkhorst, H. J.; Pack, J. D. J. P. r. B., Special points for Brillouin-zone integrations. **1976,** *13* (12), 5188.

201. Halgren, T. A.; Lipscomb, W. N. J. C. P. L., The synchronous-transit method for determining reaction pathways and locating molecular transition states. **1977,** *49* (2), 225-232.

202. Lu, T.; Chen, F. J. J. o. c. c., Multiwfn: a multifunctional wavefunction analyzer. **2012,** *33* (5), 580-592.

203. Zhao, Y.; Truhlar, D. G. J. T. C. A., The M06 suite of density functionals for main group thermochemistry, thermochemical kinetics, noncovalent interactions, excited states, and transition elements: two new functionals and systematic testing of four M06-class functionals and 12 other functionals. **2008,** *120* (1-3), 215-241.

204. Frisch, M.; Clemente, F. J. S., V. Barone, B. Mennucci, GA Petersson, H. Nakatsuji, M. Caricato, X. Li, HP Hratchian, AF Izmaylov, J. Bloino, G. Zhe, Gaussian 09, Revision A. 01, MJ Frisch, GW Trucks, HB Schlegel, GE Scuseria, MA Robb, JR Cheeseman, G.

205. Roeser, J.; Prill, D.; Bojdys, M. J.; Fayon, P.; Trewin, A.; Fitch, A. N.; Schmidt, M. U.; Thomas, A., Anionic silicate organic frameworks constructed from hexacoordinate silicon centres. *Nature Chemistry* **2017,** *9* (10), 977-982.

206. Hahn, F. E.; Keck, M.; Raymond, K. N., Catecholate Complexes of Silicon: Synthesis and Molecular and Crystal Structures of [Si(cat)2].cntdot.2THF and Li2[Si(cat)3].cntdot.3.5dme (cat = Catecholate Dianion). *Inorganic Chemistry* **1995,** *34* (6), 1402-1407.

207. Li, Z.; Liu, Z.-W.; Mu, Z.-J.; Cao, C.; Li, Z.; Wang, T.-X.; Li, Y.; Ding, X.; Han, B.-H.; Feng, W., Cationic covalent organic framework based all-solid-state electrolytes. *Materials Chemistry Frontiers* **2020,** *4* (4), 1164-1173.

208. Chen, H.; Tu, H.; Hu, C.; Liu, Y.; Dong, D.; Sun, Y.; Dai, Y.; Wang, S.; Qian, H.; Lin, Z.; Chen, L., Cationic Covalent Organic Framework Nanosheets for Fast Li-Ion Conduction. *Journal of the American Chemical Society* **2018,** *140* (3), 896-899.

209. Ashraf, S.; Zuo, Y.; Li, S.; Liu, C.; Wang, H.; Feng, X.; Li, P.; Wang, B., Crystalline Anionic Germanate Covalent Organic Framework for High CO2 Selectivity and Fast Li Ion Conduction. *Chemistry – A European Journal* **2019,** *25* (59), 13479-13483.

210. Guo, Z.; Zhang, Y.; Dong, Y.; Li, J.; Li, S.; Shao, P.; Feng, X.; Wang, B., Fast Ion Transport Pathway Provided by Polyethylene Glycol Confined in Covalent Organic Frameworks. *Journal of the American Chemical Society* **2019,** *141* (5), 1923-1927.

211. Du, Y.; Yang, H.; Whiteley, J. M.; Wan, S.; Jin, Y.; Lee, S.-H.; Zhang, W., Ionic Covalent

Organic Frameworks with Spiroborate Linkage. *Angewandte Chemie International Edition* **2016,** *55* (5), 1737-1741.

212. Jeong, K.; Park, S.; Jung, G. Y.; Kim, S. H.; Lee, Y.-H.; Kwak, S. K.; Lee, S.-Y., Solvent-Free, Single Lithium-Ion Conducting Covalent Organic Frameworks. *Journal of the American Chemical Society* **2019,** *141* (14), 5880-5885.

213. Zhang, Y.; Duan, J.; Ma, D.; Li, P.; Li, S.; Li, H.; Zhou, J.; Ma, X.; Feng, X.; Wang, B., Three-Dimensional Anionic Cyclodextrin-Based Covalent Organic Frameworks. *Angewandte Chemie International Edition* **2017,** *56* (51), 16313-16317.

214. Shi, W.; Shen, J.; Shen, L.; Hu, W.; Xu, P.; Baucom, J. A.; Ma, S.; Yang, S.; Chen, X.-M.; Lu, Y., Electrolyte Membranes with Biomimetic Lithium-Ion Channels. *Nano Letters* **2020,** *20* (7), 5435-5442.

215. Ma, S.; Shen, L.; Liu, Q.; Shi, W.; Zhang, C.; Liu, F.; Baucom, J. A.; Zhang, D.; Yue, H.; Wu, H. B.; Lu, Y., Class of Solid-like Electrolytes for Rechargeable Batteries Based on Metal–Organic Frameworks Infiltrated with Liquid Electrolytes. *ACS Applied Materials & Interfaces* **2020,** *12* (39), 43824-43832.

216. Lu, X.; Wu, H.; Kong, D.; Li, X.; Shen, L.; Lu, Y., Facilitating Lithium-Ion Conduction in Gel Polymer Electrolyte by Metal-Organic Frameworks. *ACS Materials Letters* **2020,** *2* (11), 1435-1441.

217. Qiao, B.; Leverick, G. M.; Zhao, W.; Flood, A. H.; Johnson, J. A.; Shao-Horn, Y., Supramolecular Regulation of Anions Enhances Conductivity and Transference Number of Lithium in Liquid Electrolytes. *Journal of the American Chemical Society* **2018,** *140* (35), 10932-10936.

218. Hayamizu, K.; Aihara, Y., Lithium ion diffusion in solid electrolyte (Li2S)7(P2S5)3 measured by

pulsed-gradient spin-echo 7Li NMR spectroscopy. *Solid State Ionics* **2013,** *238*, 7-14.

219. Chen, W.; Hu, Y.; Lv, W.; Lei, T.; Wang, X.; Li, Z.; Zhang, M.; Huang, J.; Du, X.; Yan, Y.; He, W.; Liu, C.; Liao, M.; Zhang, W.; Xiong, J.; Yan, C., Lithiophilic montmorillonite serves as lithium ion reservoir to facilitate uniform lithium deposition. *Nature Communications* **2019,** *10* (1), 4973.

220. Radvanyi, E.; De Vito, E.; Porcher, W.; Jouanneau Si Larbi, S., An XPS/AES comparative study of the surface behaviour of nano-silicon anodes for Li-ion batteries. *Journal of Analytical Atomic Spectrometry* **2014,** *29* (6), 1120-1131.

221. Seh, Z. W.; Wang, H.; Hsu, P.-C.; Zhang, Q.; Li, W.; Zheng, G.; Yao, H.; Cui, Y., Facile synthesis of Li2S–polypyrrole composite structures for high-performance Li2S cathodes. *Energy & Environmental Science* **2014,** *7* (2), 672-676.

222. Strauß, F.; Hüger, E.; Heitjans, P.; Trouillet, V.; Bruns, M.; Schmidt, H., Li–Si thin films for battery applications produced by ion-beam co-sputtering. *RSC Advances* **2015,** *5* (10), 7192-7195.

223. Liu, F.; Xiao, Q.; Wu, H. B.; Shen, L.; Xu, D.; Cai, M.; Lu, Y., Fabrication of Hybrid Silicate Coatings by a Simple Vapor Deposition Method for Lithium Metal Anodes. *Advanced Energy Materials* **2018,** *8* (6), 1701744.

224. Bruce, P. G.; Vincent, C. A., Steady state current flow in solid binary electrolyte cells. *Journal of Electroanalytical Chemistry and Interfacial Electrochemistry* **1987,** *225* (1), 1-17.

225. Hwang, J.-Y.; Park, S.-J.; Yoon, C. S.; Sun, Y.-K., Customizing a Li–metal battery that survives practical operating conditions for electric vehicle applications. *Energy & Environmental Science* **2019,** *12* (7), 2174-2184.

226. Philippe, B.; Dedryvère, R.; Allouche, J.; Lindgren, F.; Gorgoi, M.; Rensmo, H.;

Gonbeau, D.; Edström, K., Nanosilicon Electrodes for Lithium-Ion Batteries: Interfacial Mechanisms Studied by Hard and Soft X-ray Photoelectron Spectroscopy. *Chemistry of Materials* **2012,** *24* (6), 1107-1115.

227. Zhao, Z.; Chen, W.; Impeng, S.; Li, M.; Wang, R.; Liu, Y.; Zhang, L.; Dong, L.; Unruangsri, J.; Peng, C.; Wang, C.; Namuangruk, S.; Lee, S.-Y.; Wang, Y.; Lu, H.; Guo, J., Covalent organic framework-based ultrathin crystalline porous film: manipulating uniformity of fluoride distribution for stabilizing lithium metal anode. *Journal of Materials Chemistry A* **2020,** *8* (6), 3459-3467.